

Proceedings of the

3rd MSG RAO Workshop

5 June 2006
Helsinki, Finland



MSG13

Organising Committee

E. Oriol-Pibernat, ESA

Y. Govaerts, EUMETSAT

M. Pooley, EUMETSAT

Publication: Proceedings of the 3rd MSG RAO Workshop, 15 June 2006,
Helsinki, Finland (ESA SP-619, August 2006)

Editor: D. Danesy, ESA Publications Division

Published and distributed by: ESA Publications Division
ESTEC, Postbus 299
2200 AG Noordwijk
The Netherlands

Printed in: The Netherlands

Price: € 30

ISBN: 92-9092-930-8

ISSN: 0379-6566

Copyright: © 2006 European Space Agency

SP-619

August 2006

Proceedings of the
3rd MSG RAO Workshop

15 June 2006

Helsinki, Finland

European Space Agency
Agence spatiale européenne

FOREWORD

Evangelina Oriol-Pibernat

MSG & MetOp Mission Manager

ESA/ESRIN

Yves Govaerts

Remote Sensing Scientist

EUMETSAT

The Meteosat Second Generation (MSG) series ensures the continuity of the Meteosat data and services, but also provides improved observations in terms of spectral coverage, radiometric accuracy and data repeat rate. This represents an opportunity for research in many domains of Earth Sciences, not previously addressed by Meteosat.

The MSG Research Announcement of Opportunity (RAO) provided a structured framework for demonstrating the value of the MSG mission to innovative research in various Earth Sciences disciplines and for investigating the potential implications for the evolution of the operational services. The European Space Agency (ESA) and the European Organization for the Exploitation of Meteorological satellites (EUMETSAT) announced this opportunity to the worldwide scientific community in September 1998. Candidate Principal Investigators (PIs) were encouraged to submit research proposals using data from the MSG satellite series on:

- Innovative scientific investigations in areas such as
 - hydrology and land surface processes
 - atmospheric research
 - oceanography
 - climate research

- Calibration of MSG data and validation of geophysical products

- Investigation of new algorithms, including demonstration of new experimental products and of their value for research.

There were in total 43 projects jointly selected by ESA and EUMETSAT in November 1999, following a peer evaluation process initiated in February of the same year. Five of such projects were withdrawn, mainly for lack of resources.

The topics addressed in the investigations cover most of the foreseen RAO objectives, many going beyond, particularly for what refers to environmental issues.

Considering their leading role in MSG-relevant research, the selected PIs and their Co-Investigators (Co-Is) had access to required real-time and archived MSG data and products, even during the commissioning. Such data were provided by EUMETSAT, whilst ESA delivered necessary complementary data from ESA Earth Observation satellites, also free of charge.

The first MSG PI Workshop organised in Bologna, Italy, 17-19 May 2000, started this dialogue between the Investigators and the ESA and EUMETSAT relevant staff. A key objective was to deliver the latest information on the MSG mission objectives, capabilities and plans in order to enable all investigators to optimize their own investigation plans. A second objective was to have an overview and initial discussion of the planned investigations, including the associated needs for EUMETSAT (Meteosat, MSG) and ESA data (ERS & Envisat). A number of recommendations were formulated, as for instance to increase the delivery capabilities of the U-MARF, and were taken into account by ESA and EUMETSAT. The proceedings were published by ESA (SP-452).

The second MSG RAO Workshop (9-10 October 2004, Salzburg, Austria) was the first opportunity for ESA and EUMETSAT to present the status of the mission after its successful launch in 2002 and for the PIs to present the first results since the start of routine operations in early 2004. The proceedings were published by ESA (SP-582)

The third and final Workshop (15 June 2006, Helsinki, Finland) was the occasion for the scientists to provide tangible results about their investigations, after having had access to MSG-1 data for over two years. Being organised in parallel with the EUMETSAT Conference, it was also a good occasion for them to meet with the EUMETSAT user community at large.

Attendees to the Workshop were informed about the successful MSG-2 launch in December 2005 and about the final stages of its commissioning. Thus, it was assured the continuity of the MSG data stream, which was a key issue for keeping their interest in follow-on investigations with the MSG data. Also, those who had reached a mature stage of new applications, would be able to put them into operations.

ESA and EUMETSAT thanked those PIs and co-Is who managed to carry forward their investigations, in spite of the launch delay announced six years earlier, and encouraged them to keep using ESA and EUMETSAT data for their future research.

We hope these proceedings provide a comprehensive overview of the presentations and discussions held during the Workshop, and take this opportunity for thanking all participants for their active and stimulating contributions.

SP-619 Contents

A STATUS REPORT ON THE GERB PROGRAMME.....	1
<i>P. Allan, M. Bates, A. Smith & B. Stewart</i>	
GEOSTATIONARY EARTH RADIATION BUDGET (GERB): VALIDATION RESULTS	5
<i>J.E Russell, J.E. Harries & N. Clearbaux</i>	
CERES SCALES GROUND VALIDATION CAMPAIGNS FOR GERB. ASSESSMENT OF THE VALENCIA ANCHOR STATION CAPABILITIES.....	11
<i>E. Lopez-Baeza et al.</i>	
RADIOMETRIC CALIBRATION OF THE VISIBLE AND NEAR-INFRARED BANDS OF SEVIRI USING RAYLEIGH SCATTERING AND SUN-GLINT OVER OCEANS.....	19
<i>J.-M. Nicolas, P.-Y. Deschamps & O. Hagolle</i>	
MSG SEVIRI APPLICATIONS FOR WEATHER AND CLIMATE: CLOUD PROPERTIES AND CALIBRATIONS.....	25
<i>P. Minnis et al.</i>	
USE OF SEVIRI DATA FOR AN OPERATIONAL CMSAF SURFACE RADIATION BUDGET PROCESSING AND ITS VALIDATION	31
<i>R. Hollmann & R.W. Mueller</i>	
COMPARISON OF SEVIRI CLOUD PRODUCT WITH BOTH THE POLDER AND THE GLAS SPACE LIDAR ONE ...	37
<i>G. Sèze</i>	
REMOTE SENSING OF WATER AND ICE CLOUDS FROM MSG/SEVIRI.....	43
<i>B. Mayer, L. Bugliaro, H. Mannstein, T. Zinner, W. Krebs & P. Wendling</i>	
MSG FOG AND LOW STRATUS PRODUCTS AT LCRS (SOFOS).....	49
<i>J. Cermak, J. Bendix & T. Nauß</i>	
ENERGY-SPECIFIC SOLAR RADIATION DATA FROM MSG: THE HELIOSAT-3 PROJECT.....	52
<i>M. Schroedter-Homscheidt</i>	
IMPROVEMENT AND VALIDATION OF THE OZONE COLUMN PRODUCT DERIVED FROM THE SEVIRI 9.7 MICRON CHANNEL	59
<i>F. Karcher, A. Drouin, L. El Amraoui, V. Ferreira & A. Pacini</i>	
MODELING NATURAL SURFACE UV RADIATION WITH METEOSAT AND MSG.....	65
<i>J. Verdebout</i>	
NET AIR-SEA FLUX ESTIMATES FOR THE TROPICAL AND SUBTROPICAL ATLANTIC OCEAN BASED ON SATELLITE DATA.....	71
<i>K.B. Katsaros, R.T. Pinker, A. Bentamy, J.A. Carton, W.M. Drennan & A.M. Mestas-Nuñez</i>	
OPERATIONAL DERIVATION OF SURFACE ALBEDO AND DOWN-WELLING SHORT-WAVE RADIATION IN THE SATELLITE APPLICATION FACILITY FOR LAND SURFACE ANALYSIS.....	77
<i>B. Geiger, D. Carrer, C. Meurey & J.-L. Roujean</i>	
MSG SEVIRI DATA FOR VEGETATION MONITORING AND LAND SURFACE PROCESS MODELING IN AFRICA	83
<i>Sandholt</i>	
FIRE DETECTION AND PARAMETERIZATION WITH MSG-SEVIRI SENSOR.....	89
<i>A. Calle, J.L. Casanova, C. Moclán, A. Romo & S. Fraile</i>	
LIST OF PARTICIPANTS.....	99
ADDITIONAL MATERIAL – CONFERENCE PHOTOS (CD ONLY)	

A STATUS REPORT ON THE GERB PROGRAMME

Peter Allan, Martin Bates, Andy Smith, Brian Stewart

*Rutherford Appleton Laboratory, Chilton, Didcot, Oxon OX11 0QX, England
p.m.allan@rl.ac.uk, m.j.bates@rl.ac.uk, a.smith@rl.ac.uk*

ABSTRACT

The first of the Geostationary Earth Radiation Budget (GERB) instruments has been delivering data since 2003 and has been in regular operational service since February 2004. The validation of the data has proven challenging (see paper by Russell in these proceedings), but the first public release of the data took place in May 2006. Building on from the success of the first GERB instrument, three more have been built in order to provide a consistent climate dataset for well over a decade.

This paper is an update of the one presented at the second MSG RAO workshop (Allan [1]). Some of the basic information about the instruments is repeated here to avoid the need for cross reference.

1. THE GERB INSTRUMENTS

The purpose of the Geostationary Earth Radiation Budget (GERB) instrument is to determine the Earth's radiation budget to high accuracy. It is the first Earth radiation budget instrument to be in geostationary orbit and hence it provides unique temporal sampling of almost half of the Earth, giving images approximately every 15 minutes. GERB measures the radiance from the Earth in two broad bands which are essentially the reflected sunlight from the Earth's surface and atmosphere and the total emission, specifically including the thermal emission and reflection, from the Earth. The first of the GERB instruments to be flown is located on Meteosat-8, the first of the Meteosat Second Generation satellites. Three more GERB instruments have been built. The first of the GERB instruments was funded by the UK Natural Environment Research Council and the following three by EUMETSAT. We note in passing that the instrument actually flying on Meteosat-8 is the second GERB that was built. The first instrument built is actually on Meteosat-9.

For a full description of the GERB instrument, see Harries et al [2], which also describes the calibration of the instrument, the ground segment processing system and gives examples of science applications.

2. DESIGN GOALS AND PERFORMANCE

The GERB instrument has several basic design goals. The fundamental goal is to measure the total radiative energy output of the Earth to an accuracy of 1%. The short wave channel is defined by a filter that cuts out radiation with a wavelength longer than $4\mu\text{m}$, giving designed shortwave and longwave channels of $0.4\mu\text{m}$ to $4\mu\text{m}$ and $4\mu\text{m}$ to $40\mu\text{m}$. In practice the short wave response extends down to $0.3\mu\text{m}$ and the longwave response to beyond $100\mu\text{m}$, thereby exceeding the design specification.

The GERB detector is a 256 element array that views a North-South strip of the Earth with a pixel size at the sub-satellite point of 44km square. It builds up an image of the Earth by using a rotating de-spin mirror to effectively remove the rotation of the satellite and to step the image of the Earth across the detector. It does this every 282 rotations of the satellite, building up a single Earth view in slightly less than 17 minutes. The electronic control unit for the de-spin mirror is synchronized with the rotation rate of the satellite using the "start of line" (SOL) pulse that the satellite generates. In addition, the electronic control unit for the de-spin mirror introduces a phase difference on each rotation that gives the effect of stepping the detector across the image of the Earth.

In order to be able to compare the data from GERB and SEVIRI, the original design goal for the accuracy of geolocation of the GERB pixels was 0.1 pixels, or 4 km. To date, it has not proven possible to achieve this level of accuracy for two reasons. Firstly, the E-W position of the image of the GERB detector is governed by the Start-of-Line pulse from the satellite. This signal is noisier than expected resulting in a slight mis-positioning of the detector on each rotation of the satellite. Even though the detector may not be viewing the exact scene expected, it should still be possible to know exactly where it did look. However, due to a slight misalignment of the rotation axes of the satellite and the de-spin mirror, it is difficult to reconstruct the position exactly. The rotation axis of the spacecraft changes with respect to the body axis of the spacecraft as fuel is used and due to thermal effects, so the effect changes over time. The accuracy with which a GERB pixel can be geolocated by "dead reckoning" is

currently 0.5 pixels, although work is continuing on improving this. The addition of data from SEVIRI allows us to improve the accuracy to a quarter of a pixel, which is the accuracy of the data used in the angular dependency model used to calculate the fluxes.

3. GERB DATA PRODUCTS

The GERB data are processed to several levels of scientifically useful products.

The first level of processing is to generate fully calibrated pixel data. These products are called non-averaged, non-rectified, geolocated radiance data (NANRG), as they contain the spatial coordinates of the pixels, but these contain the measured data of the location actually viewed and are not on a regular grid. Strictly speaking, these pixel arrays are not images, due to the irregular spacing of the columns of data, although they do look like images at first sight.

These products are used to generate (time) averaged, rectified, geolocated radiance data (ARG), where three successive Earth scans with the filter in, then with the filter out, are averaged and put on a regular spatial grid (rectified). These are true images.

The NANRG products are also used as input for calculating fluxes, which is done at the Royal Belgian Meteorological Institute (RMIB).

Real-time flux products are available from RMIB [3] and the NANRG, ARG and flux products are available from the project archive at the Rutherford Appleton Laboratory [4].

Table 1 – Types of GERB data products

Product name	Type	Temporal accuracy
NANRG	Pixel radiances	2.8 min
ARG	Gridded radiances	~ 17 min
Fluxes	Gridded fluxes and unfiltered radiances	15 min
Monthly means	Gridded fluxes	1 month

The validation of the GERB data was a challenging task due to the high accuracy required. The first public release of the data products took place in May 2006. The initial release consists of data gathered from 25 March 2006 onwards, with earlier data being added as they are reprocessed.

Anyone wishing to use the GERB data should look at the web site [4] which describes how to get access to the data. This also indicates periods when data are

unavailable due to the instrument not being in the normal operating mode.

4. GERB ON MSG-2

The second MSG satellite was launched on 21 December 2005 with a GERB instrument on board. While there is a concern about the water vapour channel on SEVIRI, both it and GERB are performing well and it is expected that MSG-2 will become the operational satellite sometime in the second half of 2006.

5. THE LONG-TERM CLIMATE RECORD

While section 2 noted some shortfalls in the ultimate performance of the GERB instrument on Meteosat-8, the data are generally of very high accuracy and will form a valuable set of climate data covering the period of operation of the Meteosat Second Generation satellites. This started in 2004 and is likely to extend up to approximately 2018.

As well as providing an accurate long term climate dataset, GERB provides a unique source of data on the Earth's radiation budget with rapid sampling (every 15 minutes), thereby enabling studies of the diurnal cycle that were previously not possible with sparsely sampled data (typically once every three days).

6. SUMMARY

Despite the problems noted above, GERB is proving to be a very successful instrument. GERB is the first Earth radiation budget to be on a geostationary satellite, and hence it will provide data that are uniquely suitable for studying diurnal changes, something that is not possible with instruments in low Earth orbit. The series of instruments will provide an accurate measurement of the Earth's radiation budget over the lifetime of the Meteosat Second Generation satellites. This will be of crucial importance for understanding the Earth's climate and in predicting future climate change.

7. ACKNOWLEDGMENTS

The design, building, calibration and validation of the GERB instrument and the ground segment have been done by a large team. These are the authors of reference [2].

The inter-comparison of GERB and CERES data has been particularly valuable in validating GERB data and the GERB team wishes to acknowledge the help that we have received from the CERES team.

The funding for the development of GERB-1 was provided by the UK Natural Environment Research Council, OSTC in Belgium and the Italian space agency ASI.

The project has received tremendous support from both EUMETSAT and ESA, and EUMETSAT have funded the three GERB instruments that will follow on from GERB-1.

8. REFERENCES

1. Allan, P.M, *The GERB Instrument – 2 years in orbit*, in proceedings of the 2nd MSG RAO workshop.
2. Harries J. E., Russell J. E., Kellock S., Hanafin J. A., Matthews G., Wrigley R., Last A., Mueller J., Rufus J., Brindley H., Futyran J., Mossavati R., Ashmall J., Sawyer E., Parker D., Caldwell M., Allan P. M., Smith A., Bates M. J., Coan B., Stewart B. C., Lepine D. R., Cornwall L. A., Corney D. R., Ricketts M. J., Drummond D., Smart D., Cutler R., Dewitte S., Clerbaux N., Gonzalez L., Ipe A., Bertrand C., Joukoff A., Crommelynck D., Nelms N., Llewellyn-Jones D. T., Butcher G., Smith G. L., Szewczyk Z. P., Mlynczak, P. E., Slingo A., Allan R. P. and Ringer M. A., 2005: *The Geostationary Earth Radiation Budget (GERB) Project*, Bulletin of the American Meteorological Society, **86**, 945-960.
3. The web site for the RMIB near real-time data service is gerb.oma.be
4. The web site for the GERB data processing and archiving system is ggsp.rl.ac.uk

GEOSTATIONARY EARTH RADIATION BUDGET (GERB): VALIDATION RESULTS

J E Russell⁽¹⁾, J E Harries⁽²⁾, N Clearbaux⁽³⁾

⁽¹⁾*Space and Atmospheric Physics, Imperial College, London SW7 2BZ, UK. Email: j.e.russell@imperial.ac.uk*

⁽²⁾*Space and Atmospheric Physics, Imperial College, London SW7 2BZ, UK. Email: j.harries@imperial.ac.uk*

⁽³⁾*Royal Meteorological Institute Belgium, Brussels, Belgium. Email: nic@oma.be*

ABSTRACT

The Geostationary Earth Radiation Budget (GERB) instrument on METEOSAT-8 is making the first measurements of the Earth's radiation budget from geostationary orbit. The first validated GERB Edition 1 products were released to the scientific community via the ggsp archive (<http://ggsp.rl.ac.uk>) earlier this year. This paper summaries the calibration accuracy and validation results for these Edition 1 products.

1 INTRODUCTION

The first Geostationary Earth Radiation Budget (GERB) [1] was launched as an instrument of opportunity onboard Meteosat-8 in August 2002 and made the first ever observations of the broadband reflected solar and emitted thermal energy from geostationary orbit in December 2002. Since this time it has been operating almost continuously, providing near-real time (NRT) shortwave and longwave top of the atmosphere radiances and fluxes every 15 minutes for the region 60W to 60E, 60N to 60S, with a spatial resolution at the sub-satellite point of 44.6 km (N-S) by 39.3 km (E-W).

A series of 4 GERB instruments will be flown sequentially on each of the Meteosat Second Generation (MSG) satellites along with the prime meteorological instrument the Scanning Enhanced Visible and Infrared (SEVIRI) ([2] and [3]). These should provide a continuous GERB data record spanning at least a decade.

GERB measurements provide a unique opportunity to study rapidly varying climate processes, and in turn provide improved understanding of these mechanisms to determine inter-annual and longer term climate variability. A thorough understanding of the accuracy of the measurements, supported by extensive validation is necessary to allow the data to be appropriately used. The first validated Edition 1 GERB data products were released to the scientific community earlier this year. This paper summaries the calibration accuracy for this first edition and reports on the validation results.

2 PROCESSING AND CALIBRATION ACCURACY

The absolute accuracy aims for the GERB products are 1% (of the typical full scale radiance) for the emitted thermal (hereafter referred to as LW) and the reflected

solar (hereafter referred to as SW) radiances, and 0.1 of a GERB pixel for the geolocation. The theoretical accuracy of the edition 1 GERB products does not meet all of these targets due to known issues which we plan to resolve in future releases. Below is a summary of the determined accuracy of the GERB radiances and geolocation.

2.1 Unfiltered radiances

Table 1 summarises the approximate magnitudes of each of the error contributions affecting the absolute accuracy of the GERB unfiltered radiances, and determines an RMS combination of the contributions. Errors are quoted as a percentage where a fixed error in the quantities corresponds to a fixed fractional error in the unfiltered radiances, independent of the magnitude of the unfiltered radiances. Where a fixed error causes a fixed radiance error on the unfiltered radiances, errors are quoted as a percentage of the typical full scale radiances which are taken to be $240 \text{ Wm}^{-2}\text{sr}^{-1}$ for the SW and $77 \text{ Wm}^{-2}\text{sr}^{-1}$ for consistency with the accuracy requirements. No random errors, including those that may be systematic for a particular scene type, are considered in table 1.

Errors due to the accuracy of the calibration sources and spectral response are determined as the combined effect of 1SD level spectrally random and spectrally systematic uncertainties on the sources and response measurements. For the spectral response the errors quoted are the worst case error in $\text{Wm}^{-2}\text{sr}^{-1}$ over a wide variety of simulated Earth scenes, expressed as a percentage of the full scale. As SEVIRI is used to unfilter the GERB radiances, the effect of the quoted SEVIRI calibration uncertainty is also determined. The simulated worst case effect of a SEVIRI inter-channel calibration error at a $\pm 5\%$ level is quoted for the LW and SW radiances. For the SW a worst case effect is an overestimation of the unfiltering factor by 0.8% if the errors on SEVIRI 0.6 μm is +5% and on 0.8 μm and 1.6 μm is -5%. For the longwave the worst case is found to be an overestimation of the unfiltering factor by 0.09% for -5% on 6.2 μm , 7.3 μm , 12 μm and 13.4 μm SEVIRI channels and +5% on 8.7 μm and 10.8 μm .

Table 1. Estimates of the ground determined unfiltered radiance bias error sources and magnitudes.

Error source	Reflected solar	Emitted thermal (night)	Emitted thermal (day)
Calibration sources absolute accuracy (1 SD uncertainty values)	~0.22%	<0.05%	
Calibration sources uniformity (full range over region used)	< 0.5%	Small	
Spectral response	1.9% of typical full scale	<0.9% of typical full scale	<0.9% of typical full scale
Stray light (maximum effect in un-flagged data)	<0.25 Wm ⁻² sr ⁻¹		
	<0.1% of typical full scale	<0.3% of typical full scale	
Polarisation (Worst case error for a completely linearly polarised source.)	<0.4%	Small	
SEVIRI inter-channel calibration	<1%	<0.1%	<0.1%
RMS combination of above errors	2.25%	0.96%	0.96%

Table 2. Estimates of the random errors on the unfiltered radiance.

Error source	Reflected solar	Emitted thermal (night)	Emitted thermal (day)
Instrument noise	0.13% of typical full scale	0.4% of typical full scale	0.6% of typical full scale
Geolocation	0.25 pixel		
Interpolation	0.63% of typical full scale	1% of typical full scale	1% of typical full scale
Spectral overlap correction	0.02% of typical full scale	None	0.08%
Unfiltering	0.3% of typical full scale	0.05% of typical full scale	0.05% of typical full scale

Random errors are considered in table 2. This table includes contributions from detector noise, interpolation and unfiltering. Uncertainties due to these sources are stated as percentages of the typical full scale radiances are before.

The estimated 1 standard deviation (1 SD) random error in geolocation accuracy is stated in terms of GERB pixels. It should be noted that geolocation errors will lead to errors in the assigned filtered radiances for a given location, and additional errors due to a mismatch with SEVIRI in the unfiltering factor and the radiance to flux conversion factors. Whilst random in origin, unfiltering and geolocation errors can lead to systematic errors in radiances and fluxes ascribed to a particular scene type.

2.2 Fluxes

GERB SW fluxes are derived from the GERB SW radiances using the CERES TRMM ADMs as the basis of the radiance to flux conversion [4].

The ADMs which are the basis of the radiance to flux conversions are statistical in nature and thus a random error will be associated with the instantaneous flux

estimates, the 1SD values of these errors are shown in table 3. In addition SEVIRI measurements are employed both for the scene identification required to choose the appropriate SW radiance to flux conversion factor, and in determining the longwave radiance to flux conversion. Thus, the effect of 5% calibration errors on the SEVIRI radiances and inter-channel calibration is also considered. These flux errors are additional to the radiance errors already discussed.

Effect of SEVIRI channel calibration is determined from simulations of the effect on the derived fluxes of a 5% calibration error in the SEVIRI radiances. In the SW such an error, if present in the 0.6µm radiances affects the cloudy scene identification used to choose the appropriate CERES ADM. In the LW radiance to flux conversion factors are chosen based on SEVIRI channel radiances and the error shown is the worst case effect of 5% inter-channel calibration errors in the LW on the determination of LW anisotropy factor.

Table 3. Addition error sources and approximate magnitudes to which the SW and LW fluxes are subject (see [4] for validation results on the CERES TRMM ADMs).

Error source	Reflected solar	Emitted thermal
SW ADM	$\sim 10 \text{ Wm}^{-2}$ random error	
LW anisotropy		$\sim 5.5 \text{ Wm}^{-2}$ random error
SEVIRI channel calibration and inter-channel calibration	$< 1.2 \text{ Wm}^{-2}$ bias $< 5.6 \text{ Wm}^{-2}$ random error	$< 1 \text{ Wm}^{-2}$ bias

3 VALIDATION RESULT SUMMARY:

The CERES instruments [5] flying on the low Earth orbit AQUA and TERRA satellites measure the outgoing longwave and reflected shortwave broad band radiances and fluxes in a similar manner to GERB. Their products have been extensively validated and have stated absolute accuracy of 1.0% for the shortwave 0.5% for the longwave radiances. The GERB ARG unfiltered radiances and fluxes have been compared to the CERES FM2 SSF rev 1 unfiltered radiances and fluxes. Results shown here are for the GERB V998 validation reprocessing data set, consisting of 21-27th June and 11th-17th December 2004. This processing version has the same science processing as the Edition 1 release GERB data.

3.1 Radiances

GERB and CERES FM2 SSF rev 1 radiances are matched for time, location and viewing. Matched data

have viewing angles within 5° of each other and the CERES acquisition time must be no more 170 seconds from the acquisition time for the relevant GERB ARG column. Only data with GERB viewing zenith angles $< 65^\circ$ for the SW and $< 80^\circ$ for the longwave are retained and solar zenith angles are also required to be $< 80^\circ$ for the SW comparison. The mean radiance for each day of GERB and CERES points is derived and the ratio of these two mean values determined. The mean and standard deviation of the ratio is then calculated from the daily ratios. Table 4 shows the mean ratio and an associated 99% confidence uncertainty determined as 3 times the standard deviation divided by the square root of the number of days.

Some scene dependence is seen in the SW radiance comparisons, with agreement between GERB and CERES (in percentage terms) being better for bright scenes than for dark scenes. This is exhibited by a higher SW ratio for ocean than for cloud or bright desert, for example.

Table 4. Results of radiance comparison for angularly matched and co-located GERB CERES radiances. SSF rev1 radiance data from FM2 (Edition 2) and GERB V998 data are compared. Rev1 all sky correction factor is applied to the CERES SW data. Overcast conditions for the SW are defined as a GERB cloud cover of 100% and optical depth of 7.4 or more.

FM2 (Edition 2) GERB/CERES	SW radiance data	LW radiance data
June	1.058 ± 0.005 (all sky) 1.041 ± 0.013 (overcast)	0.993 ± 0.001 (day) 0.990 ± 0.003 (night)
Dec	1.048 ± 0.005 (all sky) 1.032 ± 0.005 (overcast)	0.993 ± 0.001 (day) 0.988 ± 0.005 (night)

SW GERB/CERES (FM2) radiance ratios for Clear GERB pixels (GERB cloud cover 0%)	
Ocean	1.144 ± 0.043
Dark Vegetation	1.070 ± 0.017
Bright Vegetation	1.062 ± 0.010
Dark Desert	1.073 ± 0.019
Bright Desert	1.059 ± 0.006

It should be noted that the scene dependent differences may be affected by the comparison methodology and geolocation errors. For the extreme scenes geolocation errors can lead to systematic effects on the inferred average radiance. For example geolocation errors can lead scenes identified as ocean to occasionally contain some cloud; in the SW these cloud points will always be brighter than the dark ocean and therefore act to elevate the average SW radiance inferred. However, the scene dependent differences can also be due to systematic uncertainties in the spectral response of the instrument, as bluer scenes tend to darker scenes.

3.2 Fluxes

The GERB V998 level 2 ARG fluxes have also been compared to the CERES FM2 SSF rev 1 fluxes for the periods 21-27th June and 11th-17th December 2004. All CERES flux measurements, within 170 seconds of acquisition time of the relevant ARG column, falling within the GERB footprint are used (note: as fluxes are now compared there is no need to match viewing geometry). Prior to comparison the CERES SSF fluxes are adjusted from a 20km reference level to a surface reference level.

Each day the mean of GERB and CERES fluxes are determined and the ratio of these means derived. The mean and standard deviation of the ratio is then calculated from the daily ratios. The mean ratio and an associated 99% confidence uncertainty determined as 3 times the standard deviation divided by the square root of the number of days is displayed in table 5.

In addition in order to analyse viewing angle dependent and scene dependent differences an average of the matched points is constructed for each location and smoothed using a 5x5 ARG pixel moving average before being compared to construct a map of the GERB/CERES ratio over the GERB viewing region. The results of these comparisons are shown in figure 1 for the SW all sky and clear sky fluxes and figures 2 for the LW day-time and night-time fluxes.

Over the several days used to accumulate the averages, the CERES data contributing to the average at a given location will have been acquired from a range of viewing angles, whereas due to its geostationary orbit, the GERB viewing geometry remains relatively invariant for each point on the Earth. Thus whilst view angle dependent errors in the radiance to flux conversion will be much reduced in the CERES average, they are expected to remain in the GERB data at a level comparable to that present in the instantaneous measurements. The results thus highlight the view angle dependent errors in the radiance to flux conversion.

Overall the SW flux comparison shows a 1-2% increase in the GERB/CERES ratio compared to the radiance results, although there is reduced scene dependency seen. The discrepancy between the SW radiance comparison and SW flux comparison results can be attributed to a combination of differences in the ADMs (GERB uses the TRMM ADMs and the CERES fluxes used here are derived using the TERRA ADMs) and

Table 5. SW and LW flux comparison for co-located GERB CERES fluxes. Rev1 all sky correction factor is applied to the CERES SW data except for clear ocean where rev1 clear ocean factor is employed. Overcast conditions are defined from the GERB scene identification as 100% cloud cover with an optical depth above 7.4.

GERB/CERES FM2 (Edition 2) flux ratios	SW flux data	LW flux data
June	1.073 ± 0.004 (all sky) 1.054 ± 0.007 (overcast)	0.991 ± 0.001 (day time) 0.987 ± 0.001 (night time)
Dec	1.059 ± 0.004 (all sky) 1.044 ± 0.004 (overcast)	0.992 ± 0.001 (day time) 0.987 ± 0.001 (night time)

SW GERB/CERES (FM2) flux ratios for Clear GERB pixels (GERB cloud cover 0%)	
Ocean	1.085 ± 0.018
Dark Vegetation	1.072 ± 0.007
Bright Vegetation	1.082 ± 0.005
Dark Desert	1.081 ± 0.009
Bright Desert	1.068 ± 0.007

possible discrepancies in the scene identification. This is evidenced by the fact that comparison of the co-angular GERB CERES flux measurements results in, on average, a 1% difference between the two instruments in the SW anisotropy factors assigned to the SW radiances, which alone would result in an elevation of the GERB/CERES flux ratio by 1% compared to the radiances.

The geographical distribution of the GERB/CERES average flux ratio is shown in figure 1 for the SW. For the all-sky plots, the GERB/CERES SW flux ratio over much of the disk is relatively uniform. Exceptions are seen towards the edge of the disk, particularly for fluxes derived from observations with viewing zenith angles greater than 70°. Enhanced ratios are seen at the edges of the sunglint region (indicated by a roughly circular black region of missing data). Depressed ratios are seen off the West coast of Africa. As no specific aerosol treatment or radiance to flux conversion is employed, fluxes in the presence of aerosol are expected to be of reduced accuracy, and as this region of depressed flux is an area where significant aerosol effects are likely, aerosol contamination is a possible cause of the observed signature. In the clear sky the region of

depressed ratios is also clearly visible. In addition, enhanced ratios are seen for ocean points close to coastlines. These enhanced ratios are likely the result of geolocation errors causing land observations to be occasionally included in the average determined for the GERB ocean locations.

The GERB/CERES longwave flux ratios, shown in table 5, are similar to the radiance ratios. The geographical distribution of the GERB/CERES average LW flux ratio is shown in figure 2. A limb darkening effect is apparent in the LW flux comparisons, with GERB fluxes derived from observations at higher viewing angles producing lower ratios than those derived from low view angles. Enhanced ratios are also seen in regions associated with cloud particularly the ITCZ; this is believed to be related to a known problem in the GERB LW radiance to flux conversion of correctly modelling the anisotropy of semi-transparent cloud.

4 SUMMARY

The first validated GERB products were released to the scientific community earlier this year. The absolute accuracy of the GERB SW and LW unfiltered radiances



Figure 1 SW flux comparison for June (left) and December (right). GERB/FM2 ratio shown for all-sky conditions in upper panels and clear sky (identified by GERB scene ID) in lower panels. Ring in red shows limit of VZA = 70°.



Figure 2. LW flux comparison for June (left) and December (right). GERB/FM2 ratio shown for day-time matches in upper panels and night-time matches in lower panels. Ring in red shows limit of VZA = 70°

is determined to be 2.25% and 0.96% respectively. Angularly matched radiance intercomparisons with the CERES FM2 instrument show GERB SW radiances to be on average 5% higher and LW radiances to be 1% lower than the corresponding CERES quantities. GERB SW fluxes are seen to be on average 7% higher than CERES and LW fluxes 1% lower. Some angular dependency in the LW error is seen and problems with the radiance to flux conversion in the LW over high semitransparent cloud and the SW over aerosol are known to result in larger errors in the products.

5 REFERENCES

1. J E Harries, J E Russell, J A Hanafin, H Brindley, J Futyan, J Rufus, S Kellock, G Matthews, R Wrigley, A Last, J Mueller, R Mossavati, J Ashmall, E Sawyer, D Parker, M Caldwell, P M Allan, A Smith, M J Bates, B Coan, B C Stewart, D R Lepine, L A Cornwall, D R Corney, M J Ricketts, D Drummond, D Smart, R Cutler, S Dewitte, N Clerbaux, L Gonzalez, A Ipe, C Bertrand, A Joukoff, D Crommelynck, N Nelms, D T Llewellyn-Jones, G Butcher, G L Smith, Z P Szewczyk, P E Mlynczak, A Slingo, R P Allan and M A Ringer. The

Geostationary Earth Radiation Budget Project. *Bull Am Met Soc*, 2005, Volume 86, No. 7, pp 945-960.

2. Schmetz, J. P. Pili, S. Tjemkes, D. Just, J. Kerkmann, S. Rota, A. Ratier, 2002: An introduction to Meteosat Second Generation (MSG). *Bull. Amer. Meteor. Soc.*, 83, 977-994

3. Munro R., A. Ratier, J. Schmetz, D. Klaes, 2002: Atmospheric measurements from the MSG and EPS systems. *Adv. in Space Res.*, 29, 1609-1618.

4. Loeb N. G., K. Loukachine K, N. Manalo-Smith, B. A. Wielicki, D. F. Young, 2003. Angular distribution models for top-of-atmosphere radiative flux estimation from the Clouds and the Earth's Radiant Energy System instrument on the Tropical Rainfall Measuring Mission satellite. Part II: Validation. *J Applied Meteorology* 42 (12): December 1748-176

5. Wielicki, B. A., B. R. Barkstrom, E. F. Harrison, R. B. Lee III, G. L. Smith, and J. E. Cooper, 1996: Clouds and the Earth's Radiant Energy System (CERES): An Earth Observing System Experiment, *Bul Am Met Soc*, 77, 853-868.

**CERES SCALES GROUND VALIDATION CAMPAIGNS FOR GERB. ASSESSMENT OF
THE VALENCIA ANCHOR STATION CAPABILITIES**
**(In the framework of EUMETSAT/ESA MSG-RAO Project no. 138 GIST Proposal for
Calibration/Validation of SEVIRI and GERB (PI: J.E. Harries))**

E. Lopez-Baeza¹, A. Velázquez Blázquez¹, S. Alonso², S. Dewitte³, C. Diaz-Pabon², C. Domenech García¹, J.E. Harries⁴, J. Jorge⁵, A. Labajo², N. Pineda⁵, D. Pino^{6,8}, A. Rius⁶, J.E. Russell⁴, G.L. Smith^{7,9}, Z. P. Szewczyk^{7,10}, R. Tarruella⁵, and J. Torrobella⁶

⁽¹⁾University of Valencia. Dept. of Physics of the Earth and Thermodynamics. Climatology from Satellites Group. Calle Dr Moliner, 50. Burjassot. 46100 Valencia (Spain), Ernesto.Lopez@uv.es, Carlos.Domenech@uv.es, Almudena.Velazquez@uv.es

⁽²⁾Spanish Institute for Meteorology (INM). C/ Leonardo Prieto Castro, 8 (Ciudad Universitaria). 28071 Madrid (Spain), susana@inm.es, pabon@inm.es, alabajo@inm.es

⁽³⁾Royal Meteorological Institute of Belgium, Section Remote Sensing from Space, Ringlaan, 3, B-1180 Brussels (Belgium), Steven.Dewitte@oma.be

⁽⁴⁾Imperial College of Science, Technology and Medicine, Space and Atmospheric Physics Group, The Blackett Laboratory, London SW7 2BW (United Kingdom), j.harries@imperial.ac.uk, j.e.russell@imperial.ac.uk

⁽⁵⁾Polytechnic University of Catalonia, Applied Physics Department, Advanced Polytechnic School of Manresa, Av. Bases de Manresa, 61-73. 08240 Manresa. (Spain), joan.jorge@upc.es, npineda@fa.upc.es, Tarruella@eupm.upc.es

⁽⁶⁾Institute for Space Studies of Catalonia (IEEC). Campus UAB/Facultad de Ciencias, Torre C-5-parell-2^a planta, 08193 Bellaterra, Barcelona (Spain), rius@ieec.uab.es, badia@ieec.fcr.es

⁽⁷⁾NASA Langley Research Center, Hampton, VA 23681-2199, (USA)

⁽⁸⁾Polytechnic University of Catalonia, Applied Physics Department, Campus Castelldefels - Edif. C, Avda. del Canal Olímpic, s/n, 08860 Castelldefels, (Spain), david@fa.upc.es

⁽⁹⁾National Institute for Aerospace, Hampton, (USA), g.l.smith@larc.nasa.gov

⁽¹⁰⁾Science Applications International Corporation (SAIC), Hampton, (USA), z.p.szewczyk@larc.nasa.gov

ABSTRACT/RESUME

The Valencia Anchor Station (VAS) was set up by the University of Valencia at the natural region of Utiel-Requena Plateau in 2001. The plateau is a large and reasonably homogeneous area suitable for validation of low spatial resolution satellite data and products such as GERB's. In the framework of the EUMETSAT/ESA MSG-RAO Project no. 138 GIST Proposal for Calibration/Validation of SEVIRI and GERB, and of the Spanish Research Programme on Space Project SCALES (SEVIRI & GERB Cal/Val Area for Large-scale Field ExperimentS), three GERB ground validation campaigns have so far been carried out at the VAS under different land surface conditions. CERES instruments onboard NASA EOS Aqua and Terra satellites, operating in PAPS (Programmable Azimuth Plane Scanning) mode, have generously provided additional SW and LW radiance measurements to support validation efforts. These have shown to be most valuable as intermediate validation step between ground measurements and the large GERB pixel size.

1. INTRODUCTION

Calibration/Validation, or simply "Cal/Val", is the activity that endeavours to ensure that remote sensing products are highly consistent and reproducible. This is

an evolving discipline that is becoming increasingly important as more long-term studies on global change are undertaken, and new satellite missions are launched. Calibration is the process of quantitatively defining the system responses to known, controlled signal inputs. Validation is the process of assessing, by independent means, the quality of the data products derived from the system outputs [1]. Agencies usually undertake the calibration of their respective mission satellite systems, however to extend this beyond the commissioning phase is potentially very difficult. Thus, well-instrumented benchmark test sites and data sets for calibration should be supported, particularly for land applications, to provide calibration information to supplement or substitute for on-board calibration, in a coordinated way, and ensuring continuity, and reliability to access to their data with minimal delay.

The primary objective of validation is to assess the quality, and as far as possible quantify the accuracy of remote sensing products. Ideally, validation activities seek to compare data products to more accurate independent measurements of the same quantity over a statistically significant number of samples and wide variety of situations. The problem is that the space and time scales of *in-situ* and satellite data are rarely directly comparable. Typically, there are insufficient *in-situ* measurements to cover a satellite field of view,

whether the field of view is some meters (high resolution imagers) or several km (broadband radiometers). Even a perfect remote sensing measurement will differ from *in-situ* verification measurements due to the inability to match the observations in time or space. *In-situ* measurements are invariably taken at small space and time scales, while a satellite overpass is a few second snapshot of a large area. The matching error can be reduced (but not eliminated) by increasing the number of surface observations within the field of view (level 2 data) or grid box (level 3 data). It can also be minimized by using very large ensembles of matched data.

The *Valencia Anchor Station* (VAS) was set up by the *University of Valencia* at the Spanish natural region *Utiel-Requena Plateau* (Valencia, Spain) in 2001. The *plateau* is a large and reasonably homogeneous area suitable for validation of low spatial resolution satellite data and products such as GERB's.

In the framework of the EUMETSAT/ESA MSG-RAO Project no.138 *GIST Proposal for Calibration/Validation of SEVIRI and GERB*, and of the Spanish Research Programme on Space Project SCALES (*SEVIRI & GERB Cal/Val Area for Large-scale field ExperimentS*), three GERB ground validation campaigns have so far been carried out at the VAS under different land and atmosphere surface conditions. During these campaigns, CERES instruments onboard the NASA EOS *Aqua* and *Terra* satellites have generously provided additional radiance measurements to support validation efforts, which have shown to be most valuable as an intermediate validation step between ground measurements and the large GERB pixel size.

2. THE VALENCIA ANCHOR STATION

The main objective of the SCALES Project has been to develop an adequate methodology to validate large scale remote sensing products, specifically addressed to the GERB instrument [2], and for that we counted on a suitable reasonable homogeneous site at GERB's scale, the *Valencia Anchor Station*, robustly equipped with standard meteorological instruments and with a large suite of mobile instruments to account for the site non-homogeneities. It is placed in a reasonably homogeneous and flat area of about 50x50 km², mainly dedicated to vineyard crops, at about 80 km West of the city of Valencia. The area includes other typical Mediterranean ecosystem species such as shrubs, olive and almond trees and alepo pine forests, being the latter only present in a small mountain formation in the area (Figs. 1 and 2) [3]. According to the land use classification of Fig. 2, and considering that in winter vineyards have the same behaviour as bare soil, we

may assume that the area is composed of about 76.6 % bare soil and 23.4 % vegetation (mainly matorral, shrubs and pine trees) at CERES footprint scale, and of about 33% bare soil and 67% vegetation at GERB footprint scale.

The excellence of the CERES (*Clouds and the Earth's Radiant Energy System*) instrument, particularly its versatile special programmable scanning modes targeting the *Valencia Anchor Station*, has enable us not only to assess the suitability of the site for large scale observations, but also to validate our methodology which clearly has shown to be capable of independently reproducing top of the atmosphere (ToA) CERES SW and LW radiances in a highly extense now dataset of situations [4], including a large variety of surface and atmospheric conditions.



Figure 1. The Valencia Anchor Station

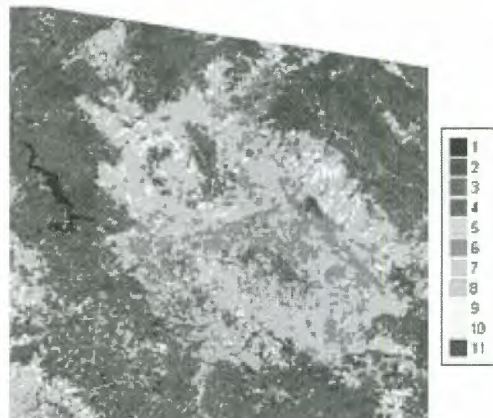


Figure 2. Land use classification of the Valencia Anchor Station area (LANDSAT-TM5 of 5th July 2003). Classes: 1. water, 2. pine trees, 3. low density pine trees and shrubs, 4. shrubs, 5. irrigated crops, 6. vineyards, 7. low density vineyards, 8. very low density vineyards, 9. herbal crops, 10. bare soil, 11. urban areas [6]

3. GERB GROUND VALIDATION CAMPAIGNS

During the three field campaigns, apart from the valuable CERES SW and LW observations, atmospheric and ground measurements were taken by sun photometer, GPS precipitable water content, on-purpose radiosounding ascents, *Anchor Station* operational meteorological measurements including the 4 radiation components at 2m. Mobile stations were used to characterize the rather large extense area, including a mobile air-quality station from the Regional Government of Valencia (*Directorate General for Environmental Quality*) in the February 2004 campaign. The first campaign took place between 18-24 June, 2003, and also included some lidar measurements carried out by the *Electromagnetic Engineering and Photonics Group, Polytechnic University of Catalonia*. The second one developed between 9-12 February, 2004, and the third one between 12-18 September, 2005, included full coverage of a sun-tracking photometer from the *Solar Radiation Group* of the *University of Valencia*. These activities were carried out within the GIST (*GERB International Science Team*) framework.

This paper describes the instrumental set up and deployment during the ground campaigns, the data obtained from the ground, the exclusive CERES PAPS observations over the VAS and the results of analyses and good comparisons between ToA measurements and radiative transfer simulations that confirm the good capabilities of the station to get reliable independent products to be used for the validation of GERB [5]. The work includes a realistic BRDF estimation for the large-scale study area and *Streamer* [6] radiative transfer simulations of ToA SW and LW radiances under clear and cloudy sky conditions. For cloudy sky simulations, MODIS data has been used to get the necessary input cloud parameters.

4. USE OF CERES PAPS OBSERVATIONS AS AN ASSESSMENT OF THE VAS CAPABILITIES FOR VALIDATION OF LOW SPATIAL RESOLUTION DATA AND PRODUCTS

To be able to reproduce CERES observations from independent ground and atmospheric measurements, it is necessary to properly characterize the surface and the atmosphere. The methodology has gradually been developed, first starting with CERES ES8 data [7-8] and is taking its final shape by using the more accurate CERES SSF (*Single Scanner Footprint*) data [9].

In summary, atmospheric profiles needed as input for the *Streamer* simulations are of three types:

- Radiosoundings ascents, generously provided by the *Spanish Meteorological Institute* (INM),

launched on spot, during both *Terra* and *Aqua* CERES overpassing times. The water vapour profile is obtained by scaling total water vapour content to the integrated water vapour measured by the GPS system. The correlation between both set of measurements is really high [7-9]

- Aerosol profile, from *Streamer* Mid-Latitude Winter/Summer (MLW/MLS, depending on the season) standard atmosphere profile, assuming background tropospheric aerosols and background stratospheric aerosols, with the aerosol optical depth obtained from on-ground sun-photometer transmissivity measurements
- Ozone profile, also from *Streamer* MLW/MLS but scaled to the TOMS (*Total Ozone Mapping Spectrometer*) corresponding measurement (<http://toms.gsfc.nasa.gov>)

As far as surface parameters are concerned:

- Surface emissivity [10] is obtained from CERES/SARB (*Surface and Atmospheric Radiation Budget*) database (<http://www-surf.larc.nasa.gov/surf/>)
- Surface temperatures were measured at the VAS and at the mobile stations, weighting up the respective contribution of each one in the whole area by taking into account the land use classification of the study area (Fig. 2)
- Surface BRDF for the whole area is estimated from three contributions, namely broadband albedo weighted from those measured at the VAS and at the mobile station (a_0^{BB}), spectral albedo for the same type of soil from the *ASTER Spectral Library John Hopkins University* (a_λ^{JHU}), and from bidirectional reflectance measurements ($\rho_\lambda(\theta_0, \theta, \phi)$) over bare soil from Ahmad and Deering [11]. See [7-9] for the details

The satellite data used proceed from the specific CERES PAPS acquisitions generously programmed by the *CERES Science Team*. The CERES data finally used are CERES SSF data products which contain CERES PSF (*Point Spread Function*) weighted imager (MODIS) parameters that will be useful to simulate cloudy sky conditions. For Terra FM2, Edition 2B data were used and for Aqua FM3, Edition 1B.

We are here showing results corresponding to the February 2004 campaign with the period 10th to 12th under perfect clear sky conditions as we infer from SSF cloud parameters and from radiation measurements carried out at the VAS. The 9th of February is classified as cloudy with cloud percent cover between 99% and 100% for about 78% of the footprints and between 40% and 99% for the rest of the data. All footprints are classified as one level, liquid water, low cloud with effective pressure above 680 mb, and with optical

thickness over 22.63. Some SSF parameters were selected as inputs for *Streamer* simulations such as

cloud top pressure, cloud optical thickness, cloud effective radius, and cloud liquid water path (Fig. 5).

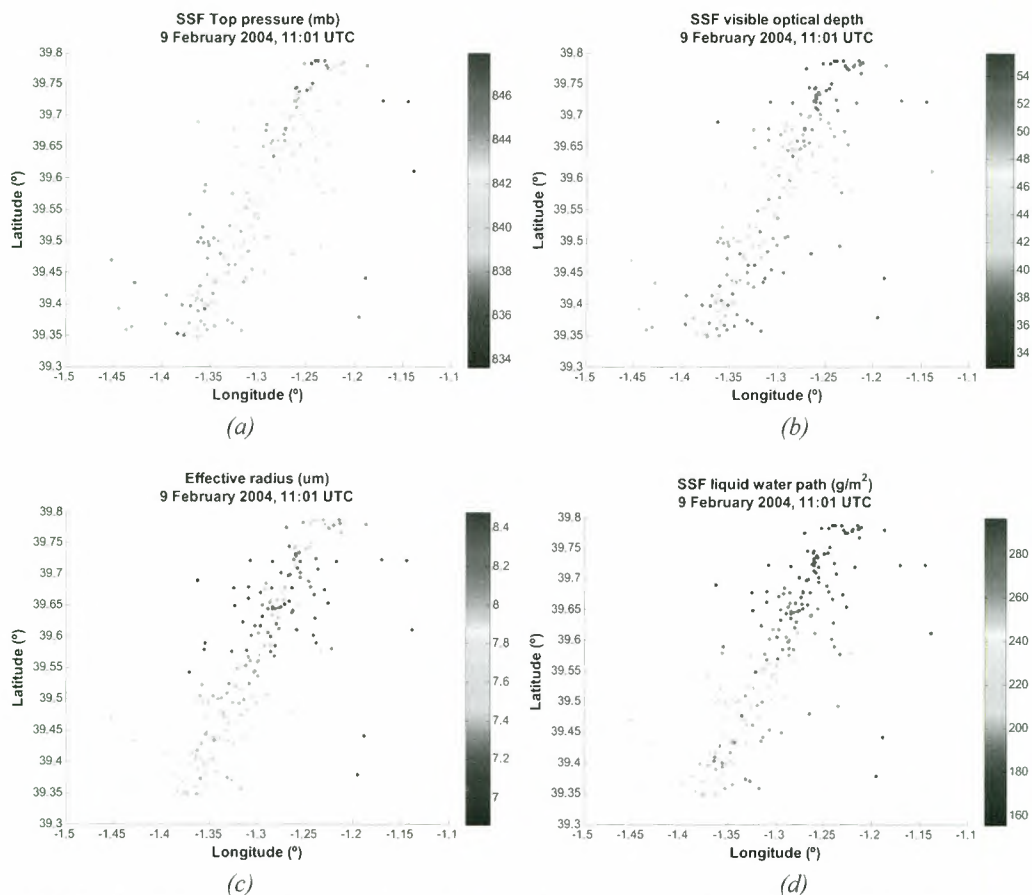


Figure 5. SSF cloud parameter products for the whole $50 \times 50 \text{ km}^2$ area: (a) SSF-93, mean cloud top pressure (mb), (b) SSF-83, mean visible optical depth (c), SSF-103, mean water particle radius, (d) SSF-89, mean liquid water path (g/m^2)

4.1. ToA Radiance Comparisons

A sample of the results of the radiance simulations performed is shown in Figs. 6-8. The left hand side image of each picture shows the observation geometry in a polar plot where we can also see the magnitude of the SW radiances for the full CERES PAPS acquisition pass. The right hand side image of each picture shows the comparison between *Streamer* simulations and CERES ToA radiances (SW and LW). In all cases it is easy to see the radiance anisotropy between the forward and backward scattering directions.

Under clear sky conditions (Figs. 6-7), the agreement is good between satellite data and simulations. In all the cases analysed, the backward radiances are always higher than the forward ones, both in the SW and, less pronounced, in the LW. This anisotropy varies with RAA, with a minimum in the orthogonal plane (plane

where observation and illumination planes are orthogonal) and with a maximum in the principal plane (when those planes are colinear). Anisotropy on clear sky scenes depends on SZA, specially in the SW, being the LW dependence possibly due to changes in boundary layer temperatures during the day [12].

For the cloudy conditions of 9th of February (Fig. 8), we can see that the forward scattering radiances are much higher than the backward ones. The comparison between CERES ToA SW radiances and simulations shows an overestimation of the modeled radiances in the forward scattering direction, being these differences greater as VZA increases. However, there is a really good agreement between CERES ToA LW radiances and *Streamer* simulations. Differences between simulated and measured shortwave radiances may be due to small changes in droplet size that could induce large changes in cloud albedo. Accurate determination of microphysical properties of boundary layer stratus is

essential for the correct treatment of these clouds in radiative transfer and global climate models [13]. It is

definitely necessary to properly measure cloud parameters from the ground.

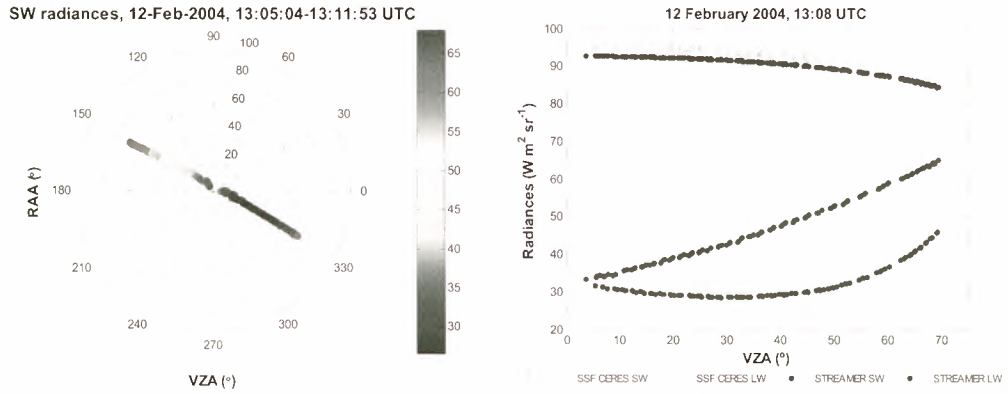


Figure 6. Results for Terra FM2 CERES PAPS observations on 12th February 2004. (Left): CERES ToA SW radiances and observation geometry (almost nadir acquisitions along the full PAPS). Radial axis corresponds to VZA and azimuthal direction to RAA. (Right): Comparison of Streamer simulated ToA radiances to CERES measurements

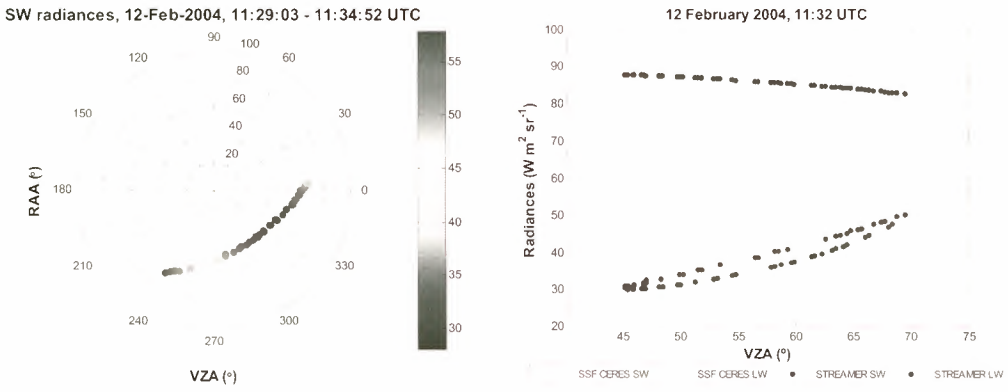


Figure 7. Results for Terra FM2 CERES PAPS observations on 10th February 2004. (Left): CERES ToA SW radiances and observation geometry (quite slant along the full PAPS). Radial axis corresponds to VZA and azimuthal direction to RAA. (Right): Comparison of Streamer simulated ToA radiances to CERES measurements

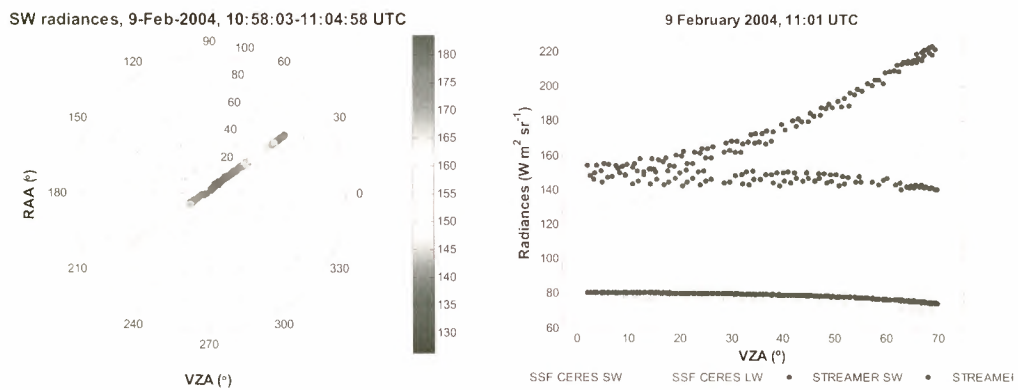


Figure 8. Results for Terra FM2 CERES PAPS observations on 9th February 2004. (Left): CERES ToA SW radiances and observation geometry. Radial axis corresponds to VZA and azimuthal direction to RAA. (Right): Comparison of Streamer simulated ToA radiances to CERES measurements

5. CONCLUSIONS

We have been able to carry out a number of field campaigns addressed to the validation of GERB products. Under clear sky conditions, the *Valencia Anchor Station* has proved to be a good instrument for the ground validation of low spatial resolution remote sensing data and products by being able to reproduce CERES ToA unfiltered radiances from simulations carried out using independent ground measurements of input parameters. In the shortwave, simulated radiances reproduce accurately the anisotropy of the radiance field with RMSEs below $8 \text{ W m}^{-2}\text{sr}^{-1}$. The agreement still improves between simulated and CERES ToA longwave radiances, with RMSEs below $4 \text{ W m}^{-2}\text{sr}^{-1}$. For cloudy conditions, for the shortwave, there is always a slight overestimation in the forward direction. In the longwave, the agreement remains good. Most likely, in the future, the way to improve the results for cloudy conditions in the shortwave, would be by having ground measurements of cloud parameters.

CERES dedicated PAPS observations over the Valencia Anchor Station are of great value to develop the methodology to validate low spatial resolution remote sensing data and products. In this way, the methodology is presently being extended and applied to GERB products, recently been public.

6. ACKNOWLEDGMENTS

The authors thank ESA and EUMETSAT for the selection of this project. They also acknowledge the *Spanish Programme on Space Research (SCALES Project)* and its continuation now as *MIDAS-4/UEG Project* in which context some of the activities will be carried out. The help of the *Regional Government (Directorate General on Environmental Quality)* is appreciated as well for the installation and provision of the Alacant *Anchor Station* and for the use of data from their air quality network.

The authors thank A. Comeron, F. Rocadenbosh and M.Sicard (*Electromagnetic Engineering and Photonics Group, Universitat Politecnica de Catalunya*), J.V. Miró, R. Orts and M. Poquet (*Directorate General for Environmental Quality, Regional Government of Valencia*) and V. Estelles (*Solar Radiation Group, University of Valencia*) for their collaboration in the field campaigns.

6. REFERENCES

1. E. Attema and R. Francis ERS-1, Calibration and Validation, *ESA bulletin* no 65, February 1991

2. J. E. Harries et al. (43 authors more), The Geostationary Earth Radiation Budget Project, *Bulleting American Meteorological Society*, July 2005, 945-960

3. E. Lopez-Baeza, F. Belda, A. Bodas, D. Crommelynck, S. Dewitte, C. Domenech, J.F. Gimeno, J.E. Harries, J. Jorge Sanchez, N. Pineda, D. Pino, A. Rius, K. Saleh, R. Tarruella, A. Velazquez, *SCALES: SEVIRI and GERB CaL/VaL area for large-scale field experiments*. Remote Sensing of Clouds and the Atmosphere VIII. Edited by K. Schaefer, A. Comeron, M.R. Carleer, R.H. Picard, Proceedings of the SPIE, Volume 5235, pp. 134-148 (2004)

4. E. Lopez-Baeza S. Alonso, A. Comerón, R. Diaz-Pabon, C. Domenech, J.F. Gimeno-Ferrer, J. Jorge, A. Labajo, N. Pineda, D. Pino, A. Rius, F. Rocadenbosch, K Saleh, M. Sicard, R. Tarruella, J. Torrobella, and A. Velazquez, *A High-Quality Dataset of Land-Surface and Atmospheric Measurements for the Comparison/Crosscalibration of Data From Large Scale Optical Earth Observation Sensors in Space. The Valencia Anchor Station*. Proceedings of the Workshop on Inter-Comparison of Large Scale Optical and Infrared Sensors. ESA/ESTEC 12-14 October 2004. ESA-WPP-244, Feb. 2005. ESA Publications Division, ISSN No: 1022-6656

5. J.E. Russell (ed.), *GERB Validation Plan. Part 1: Introduction and Overview*. Compiled by J E Russell. Available from Imperial College for Science, Technology and Medicine (ICSTM), (2003)

6. Key, J. and A.J. Schweiger (1998): Tools for atmospheric radiative transfer: Streamer and FluxNet, *Computers & Geosciences*, **24**(5), 443-451

7. A. Velazquez Blazquez, E. Lopez-Baeza, G.L. Smith and Z. Peter Szweczyk, *CERES Operations for the Valencia Anchor Station in Support of GERB Validation Efforts. CERES SCALES Campaigns*. Poster, *13th Conference on Satellite Meteorology and Oceanography, Norfolk, Virginia(US), 20-23 September 2004*
<http://ams.confex.com/ams/pdfpapers/79258.pdf>

8. A. Velazquez Blazquez, S. Alonso, A. Bodas-Salcedo, C. Domenech, J. Gimeno, J. Jorge Sanchez, A. Labajo, N. G. Loeb, D. Pino, A. D. Sanchis, G. L. Smith, Z. P. Szweczyk, R. Tarruella, J. Torrobella, E. Lopez-Baeza, *Comparison of top of the atmosphere GERB measured radiances with independent radiative transfer simulations obtained at the Valencia Anchor Station reference area*. 11th SPIE International Symposium on Remote Sensing, Remote Sensing of

Clouds and the Atmosphere X. Bruges, Belgium, 19–22 September, 2005

9. A. Velázquez Blázquez, S. Alonso, C. Doménech, J. Gimeno, J. Jorge Sanchez, A. Labajo, N.G. Loeb, D. Pino, A. Rius, A. Sanchis, G. L. Smith, Z. P. Szewczyk, R. Tarruella, J. Torrobella, E. Lopez-Baeza, *Use of CERES PAPS observations over the Valencia Anchor Station to validate low spatial resolution remote sensing data and products*. Poster 3.8 in 12th Conference on Atmospheric Radiation / 12th Conference on Cloud Physics, Madison, VI, 9-14 July 2006

10. A.C. Wilber, D.P. Kratz, and S.K. Gupta, *Surface Emissivity Maps for Use in Satellite Retrievals of Longwave Radiation*. NASA/TP-1999-209362

11. S.P. Ahmad, and D. W. Deering, A simple Analytical Function for Bidirectional Reflectance. *J. Geophys. Res.*, **97**, D17, pages 18867-18886

12. P. Minnis, A.V. Gambheer and D. R. Doelling, Azimuthal anisotropy of longwave and infrared window radiances from the Clouds and Earth Radiant Energy System on the Tropical Rainfall Measuring Mission and Terra data. *J. Geophys. Res.*, **109**, D08202

13. N.L. Miles, J. Verlinde, and E.E. Clothiaux, Cloud Droplet Size Distributions in Low-Level Stratiform Clouds. *Journal of Atmospheric Sciences*, Vol **57**, 295-311

RADIOMETRIC CALIBRATION OF THE VISIBLE AND NEAR-INFRARED BANDS OF SEVIRI USING RAYLEIGH SCATTERING AND SUN-GLINT OVER OCEANS

Jean-Marc Nicolas⁽¹⁾, Pierre-Yves Deschamps⁽¹⁾, Olivier Hagolle⁽²⁾

⁽¹⁾ Laboratoire d'Optique Atmospherique, USTL, Bâtiment P5
59655 Villeneuve d'Ascq, FRANCE, nicolas@loa.univ-lille1.fr, pyd@loa.univ-lille1.fr

⁽²⁾ Centre National d'Etude Spatiale, 18 avenue Edouard Belin
31401 Toulouse Cedex 4, FRANCE, olivier.hagolle@cnes.fr

ABSTRACT

Radiometric calibration methods based on clear-sky over ocean natural targets have been applied to three visible and near-infrared bands of SEVIRI sensor on-board MSG1 (now Meteosat-8) satellite. Those methods have been initially developed for in-flight calibration of POLDER sensors [1] and they have been successfully applied to other sensors [2]. An absolute calibration method based on rayleigh scattering is first applied to the 0.6 μm band (VIS 0.6). That calibration is then exported to the 0.8 (VIS 0.8) and 1.6 μm (NIR 1.6) bands using a cross-band calibration method based on sun-glnt reflection. According to error budget analysis the accuracy of the method is below 3 % for VIS 0.6 band and below 5 % for cross-calibrated bands. Application to 2005-2006 data shows excellent stability along time. Calibration correction factors for each of the three bands are proposed.

1. METHODS

We will use in that paper the normalized radiance defined as :

$$R(\theta_s, \theta_v, \varphi, \lambda) = \frac{\pi \cdot L(\theta_s, \theta_v, \varphi, \lambda)}{F_0(\lambda)} \quad (1)$$

where L is the measured radiance and F_0 is the extra-terrestrial solar irradiance corrected from the Sun-Earth distance variations for wavelength λ . θ_s , θ_v , and φ are solar zenith angle, view zenith angle and relative azimuth angle respectively. Geometry and wavelength dependence will be implicit in the rest of the equations of that paper.

1.1 Absolute calibration on rayleigh scattering

Atmospheric rayleigh scattering, i.e. scattering by molecules, can be exactly computed for any wavelengths and any viewing geometries using radiative transfer code [3]. Calibration correction factor can then be computed by comparison with Top Of the Atmosphere (TOA) sensor measurements. The signal becomes very small for wavelength above 0.7 μm but it ranges from 2 to 5 % of maximum dynamic for the VIS 0.6 band of SEVIRI, which is enough for calibration purposes if the linearity of the sensor is well-characterized.

The main uncertainty for such a method is the contribution of aerosol scattering. That perturbation can be roughly corrected using a maritime aerosol model coupled with VIS 0.8 band measurement when aerosol charge is low as long as continental aerosol or highly charged situations are correctly discarded (areas and pixels selection). Gaseous absorption and water leaving reflectance contribution are accounted for using meteorological analysis and climatologies. Error budget analysis is developed below.

The TOA clear sky normalized radiance over ocean for VIS 0.6 can be written as :

$$R_{TOA} = [R_{ray} + R_{aer} + R_{gli} + R_w] \cdot T_{O3} \quad (2)$$

where R_{ray} accounts for rayleigh scattering, R_{aer} accounts for aerosol scattering including coupling terms, R_{gli} is the TOA sun-glnt reflection and R_w is the TOA water leaving radiance contribution. T_{O3} is the ozone absorption transmission factor. R_{ray} can be exactly computed knowing the spectral filter response and after adjustment by the surface pressure (ECMWF analysis data). That term is about 90 % of the observed signal for very clear situations. R_{gli} is very small for geometries off the specular direction that can be easily selected. R_w is below one Digital Count (DC) at 0.6 μm over clear open ocean waters. It is computed using mean oligotrophic conditions (chlorophyll concentration = 0.05 $\text{mg}\cdot\text{m}^{-3}$) and a bio-optical model

[4]. T_{O3} can be estimated with enough precision using stratospheric ozone contents from other sensors (TOMS, OMI, GOME) or from ECMWF analysis data.

The R_{aer} term cannot be simulated from mean geophysical conditions because aerosols are highly changeable in both charge and type from one day to another. An algorithm has to be implemented to correct for that perturbation. We used the VIS 0.8 band both to select pixel with low aerosols and to retrieve aerosols contribution. In that band open ocean is black, so we can write that aerosol scattering term at 0.8 μ m is :

$$R_{aer}^{VIS08} = \frac{[R_{mes}^{VIS08} - R_{ray}^{VIS08}]}{T_{H2O}^{VIS08}} \quad (3)$$

If we suppose a fixed aerosol model according to open oceans conditions far from any continental aerosols sources, we can then extrapolate that terms to VIS 0.6 band and compute a simulated TOA signal with :

$$R_{simu}^{VIS06} = [R_{ray}^{VIS06} + \epsilon_{aer} \cdot R_{aer}^{VIS08} + R_w]. T_{O3} \quad (4)$$

R_{ray} and R_{aer} are pre-computed for each geometry and wavelength using a radiative transfer code and we store them in Look-Up Tables (LUT). For aerosol we choose a maritime model with 98 % of relative humidity (M98 model) according to Shettle and Fenn [5] approach with Aerosol Optical Thicknesses (AOTs) ranging from 0 to 0.1 by step of 0.02. AOT really used is interpolated from VIS 0.8 measurements and LUT at 0.8 μ m. Tab. 1 summarizes all those simulation conditions.

<i>Geophysical conditions</i>	<i>value</i>
VIS 0.6 rayleigh optical thickness	0.0533
VIS 0.8 rayleigh optical thickness	0.0204
NIR 1.6 rayleigh optical thickness	0.0014
Aerosol model	M98
Aerosol optical thickness (865 nm)	from 0 to 0.1
Chlorophyll	0.05 mg/m ³

Table 1. Geophysical conditions for simulations

Calibration bias on VIS 0.8 will affect that calculation, but one must keep in mind that aerosol term remains small and is nothing but a perturbation. Geographical areas and pixels selection help us to be sure that real conditions fit well the ones we simulated.

1.2. Crossband calibration on sun-glint

Sun-glint (the fresnel reflection of sun light on the air-sea interface) can be used as a spectrally flat target to calibrate one spectral band according to another. Here we will use the VIS 0.6 band after adjustment from rayleigh scattering method as reference, and cross-calibrate VIS 0.8 and NIR 1.6 bands. Sun-glint signal ranges from 10 to 40 % of maximum dynamic for each of the three bands, which is almost perfect for calibration purposes. High, thick clouds also could be considered as white, spectrally flat targets in the visible, but at 1.6 μ m ice clouds absorption is far greater than liquid clouds absorption. Crossband calibration of NIR 1.6 band is then impossible with clouds.

Once again we have to deal with atmospheric perturbation which is far from being spectrally flat. First we inverse aerosol contents using a MSG slot off the sun-glint, a couple of hours before, using VIS 0.6 band. The aerosol term :

$$R_{aer}^{VIS06} = \frac{[R_{mes}^{VIS06} - R_{ray}^{VIS06} - R_w]}{T_{O3}^{VIS06}} \quad (5)$$

is used against LUT to estimate the AOT. Then we used the sun-glint slot to make a pseudo-wind speed inversion using dedicated LUT of the TOA sun-glint signal using Cox & Munk model [6] and radiative transfer code. For the given geometry and AOT, the LUT is used to compute the wind speed that fit the measurement at VIS 0.6. That wind speed is then used to interpolate the signal at the other bands (VIS 0.8 and NIR 1.6) using the LUT. Fig. 1 shows an example of the process. The use of a sun-glint model allowed us to account for the slight spectral dependence of the index of refraction of seawater from 0.6 to 1.6 μ m [7][8].

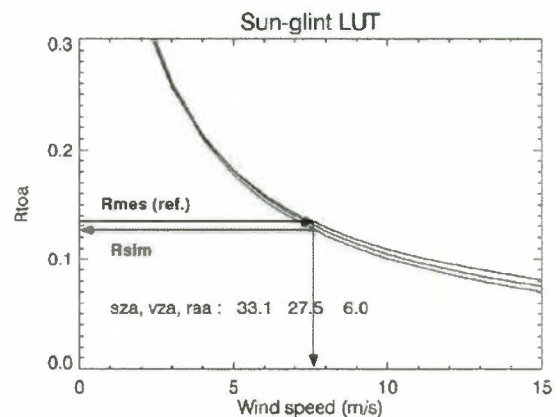


Figure 1. Example of sun-glint LUT for VIS 0.6 (black) VIS 0.8 (blue) and NIR 1.6 (red). Measurement at VIS 0.6 is used to invert a wind-speed that is then used to interpolate the simulated signal at VIS 0.8 and NIR 1.6.

2. ERROR BUDGET

Rayleigh scattering can be exactly computed using a Successive Order of Scattering code [3]. A surface pressure correction can be performed. 10 mB uncertainty on surface pressure leads to a 1 % uncertainty on A_k .

Water reflectance is very small and constant for clear waters at 0.6 μ m and water is black for other bands. Coastal and eutrophic waters will be discarded. 1% uncertainty.

Aerosols : That is the main uncertainty because aerosols are highly variable. Previous simulation [1] shows that aerosol models variability leads to an error of 1% and that calibration error of 5 % of VIS 0.8 band used for correction leads to another 1% error. Maximum error : 2 %

Surface roughness : That leads to sun glint contamination of the sequence. Those contaminated pixels can be discarded using geometric selection.

Gaseous absorption : ECMWF analysis data give ozone amount with a 5 % precision. That leads to a 0.5 % uncertainties on the simulated top of atmosphere radiance for VIS 0.6. For water vapour absorption we used a mean atmospheric profile (US62) which leads to larger errors of about 3 % for VIS 0.8 and NIR 1.6 calibration factors.

For cross-band method, the error on the reference band has of course an impact on the total error.

Total (quadratic) rayleigh method : ~ 3 %

Total (quadratic) sun-glnt method : ~ 5 %

3. AREAS AND PIXELS SELECTION

Calibration process does not have to deal with as much pixels as possible. Strict selection criteria has to be applied in order to be sure that geometric, geographic and geophysical conditions are fulfilled. That implies two way of selection : a first one on geographical criteria, i.e. areas selection, a second one on thresholds apply to the measurements itself.

3.1. Areas selection

We have selected three areas for rayleigh scattering method based on different signal dynamic available for each area, on the probability to have low aerosol charge above those areas (aerosol climatologies) and over oligotrophic basins in order to minimize marine reflectance impact. We do not select disc edges to avoid

earth curvature effect. Fig. 2 shows those three areas.

South Atlantic (area 1) : Large area without aerosols. Clear waters. The level of the measured signal is low because the air mass is low.

Sargasso Sea (area 2) : Very clear waters area with high signal level. Dust outbreaks from Africa (february, march) should be carefully discarded .

Indian ocean (area 3) : Small area with high signal level, but in the border of SEVIRI field of view.



Figure 2. Selected areas for rayleigh scattering method

For sun-glnt method, area is necessary centered on the maximum of the sun-glnt signal for the chosen slot. It means the selection is driven by geometric conditions only. That maximum is available of course only over oceans and it is moving from east to west along the day and from north to south along the year. It is located in northern atlantic, off Africa, from march to september (possibility of dust contamination) and in southern Atlantic from september to march. Fig. 3 shows an example of the location of that maximum.



Figure 3. Example of sun-glint area for 16:00 slot of the 23th of august, 2005

3.2. Pixels selection

The objectives of the selection are thrice :

- clouds masking. A simple local (3x3 neighborhood) standard deviation threshold on VIS 0.8 measurement is enough for both rayleigh or sun-glint method. $\sigma_{3 \times 3} < 0.005$.
- low aerosol charges. Sun-glint free slots are used, and thresholds on $R_{aer} < 0.008$ and on inverted AOT < 0.06 are applied.
- sun-glint mask control (for rayleigh method). A threshold on maximum wind speed (ECMWF data) is applied : wind speed < 5 m/s. Foam contamination pixels are also discarded with that threshold.

4. RESULTS

We will mostly use in the results presentation the calibration correction factor that is defined for each band k as :

$$\Delta A_k = \frac{R_{mes}^k}{R_{simu}^k} \quad (6)$$

as the main objective of that study is to evaluate the standard, operational calibration of SEVIRI data (level 1.5). However, when signal dynamic allows it, inversion of a simple but full radiometric model (slope + offset) is possible :

$$R(\lambda) = \frac{(DC - DC0)}{slope} \quad (7)$$

4.1. Example on one scene

Fig. 4a shows an example of simulated against measured signal at 0.6 μ m for one SEVIRI slot (10:00 UT) and for all selected pixels of the three areas. Standard deviation is slightly above the 3 % of our error budget mainly because that error also includes instrumental (radiometric + digitize) errors. Fig. 4b shows simulated against Digital Counts for the same case : linear regression shows good results and we could be fairly confidence in the two inverted parameters of our simple radiometric model.

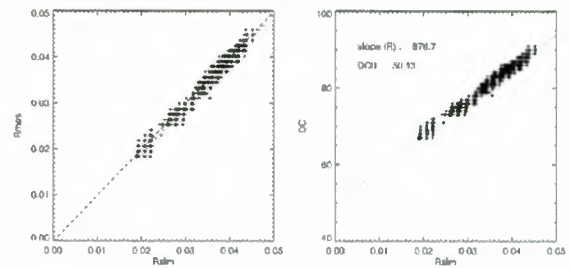


Figure 4. Simulated signal at VIS 0.6 using rayleigh scattering method against : a) Measurements using operational calibration parameters. b) Digital Counts.

Fig. 5 shows an example of crossband calibration on sun-glint for VIS 0.8 and NIR 1.6 bands, using VIS 0.6 as a reference (the calibration of VIS 0.6 as been adjusted according to rayleigh method results other one year, see §4.2.)

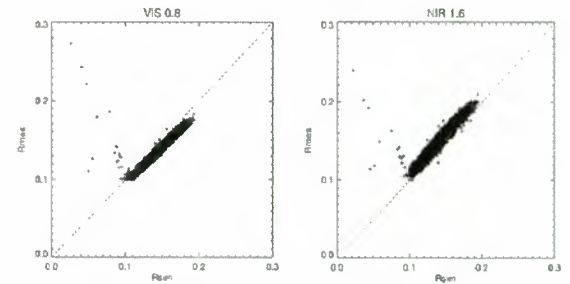


Figure 5. Simulated against measured signal at VIS 0.8 and NIR 1.6 bands using crossband method on sun-glint with VIS 0.6 band as reference (after calibration adjustments from rayleigh method results)

4.2. Results over one year

We have applied the rayleigh method on the 10:00 (Universal Time) slot for each day from June 2005 to June 2006, using MSG data received with EumetCAST system. The results for each area are shown in fig. 6 and they show remarkable stability along time. The mean calibration correction factors for the three areas show excellent consistency (within 3 %) though geometries (i.e. dynamics) are very different. It should be noticed that August-September period for area 1 and December-January period for area 2 are more noisy because solar zenith angle is very low, which means low solar irradiance and low signal. Lower limits should be raised in order to discard those situations in future processings.

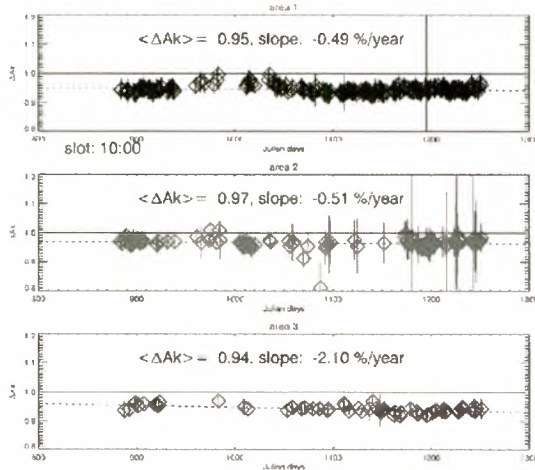


Figure 6. Correction calibration factor (eq. xxx) of VIS 06 band from rayleigh method for the three areas from June 2005 to June 2006. Julian days are computed since the 1st of January, 2003.

Merging results of the three areas are shown in fig 7. A small trend of about 1% per year could be observed, but it is within error budget, as well as the small seasonal effect (minimum observed in winter, maximum in summer). The main conclusion is that actual L1.5 normalized radiance of VIS 0.6 band shows an underestimation of 5% according to our rayleigh absolute calibration method. That bias has been corrected before application of the cross-band calibration method.

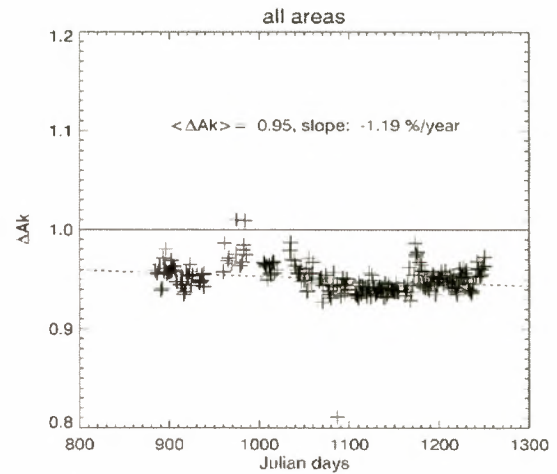


Figure 7. Final merged results for rayleigh calibration method. A small trend of about 1% per year is observed, as well as a seasonal effect. Both of them are within the error budget of the method.

For cross-band on sun-glint method, we have proceeded differently: we have visually selected one sun-glint slot other than the Atlantic (at 16:00 UT) for each month to be sure we are far from dust plumes or out of heavy or broken cloud cover. Automated process will be implemented in the future but that requires more work in order to be certain of thresholds adjustments and cloud masking algorithms. Results are shown in Fig. 8. From March to June 2006 we found no aerosol-free sun-glint scenes. Calibration correction factors show large variability that could be acknowledged for:

- rough water vapor absorption correction scheme. Use of integrated water vapor content from ECMWF data should improve that correction.
- permissive cloud mask that does not account for clouds shadow.

Those two points can be easily improved in a near future.

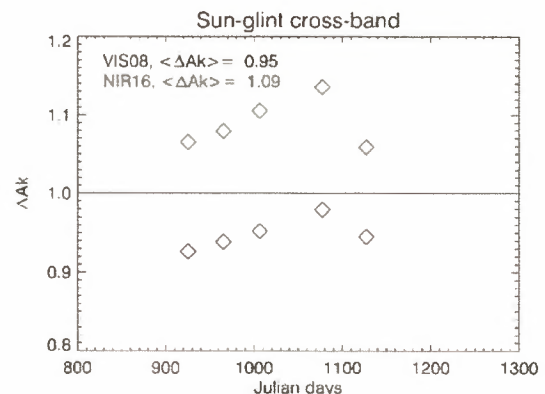


Figure 8. Sun-glint method results. No data are available from March to June 2006 period (dust contaminated). Variability from one month to another

could be reduced by improvements of the method.

But despite those limits the results are reliable enough and they show an underestimation of 5 % of the VIS 0.8 band and an overestimation of 10 % of the NIR 1.6 band. It should be noticed that those results come from VIS 0.6 band absolute calibration after a 5 % correction (the actual L1.5 radiance has been increased by a factor of 1.05) according to rayleigh calibration method results. Tab. 2 resumes those results.

	DA	DC0	slope
VIS 0.6 (rayleigh)	0.95	50.1	870.0
VIS 0.8 (sun-glnt)	0.95	NA	NA
NIR 1.6 (sun-glnt)	1.09	NA	NA

Table 2. Calibration correction factors and calibration coefficients for the three SEVIRI bands.

5. CONCLUSIONS

The absolute radiometric calibration method based on atmospheric rayleigh (or molecular) scattering has been successfully applied to SEVIRI VIS 0.6 band though on the lowest part of signal dynamic. It shows a 5 % underestimation of the L1.5 radiance for that band. If the linearity response of the sensor is confident enough that result can be exported to VIS 0.8 and NIR 1.6 SEVIRI bands by applying a crossband method based on sun-glnt. Preliminary results of that method show a 5 % underestimation of VIS 0.8 band and a 10 % overestimation of the NIR 1.6 band (in radiance). Pixels selection process as well as water vapor absorption correction should be improved in a near future in order to increase the accuracy of the method from the current 5 % to about 3% as shown by error budgets.

ACKNOWLEDGMENTS

MSG1/SEVIRI data were received with the EumetCAST system and archived at LOA and ICARE.

Data processing chain makes use of the SPT toolbox in IDL provided by Eumetsat.

REFERENCES

1. Hagolle O., et al. Results of POLDER In-Flight Calibration, *IEEE Trans. Geosci. Remote Sensing*, 1999, vol. 37, pp.1550-1566
2. Hagolle, O., et al., Absolute calibration of VEGETATION derived from an interband method based on the sun-glnt over ocean, *IEEE Trans. Gesc. Rem. Sens.*, 2004, Vol. 42, 7, 1472-1481
3. Deuzé, J.-L., et al., Fourier series expansion of the transfer equation in the atmosphere-ocean system, *J. Quant. Spectrosc. Radiat. Transfer*, 41, 483-494, 1989
4. Morel, A., and S. Maritorena. Bio-optical properties of oceanic waters: A reappraisal. *Journal of Geophysical Research*, 2001, 106: 7163-7180
5. Shettle, E. P., and R. W. Fenn, Models for the aerosols of the lower atmosphere and the effects of humidity variations on their optical properties, *AFGL-TR-79-0214*, No 676, 1979
6. Cox, C. and W. Munk, Measurement of the roughness of the sea surface from photographs of the sun's glitter, *J. Opt. Soc. Am.*, 44, 11, 838-850, 1954
7. Quan, X. and Fry, E.S., Empirical equation for the index of refraction of seawater, *Applied Optics*, 1995, Vol 34, 18, 3477-3480
8. Huibers, P. D. T., Models for the wavelength dependence of the index of refraction of water, *Applied Optics*, 1997, Vol. 36, 16, 3785-3787

MSG SEVIRI APPLICATIONS FOR WEATHER AND CLIMATE: CLOUD PROPERTIES AND CALIBRATIONS

Patrick Minnis⁽¹⁾, Louis Nguyen⁽¹⁾, William L. Smith⁽¹⁾, Rabindra Palikonda⁽²⁾, David R. Doelling⁽²⁾
J. Kirk Ayers⁽²⁾, Qing Z. Trepte⁽³⁾, Fu-Lung Chang⁽⁴⁾

⁽¹⁾NASA Langley Research Center, MS 420, Hampton, VA 23681 USA, Email: p.minnis@nasa.gov

⁽²⁾AS&M, Inc., 1 Enterprise Parkway, Hampton, VA 23666 USA, Email: d.r.doelling@larc.nasa.gov

⁽³⁾SAIC, 1 Enterprise Parkway, Hampton, VA 23666 USA, Email: q.z.trepte@larc.nasa.gov

⁽⁴⁾National Institute of Aerospace, 100 Exploration Way, Hampton, VA 23666 USA, Email: fchang@nianet.org

ABSTRACT

SEVIRI data are cross-calibrated against the corresponding *Aqua* and *Terra* MODIS channels. Compared to *Terra* MODIS, no significant trends are evident in the 0.65, 0.86, and 1.6 μm channel gains between May 2004 and May 2006, indicating excellent stability in the solar-channel sensors. On average, the corresponding *Terra* reflectances are 12, 14, and 1% greater than their SEVIRI counterparts. The *Terra* 3.8- μm channel brightness temperatures T are 7 and 4 K greater than their SEVIRI counterparts during day and night, respectively. The average differences between T for MODIS and SEVIRI 8.6, 10.8, 12.0, and 13.3- μm channels are between 0.5 and 2 K. The cloud properties are being derived hourly over Europe and, in initial comparisons, agree well with surface observations. Errors caused by residual calibration uncertainties, terminator conditions, and inaccurate temperature and humidity profiles are still problematic. Future versions will address those errors and the effects of multilayered clouds.

1. INTRODUCTION

The Meteosat Second Generation (MSG) 3-km resolution Spin-Enhanced Visible Infrared Imager (SEVIRI) provides the opportunity to monitor weather systems throughout the diurnal cycle with unprecedented temporal and spatial resolution using a combination of spectral channels heretofore available only on lower Earth-orbiting (LEO) satellites. For the past 7 years, a set of algorithms has been applied to data from high-resolution LEO satellite imagers for the Clouds and Earth's Radiant Energy System (CERES) Project [1] and from the 4-km resolution, 5-channel Geostationary Operational Environmental Satellite (GOES) imager over the United States (US) [2]. The CERES algorithms use up to 8 channels on the 32-channel Moderate Resolution Imaging Spectroradiometer (MODIS) on *Aqua* and *Terra*, but only 4 channels from GOES. The upcoming generation of GOES, the GOES-R series, will be more like the SEVIRI than its predecessors. Thus, to determine how well the CERES algorithms work on geostationary satellites using more than 4 channels to help prepare for

the use of the future GOES-R, to evaluate the algorithms over a full range of conditions, and to develop algorithm improvements, among other objectives, this MSG RAO effort has been designed to apply the CERES algorithms to SEVIRI data and evaluate and refine the results. To obtain consistency with retrievals from the other satellites, it is necessary to ensure that the satellites are properly intercalibrated. Previous studies presented initial intercalibrations [3] and cloud retrievals over a European domain [4] results from early MSG data. Progress in improving the calibrations and retrievals has continued and is reported here. The retrievals are currently being performed over a European domain each hour. To validate the retrievals, results over the Chilbolton, UK and Cabauw, Netherlands, surface sites are compared with similar quantities derived from active and passive sensors.

2. DATA

The calibrations are performed using *Meteosat-8* SEVIRI and *Terra* and *Aqua* MODIS data taken from April 2004 through May 2006. The SEVIRI (MODIS) channels of interest are the visible (VIS) 0.64 (0.64) μm , 0.80 (0.86) μm , near-infrared (NIR) 1.62 (1.62) μm , the solar-infrared (SIR) 3.9 (3.8) μm , 8.7 (8.6) μm , infrared (IR) 11.0 (10.8) μm , split-window (SWC) 12.0 (12.0) μm , and CO₂ 13.3 (13.3) μm bands. An additional comparison is performed using the GOES-12 SIR channel. The satellite detection and retrieval of single-layer cloud properties use the VIS, NIR, SIR, IR, and SWC channels. Multilayered cloud retrievals also use the CO₂ channel. Efforts to utilize the 8.7- μm channel are underway. Data from the European domain, extending from 30°N to 55°N and from 12°W to 30°E, are analyzed each hour at 6-km resolution obtained by sampling every other pixel and scan line. The Western Europe domain (39°N - 54°N; 4°W - 17°E) is analyzed at the 3-km resolution for better comparisons with ground site data. The data are analyzed in near-real time, but display is delayed for 24 hours. The auxiliary data needed for analysis include temperature, humidity and ozone profiles from the 6-hourly 1.25° NOAA Global Forecast System (GFS) analyses. Other input datasets are described by [4].

3. METHODOLOGY

3.1. Calibration

The calibrations were performed following the methods of [5] and [6]. Collocated and matched *Terra* MODIS and SEVIRI pixels taken over ocean were averaged to 0.5° regions using a 30° x 20° grid box near the M8 sub-satellite point. The data matched if the differences Δ in solar zenith, viewing zenith, and relative azimuth angles and time meet the following criteria:

$$\Delta \text{SZA} < 15^\circ, \Delta \text{VZA} < 10^\circ, \Delta \text{RAZ} < 15^\circ, \Delta t < 15\text{min},$$

respectively. No data taken in sunglint are used. For the purposes of intercalibrating, it is assumed that the corresponding MODIS and SEVIRI channels have the same filter function. The time differences are taken in to account using the ratios of $\cos(\text{SZA})$. Spectral differences were not taken into account in the intercalibrations.

When a one month of data have been acquired, the SEVIRI solar channels are calibrated in terms of the MODIS radiance,

$$L_M = a [C(M8) - C_o(M8)] F_o(M) / F_o(M8) \quad (1)$$

where a is the gain, C is the observed 10-bit count, C_o is the space count, F_o is the spectral solar constant, M refers to MODIS, and $M8$ refers to SEVIRI. For all channels with wavelengths exceeding 2.0 μm , the radiances are fit in terms of the brightness temperatures,

$$T_M = b T_{M8} + b_o, \quad (2)$$

where b is the slope and b_o is the offset. The mean differences, $T_{M8} - T_M$, are also computed each month to measure trends in SEVIRI channels because trends in the slopes can offset by opposite trends in the offsets.

3.2. Cloud Properties

Cloudy pixels are detected with a version of the CERES Cloud Mask [1, 2, 4] and the corresponding cloud properties are retrieved using the suite of CERES cloud property retrieval algorithms that include the VIS-IR-SIR-SWC Technique (VISST) during the daytime, the SIR-IR-SWC Technique (SIST) at night [7], and the SIR-IR-NIR Technique [8] during the day over snow-covered surfaces. The retrievals use a consistent set of models characterizing water droplet and hexagonal ice column reflectances and emittances [9] within a set of parameterizations [10]. The resulting output for each pixel in every image includes many different parameters, such as latitude (LAT) and longitude (LON), that are summarized in Tab. 1. The results for each image are stored digitally and used to create images of each parameter for the specific domain. These images as well as the archived data can be accessed via the Internet at <http://www-angler.larc.nasa.gov/satimage/products.html>. At that web page, the data for

Table 1. VISST output parameters for each pixel

LAT, LON, SZA, VZA, RAZ
Scene ID (Clear or Phase)
Clear-sky effective temperature
Cloud effective temperature
Cloud effective height and pressure
Cloud top height
Cloud thickness (base height)
Cloud emissivity
Cloud water droplet effective radius or ice effective diameter
Cloud optical depth
Cloud liquid water or ice water path
Broadband SW albedo & LW flux
Aircraft icing index
Reflectance or temperature at 0.64, 3.9, 10.8, 12.0, 13.3 μm

the European domain can be accessed through the link, “EUROPE”. Figure 1 shows an example of the “EUROPE” web page for image time 0900 UTC, 13 June 2006. The RGB image is displayed for the most recent analysis that is available. Links to the Western Europe domain and to averaged properties for five different ground sites in Europe are provided on the page. The images for any parameter at any time when data were analyzed using a pull-down menu that allows control of the parameter, number of images, and starting. Either one or four variables can be displayed and looped. Archived digital data and other satellite cloud products can be accessed via links listed on the page.

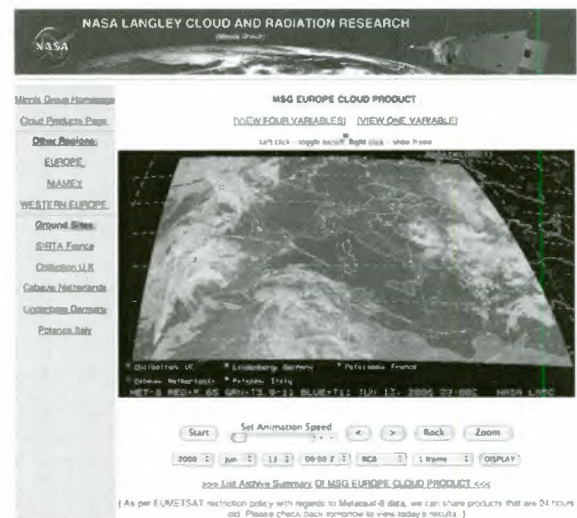


Figure 1. Example of European domain web page accessed via “EUROPE” link.

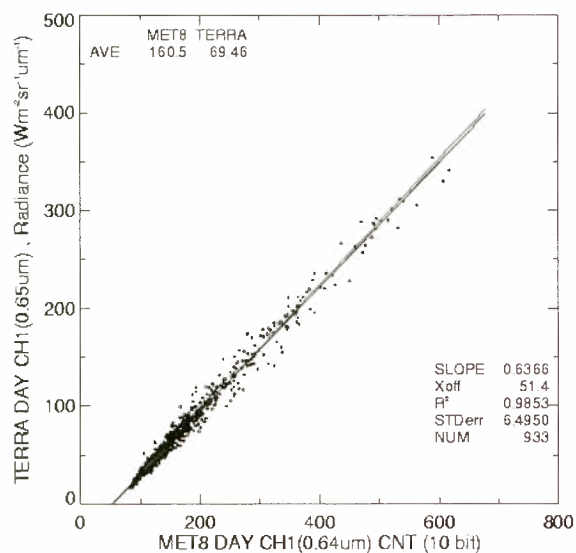


Figure 2. Terra MODIS radiance as function of SEVIRI VIS count, November 2005.

4. RESULTS

4.1. Calibrations

Fig. 2 shows the scatterplot and linear regression fit using the Terra VIS channel during November 2005. The scatter is relatively minor, except at the brighter end of the range. The resulting slope and offset are 0.6366 and 51.4, respectively. The offset is very close to the nominal space count of 51.0. Similar plots and fits were made for each month during the period for all of the solar channels and used to estimate the trends in the gains and offsets. The mean slopes are listed in Tab. 2 along with the mean gains provided operationally by EUMETSAT. The result in Fig. 2 is typical for the VIS channels. The mean gain from *Terra* is $0.639 \text{ W m}^{-2} \text{ sr}^{-1} \mu\text{m}^{-1}$, a value that is 11% greater than the operational value. The mean offset count is 52.1. The respective results from *Aqua* are nearly identical at $0.637 \text{ W m}^{-2} \text{ sr}^{-1} \mu\text{m}^{-1}$ and 52.5. No statistically significant trend was found in either set of gains. Based on radiative transfer calculations, it is expected that the MODIS reflectance should be only 2.1% greater than the SEVIRI value for a given ocean scene. Given that MODIS has an onboard calibration system, these results suggest that the SEVIRI VIS channels could be too dark by 9%. This corrected VIS calibration is used in the cloud retrievals.

Table 2. Mean gains in SEVIRI solar channels from EUMETSAT and Terra, May 2004 – May 2006.

Channel μm	EUMETSAT $\text{W m}^{-2} \text{ sr}^{-1} \mu\text{m}^{-1}$	<i>Terra</i> $\text{W m}^{-2} \text{ sr}^{-1} \mu\text{m}^{-1}$	Difference (%)
0.64	0.573	0.639	11.5
0.80	0.453	0.518	14.3
1.62	0.088	0.089	1.1

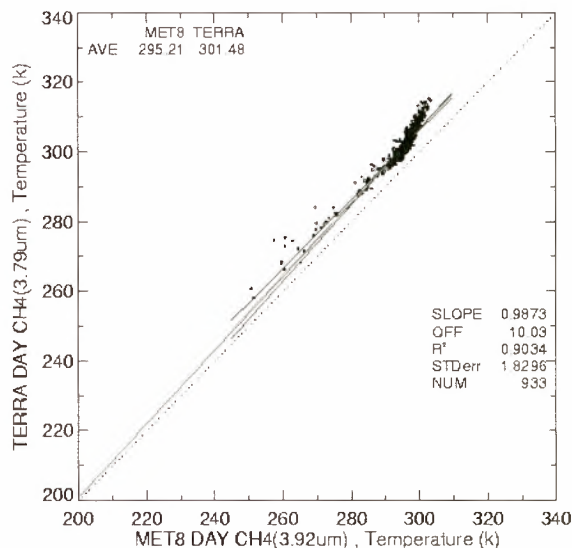


Figure 3. Terra MODIS SIR temperature as function of SEVIRI SIR temperature, daytime, November 2005.

No trends were found in any of the other solar channels. However, the MODIS 0.86- μm reflectance averages 14.3% more than the SEVIRI 0.81- μm reflectance (Tab. 2). That difference may be entirely due to spectral differences and will require additional study to determine if it is significant. The mean offset is 52.9. The differences in the NIR channel are negligible. The SEVIRI band is considerably wider than the MODIS channel, but both are symmetrically centered on the same wavelength. The mean NIR offset is 51.3 counts.

Fig. 3 shows the November 2005 daytime correlation of the SIR channels, which indicates that the MODIS temperatures are 6 K greater, on average. The result is quite typical as indicated in Tab. 3. At night, the relationship changes and the difference between the two channels decreases. Comparisons with the GOES-12 channel (not shown) yields the same results during both day and night; the GOES temperatures average 3.1 K greater than their SEVIRI counterparts. Good agreement is found at $T < 260 \text{ K}$ in both instances. Differences in the other channels are much smaller, as indicated in Tab. 3, especially for the IR and SWC channels. The SEVIRI CO_2 channel is much broader than for MODIS.

Table 3. Linear fits and differences between SEVIRI and Terra brightness temperatures, May 2004 - May 2006.

Channel (μm)	Slope	Offset	Diff (K)
3.90 (day)	1.125	-30.1	-6.67
3.90 (night)	1.041	-8.02	-3.73
8.60	0.982	5.74	-0.45
10.8	1.008	3.09	0.70
12.0	1.010	3.28	0.45
13.3	0.955	10.5	1.52

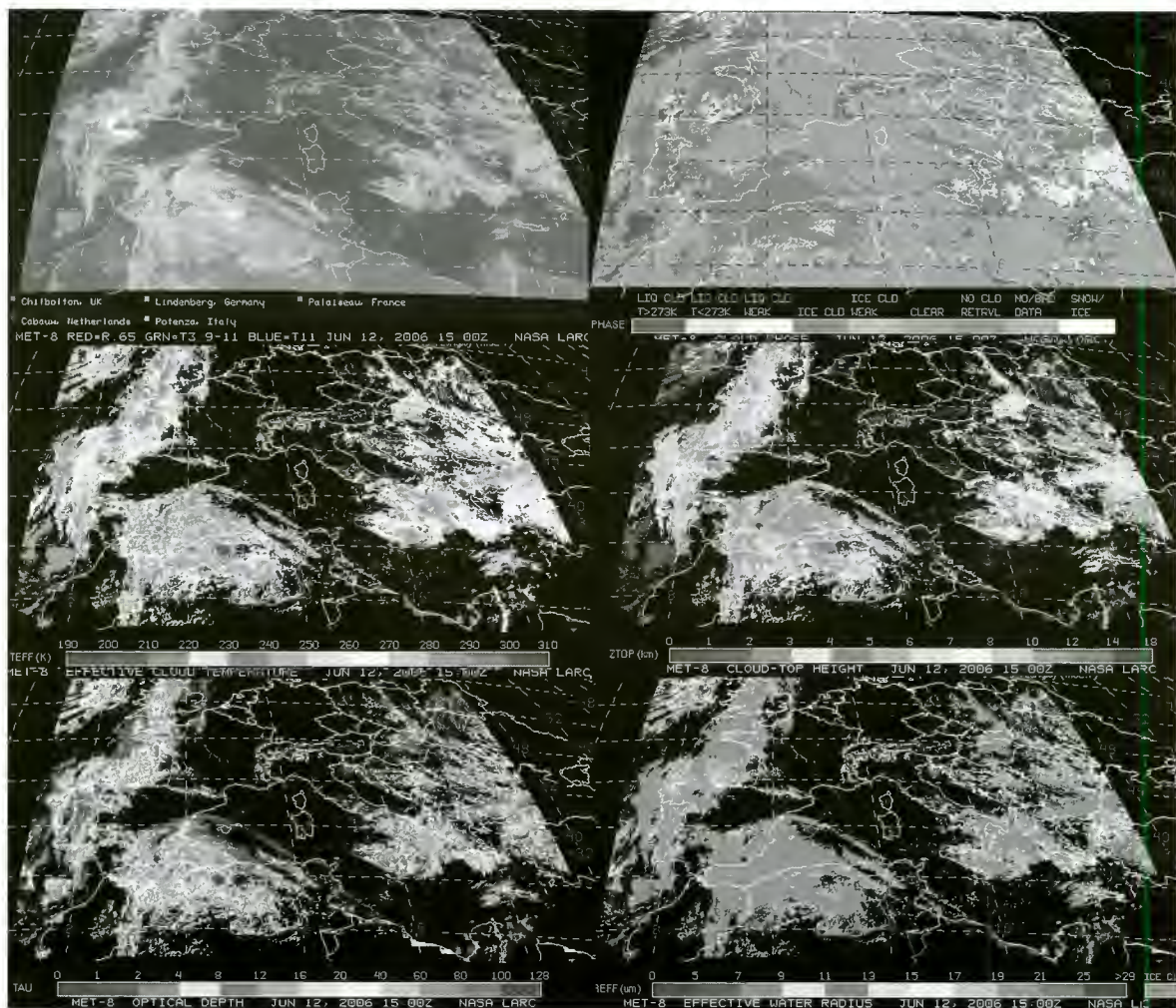


Figure 4. Example of products from cloud retrieval, 1500 UTC, 12 June 2006. Clockwise from top right: RGB image, phase, cloud-top height, water droplet effective radius, cloud optical depth, and cloud effective temperature.

4.2 Satellite Products & Access

Examples of several product images are shown in Fig. 4 for 1500 UTC, 12 June 2006. A frontal system with ice clouds on top is passing over the British, French, and Iberian coasts, while cirrus and other ice clouds indicate a low pressure system over Algeria. Cloud top heights reach up to 14 km over Algeria. The effective droplet sizes are generally between 9 and 11 μm except for some smaller values off the Moroccan coast and north of Libya. The greatest optical depths are seen over Algeria, southern Italy, and northwestern Spain. Clouds with tops between 1 and 2 km cover Ireland. These results are fairly typical. Some of the thinner clouds are not detected and a few false clouds are generated along the north African coasts. In some instances, a given 0.5° box is classified as a clear whenever the GFS temperature profiles are in error or the clear-sky temperatures or albedo are not properly characterized. Other errors are produced whenever the SZA is between 85 and 90° because the SIR signal is insufficient.

4.2 Validation

The cloud products can be assessed visually by examining images of the results and the radiances together. That approach yields a qualitative evaluation that identifies many gross errors. Comparisons with objective measurements from the surface or from aircraft is more valuable for obtaining a quantitative verification of the results. The initial evaluations [4] used data taken at the SIRTAsite in Palaiseau, France and from automated surface observing systems across Europe. Here, the active and passive sensors at Chilbolton, UK and Cabauw, Netherlands are used to assess a few of those parameters at those sites, which are indicated on the RGB image in Fig. 4. The Cabauw cloud radar is used in preliminary manner to assess the cloud boundaries, while the Chilbolton ceilometer is used to assess cloud base for single-layer clouds and the LWP derived from the microwave radiometer is compared to the same parameter derived from SEVIRI using VISST.

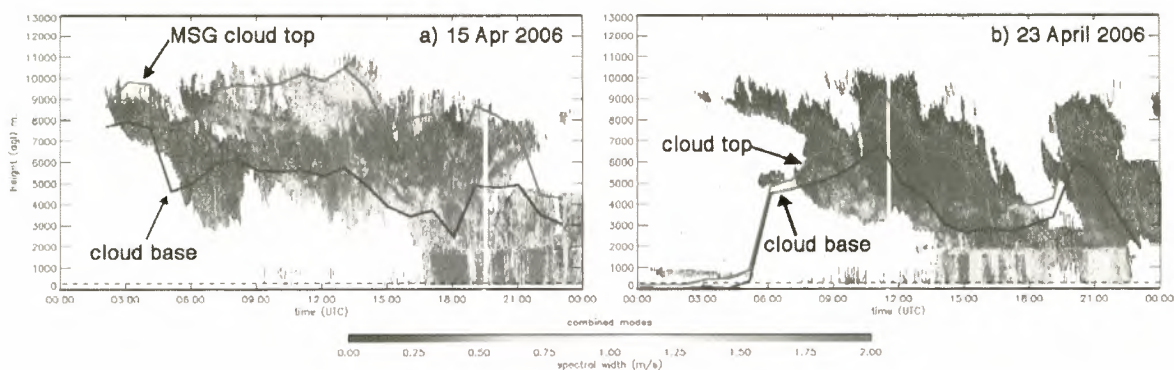


Figure 5. Cloud boundaries at Cabauw, Netherlands from cloud radar and Meteosat-8 using VISST and SIST.

Cloud boundaries from the VISST/SIST analyses track the cirrus boundaries determined from the Cabauw cloud radar during 15 April 2006 (Fig. 5a). Precipitation falls out below the cloud bases. The agreement is not as close during 23 April 2006 (Fig. 5b) when the thin low clouds are missed between 0100 and 0200 UTC and the cloud physical thickness is much greater than inferred by the satellite parameterization. Other images (not shown) have revealed the terminator problems noted earlier and some errors due to the temperature profiles.

Fig. 6 shows compares cloud-base heights for single-layer clouds derived from the Chilbolton lidar during daytime in February 2006. The satellite values, averages for a circle with a radius of 20 km centered on the site, are compared to 1-h lidar averages. The mean difference is only 0.1 km, while the RMS differences is 0.82. The comparisons for 3 months are summarized in Tab. 4. Overall, the satellite retrieval overestimates cloud-base height by 240 m with an RMS difference of 1 km. This result is fairly typical for single-layer clouds analyzed with the VISST.

The cloud LWP was derived from the surface microwave radiometer for the same months and compared to the VISST retrievals for single-layer clouds. The scatterplot and statistics are shown in Fig. 7.

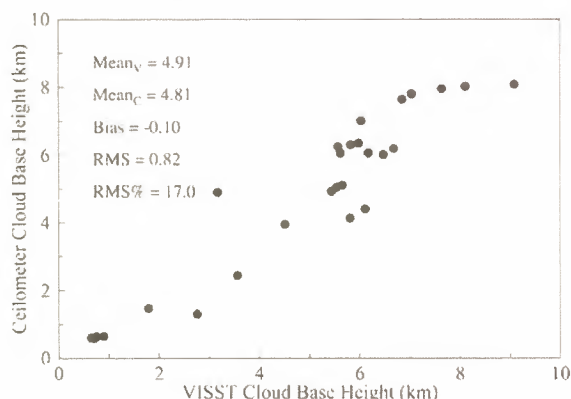


Figure 6. VISST-derived cloud base compared to Chilbolton lidar cloud base, February 2006.

Table 3. Lidar cloud base heights and differences with VISST retrievals over Chilbolton, UK, 2006.

Month	Sfc ht (km)	Diff (km)	RMS (km)	RMS (%)	N
Jan	1.34	-0.37	0.65	49	34
Feb	4.81	-0.10	0.82	17	28
Mar	4.94	-0.37	1.29	26	33
Total	3.61	-0.24	0.97	27	95

The average difference is less than 1%, however, the instant differences can be much larger as indicated by the scatter and the RMS error of 63%. This scatter is somewhat larger than seen in surface-satellite comparisons and could be due to greater variability in the surface data or using less than optimal averaging times and areas.

5. CONCLUDING REMARKS

The intercalibrations between SEVIRI and MODIS are encouraging. SEVIRI appears to have very stable solar channels with relatively good absolute calibrations. The procedures discussed here will be applied to future SEVIRI data to develop a long time record. Spectral differences will be taken into account to determine the actual corrections that should be applied to the data.

While the cloud properties often appear to be quite reasonable, much additional work is needed. Areas for improvement include the terminator, thin cirrus, and

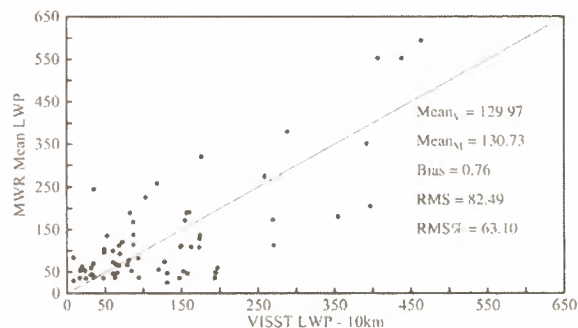


Figure 7. Same as Fig. 6, but for LWP, Jan-Mar 2006.

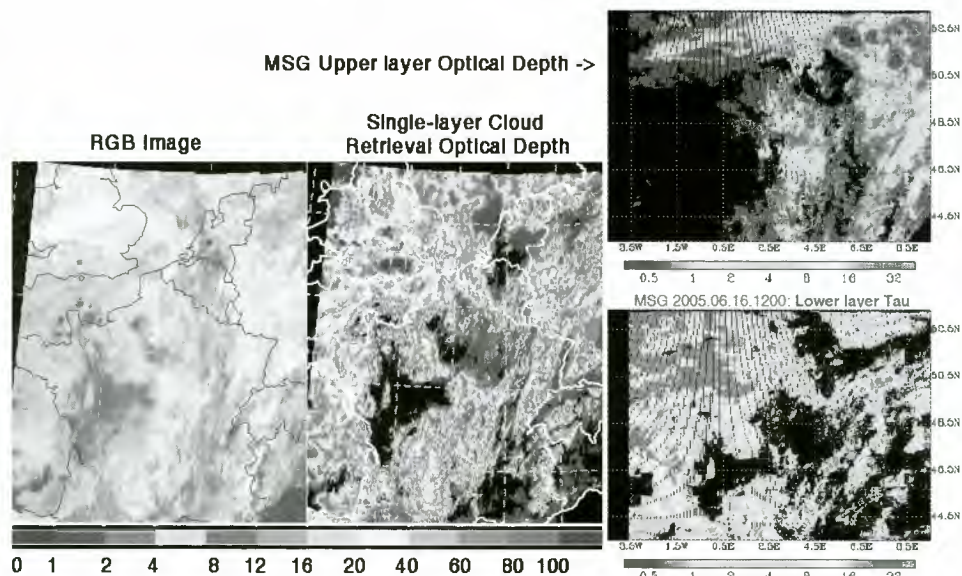


Figure 8. Example of multilayered cloud retrieval from SEVIRI data over Western Europe, 16 June 2006.

multilayered clouds. Efforts to address multilayered cloud retrievals have begun with the use of the method of [11] using the CO₂ channel. The example in Fig. 8 shows that the technique can separate the low and high clouds quite reasonably. This approach and others will be used to address the current shortcomings.

6. ACKNOWLEDGMENTS

This research was supported by the NASA Science Mission Radiation Sciences Branch and the NOAA GOES-R program. The MODIS data were obtained from the NASA Langley Research Center Atmospheric Sciences Data Center and the SEVIRI and GOES-12 data are from the University of Wisconsin-Madison Space Science and Engineering Center. Special thanks to the Radiocommunications Research Unit at the Rutherford Appleton Laboratory for data taken at Chilbolton, UK and to KNMI for the Cabauw radar data.

7. REFERENCES

1. Minnis P., et al. Real-time cloud, radiation, and aircraft icing parameters from GOES over the USA, *Proc. 13th AMS Conf. Satellite Oceanogr. and Meteorol.*, Norfolk, VA, Sept. 20-24, P7.1, 2004.
2. Minnis P., et al. Near real-time satellite cloud products for nowcasting applications. *Proc. WWRP Symp. Nowcasting & Very Short Range Forecasting*, Toulouse, FR, 5-9 Sept., 4.19, 2005.
3. Doelling D. R., P. Minnis, and L. Nguyen, Calibration comparisons between SEVIRI, MODIS, and GOES data. *Proc. MSG RAO Workshop*, Salzburg, Austria, 10-11 September, 149-154, 2004.
4. Minnis P., et al., Comparison of cloud properties from Meteosat-8 and surface observations. *Proc.*

MSG RAO Workshop, Salzburg, Austria, 10-11 September, 91-96, 2004.

5. Minnis P., et al. Rapid calibration of operational and research meteorological satellite imagers, Part II: Comparison of infrared channels. *J. Atmos. Oceanic Technol.*, **19**, 1250-1266, 2002.
6. Minnis P., et al. Rapid calibration of operational and research meteorological satellite imagers, Part I: Evaluation of research satellite visible channels as references. *J. Atmos. Oceanic Technol.*, **19**, 1233-1249, 2002.
7. Minnis P., et al. Cloud Optical Property Retrieval (Subsystem 4.3), "Clouds and the Earth's Radiant Energy System (CERES) Algorithm Theoretical Basis Document, Volume III: Cloud Optical Property Retrieval (Subsystem 4.3)", *NASA RP 1376 Vol. III*, edited by CERES Science Team, pp. 135-176, 1995.
8. Minnis, P., et al. Parameterization of reflectance and effective emittance for satellite remote sensing of cloud properties, *J. Atmos. Sci.*, **55**, 3313-3339, 1998.
9. Platnick S., et al. A solar reflectance method for retrieving cloud optical thickness and droplet size over snow and ice surfaces. *J. Geophys. Res.*, **106**, 15185-15199, 2001.
10. Arduini R. F., P. Minnis, and D. F. Young, Investigation of a visible reflectance parameterization for determining cloud properties in multilayered clouds, *Proc. 11th AMS Conf. Cloud Physics*, Ogden, UT, June 3-7, CD-ROM, P2.4, 2002.
11. Chang F.-L. and Z. Li, A new method for detection of cirrus overlapping water clouds and determination of their optical properties, *J. Atmos. Sci.*, **62**, 3993-4009, 2005.

USE OF SEVIRI DATA FOR AN OPERATIONAL CMSAF SURFACE RADIATION BUDGET PROCESSING AND ITS VALIDATION

R. Hollmann, R. W. Mueller

*Deutscher Wetterdienst, Kaiserleistrasse 29/35, 63067 Offenbach am Main, Germany,
Email: rainer.hollmann@dwd.de*

ABSTRACT

Since January 2005, the SAF on Climate Monitoring (CM-SAF, <http://www.cmsaf.dwd.de>) derives operationally consistent cloud and radiation parameters in high spatial resolution for an area that covers Europe and part of the North-Atlantic. The cloud and surface radiation products are based on data from the polar orbiting satellites NOAA (and in future METOP) for the northern latitudes. Starting in September 2005 data from MSG (METEOSAT-8) for mid latitudes are used as well for the calculation of the surface radiation budget, deriving short- and longwave fluxes, as well as for the calculation of its budgets.

To monitor and investigate the quality of the CM-SAF datasets high quality surface radiation budget measurements from different climates zones are used. The comparison shows a very good agreement on the monthly time scale with very little biases in general. However, regional differences especially for heterogeneous terrain are observable and will be discussed.

1. INTRODUCTION

The Satellite Application Facility on Climate Monitoring (CM-SAF) is aiming to generate and archive high quality data sets to improve the understanding of the climate system and its changes on a regional basis.

The target baseline area consists of Europe and the Mediterranean area, covering 30° N to 80° N and 60° W to 60° E. The deliverables of the Climate Monitoring SAF will be cloud information (e.g., cloud cover, cloud type), the radiation budget at the top of the atmosphere, the surface radiation budget, and a humidity composite product in high spatial resolution of 15 x 15 km² (45 x 45 km² for top of the atmosphere products) and with a time resolution ranging from daily to weekly and monthly means of the variables. In the area covered by METEOSAT 8 (MSG), a monthly mean of the diurnal cycle will be provided, taking benefit of the high temporal resolution of the satellite.

The project started 1999 with its development phase to select and implement the chosen algorithms. During the

initial operations phase the product development and processing will be extended in a step-by-step-approach: At first the operations will start with the NOAA-AVHRR processing for the baseline area, then, in September 2005, the processing with METEOSAT became operational, and finally, mid of 2006 there will be an area extension to the full disk of METEOSAT, covering the area from 60° S to 80° N and 60° W to 60° E.

An essential element of the CM-SAF will be the consistency between all derived products. The products will be on the same geographical grid and in a homogeneous data format. The product retrieval will benefit from the enhanced capabilities of the SEVIRI and GERB (Geostationary Earth Radiation Budget Instrument, [3]) instruments onboard MSG.

So far, the CM-SAF is producing an environmental climate data record of several essential climate variables to fulfil climate monitoring requirements there will be regularly reprocessing events to create homogeneous time-series of all products taking into account the instrument degradation and changes due to switches from one satellite to another satellite. The re-processing of data will be done with frozen and validated versions of the algorithms to avoid artefacts in the time-series due to algorithm changes.

This paper describes the work-package of the surface radiation budget retrieval based on first results and validations of MSG based results during the initial operations period. The next paragraph will give an overview of the algorithms and required data sets; the paragraph thereafter consists of the validation strategy, followed by first processing results and validation comparisons. The paper will end with a summary and an outline of future work.

2. ALGORITHMS AND DATASETS

The CM-SAF is using existent well validated algorithms to obtain the surface radiation budget. Four different components are derived independently, but consistently: surface incoming shortwave flux (SIS), surface downwelling longwave radiation (SDL), surface outgoing longwave radiation (SOL) and surface albedo (SAL). The net fluxes for longwave and shortwave as

well as the surface radiation budget are derived from the individual components.

After the reception, navigation and calibration of the satellite data the cloud module is applied. The cloud module for MSG data has been developed by the SAF on Numerical Weather Prediction and was implemented in the operational CM-SAF environment at DWD.

For the longwave spectral domain, the Gupta algorithm ([1], [2]) was adapted. This algorithm needs the vertical structure of the atmosphere, i.e., temperature and humidity profile in 3 layers and cloud information as input information. These layers have originally been derived from the TOVS vertical humidity and temperature profiles [1], later adapted to the ISCCP height profiles. In this framework, vertical profiles of analysis fields from numerical weather prediction are used as input data. The analysis data in the operational processing are from the DWD weather forecasting model GME with a spatial resolution of $0.5^\circ \times 0.5^\circ$ latitudinal longitudinal. From the results of the cloud module, the derived cloud flag and the cloud top height is used. From these, the main determining water vapour column content below the cloud is estimated by means of a pre-set cloud thickness of 50 hPa. This value has been taken from the climatology of [11] and is subject to change with a newer climatology.

To obtain SOL, the Stefan-Boltzmann equation with a surface dependent emissivity is used. The surface temperature is taken from NWP analysis data, whereas the surface emissivity maps have been prepared by [12]. For the calculation of SIS, an algorithm similar to the one developed by Pinker (e.g. [10]) is used. The basic idea of the algorithm is that the relationship between the broadband (0.2-4.0 μm) atmospheric transmittance and the reflectance at the top of the atmosphere can be described by state of the art radiative transfer models. With a radiative transfer model (e.g., LibRadtran [7]), the broadband atmospheric transmittance is calculated once in relationship to the broadband top of atmosphere albedo for a variety of atmospheric and surface states. The actual computation of the surface irradiance includes two steps. Firstly, the broadband top of the atmosphere albedo and the surface broadband albedo is determined from the satellite measurement. For this, the GERB [3] measurements with a resolution enhancement to full SEVIRI resolution at the top of the atmosphere is used. Afterwards the atmospheric transmittance is determined from the top of the atmosphere albedo together with information on the atmospheric and surface state from the pre-computed tables. To make this interpolation more time efficient and also to take advantage of the inherent symmetries, a modified Lambert-Beer (MLB) approach after [7] is used. Therefore it is only necessary to compute the SIS at two

different sun zenith angles of 0° and 60° . For these angles a MLB relation is fitted and their values are stored and used in the interpolation to the measured sun zenith angle.

Critical parts of the algorithm are the aerosol climatology and the surface albedo background data. For the first one, model computed single scattering albedo, asymmetry factor and aerosol optical thickness are used. Both are taken from OPAC/GADS climatology ([4], [5]) or alternatively from global aerosol model climatologies (e.g. Stefan Kinne (MPI-Hamburg), 2004, pers. communications).

For the surface albedo background the independently derived weekly mean of the surface albedo calculated with the help of an algorithm from [6] using the radiance measured by the visible channels of SEVIRI is used.

The broadband top of atmosphere albedo for the area covered by the MSG satellite, the surface albedo and the cloud properties are derived by other groups within the CM-SAF. All other input data are either from climatological data sets (aerosol, ozone) or numerical weather prediction model-data (water vapour).

2.1. From instantaneous to daily and monthly means

For each satellite measurement from SEVIRI (currently one slot every hour is used) all the above described instantaneous products are derived. To come to a daily mean for the longwave components, all instantaneous satellite derived surface fluxes are averaged over 24 hours. For the SIS, a slightly different approach is used. A clear sky daily average of SIS (24 hour mean value) is calculated first. In the next processing step, this is weighed by the ratio of all instantaneous measurements with their respective (maximum) clear sky flux from this day. This allows calculating a more realistic daily mean of SIS than just taking into account the measurements from the overpasses itself.

For all daily means the necessary numbers of overpasses to calculate a daily mean is set to three. The monthly mean value is calculated based on the availability of at least 20 daily means, otherwise it is set to undefined.

3. VALIDATION OF RADIATION PRODUCTS

The surface radiation fluxes will be validated with all available surface measurements (e.g., networks of National Meteorological and Hydrological Services, Baseline Surface Radiation Network) to ensure a good quality of the data. It is expected to establish an automatic quality assurance and checking tool for all surface radiation products.

An operational network is the Baseline Surface Radiation Network (BSRN, [9]), initiated by the World Climate Research Program (WCRP). BSRN measures, quality controls and archives surface radiation measurements from dedicated stations around the world. In 2003, 35 stations were fully or partially operational.

Some of the BSRN stations and further operational surface sites have been selected as target stations (Tab. 1) to validate our results.

Station	Latitude	Longitude	Measured component
Carpentras	44.05° N	5.03° E	SIS, SDL
Cabauw	51.97° N	4.93° E	SIS, SDL, SOL
Lindenberg	52.22° N	14.12° E	SIS, SDL, SOL, SAL
Payerne	46.81° N	6.94° E	SIS, SDL, SOL, SAL

Table 1. Selected stations for validation of Surface Radiation products

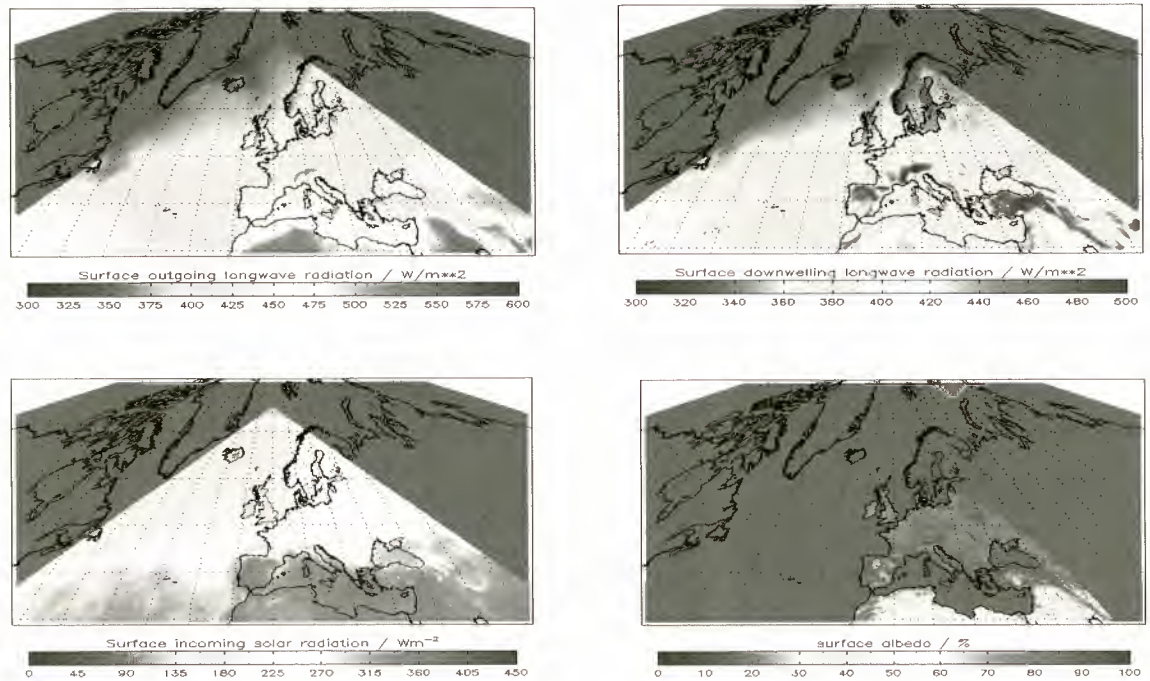


Figure 1. Monthly Means in W/m^2 of surface radiation products for July 2005: Outgoing longwave radiation (top left), Downwelling Longwave Radiation (top right), Surface incoming solar radiation (bottom left) and surface albedo (bottom right)

4. RESULTS

4.1. Validation of monthly means

The operational processing of MSG data has been started in September 2005 and is running continuously. As an example of products, Fig. 1 shows the monthly means of the surface radiation budget components for July 2005. At the moment no cut-off-angle for the viewing geometry of MSG is introduced except for the surface albedo which is not calculated for viewing zenith and sun zenith angles greater than 70° , therefore Fig. 1 gives the full coverage of MSG-satellite in the chosen CM-SAF $15 \times 15 \text{ km}^2$ sinusoidal spatial resolution.

4.2. Validation of instantaneous data

Routine validation of the results has been started in parallel with the processing. A target accuracy of 10 W/m^2 on monthly mean basis has been defined within the scope of CM-SAF project. The selection of the definition was based on expected accuracies needed for the regional climate analysis and regional climate monitoring. In this context, the target accuracy is an important benchmark for the usability of the data products.

The validation is done as follows: For each instantaneous overpass an area of 3 by 5 pixels corresponding to about $15 \times 15 \text{ km}^2$ symmetrically around the surface site has been extracted and their statistics were computed. From the surface

measurements point of view some data are in hourly format, some have a higher temporal resolution, thus the decision was taken to average all surface data within one hour and compare this to the spatial mean derived as described above. All measurements were taken and the monthly mean has been calculated and compared. The results of this for MSG-based results are tabled in Tab. 2 for all components. It clearly demonstrates that most products are within the target accuracy. Nevertheless, for the longwave downwelling component as slightly higher mean difference is observed due to heterogeneity problems of the Payerne station.

	BIAS in %	BIAS in W/m ²	Target acc. W/m ²
SOL	2.4	9.3	10
SDL	4.5	10.9	10
SIS	6.5	4.0	10
SNL	-	7.2	15

Table 2. Results of comparisons of MSG products for 4 stations and 11 processed months

The water vapour amount as well as the surface temperature is provided by NWP analysis. This could be an error source for specific regions as in heterogeneous terrain the NWP model does not give a good diurnal variation of the surface temperature. On the other hand the measurement of the longwave radiation components does reflect this. However, the reasons for the biases have to be analysed in more detail, which is in progress.

Also a validation based on daily averages is done. A result of this for the solar incoming radiation is shown in Fig. 2. Here all daily mean data since March 2004, where the preoperational processing of NOAA-AVHRR had started are shown until May 2006. This gives also a good estimate of the achieved accuracy of our products. The correlation is very high and the general biases are small for this product.

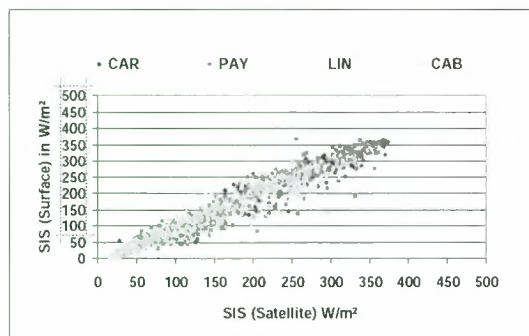


Figure 2. Scatter diagram for all daily means of solar incoming radiation since March 2004 with different colors for different stations (blue: Carpentras, yellow: Lindenberg, light blue: Cabauw, pink: Payerne). Both, NOAA AVHRR and MSG based results are shown

The validation exercises of the processing delivers clear evidence that the target accuracy can be achieved. It is important to note that the derived biases can not be transformed one-to-one to monthly or daily means, because of the averaging process. In this context the percentage biases are the relevant quantities. They are comparatively small demonstrating the usability of the SIS routines for climate monitoring purposes.

5. FUTURE WORK

Since the beginning of the processing of MSG based products, it is possible to inter-compare products based on two different satellites on multiple time and spatial scales. As both product sets have been produced with the same algorithms to derive the surface radiation it is possible to investigate the issues of time-sampling (up to quarter-hourly MSG-measurement versus the 2-3 measurements a day from polar orbiting satellite), spatial sampling (different spatial resolution of both satellites), cloud masking (different algorithms based on the capabilities and advantages of each satellite) and the top of atmosphere albedo.

For the MSG-based product set the CM-SAF uses the resolution enhanced GERB based broadband measurements, whereas for the NOAA overpasses a narrow-to-broadband conversion has to be used followed by the angular direction modelling to come from the radiance to the flux.

Both data sets together offer the unique opportunity to inter-compare both and estimate the errors in the processing. This is also the first step toward a homogenized top of the atmosphere flux data set for the CM-SAF area which then could be used in the development and production of a climate data record. This work is ongoing and first results of a few processed days suggest that the method is valuable and working and the mean difference seems to be small, nevertheless also indicating some regional features.

From the surface radiation group of the CM-SAF already some inter-comparison with other international products like the GEWEX-SRB or ISCCP-FD data sets have been done. This work will also be continued once more months of these international data sets become available, as at the moment only a few month of overlap in 2004 could be used for this work. These few months yield to very similar results with small overall biases less than 5 W/m² but with clear regional (ocean/land) contrasts which will be investigated in future.

Together with the extension to the full disc processing the CM-SAF has decided to support the AMMA (African Monsoon Multidisciplinary Analyses) in 2006. For this the targeted area is cut off the product and will be available as autonomous subset.

6. SUMMARY

In January 2005, the CM-SAF started the operational processing of NOAA-AVHRR data to derive the products for the target area in Europe. Later on, in September 2005, we have started to process and deliver MSG-based products on a routine basis. This paper has described the algorithms which are used to derive surface radiation budget products on high spatial scale of 15 x 15 km². First results of the ongoing validation for MSG-based products with selected sites have been shown.

For all components of the surface radiation budget it can be concluded that the average mean biases are small and they will be within the targeted accuracy of 10 W/m² on monthly mean time scales. Higher biases for some stations need further investigation. The validation demonstrates the potential of the radiation algorithms to retrieve radiation products usable for climate monitoring and analysis of regional climate change.

6. ACKNOWLEDGEMENTS

The surface radiation data have been kindly provided in timely manner from the Swiss Meteorological Service (MeteoSwiss), Alfred Wegener Institute (Germany), Deutscher Wetterdienst, KNMI, Meteo France and University of Valencia. We thank Arne Kylling (NILU) and Bernhard Mayer (DLR) for providing the LibRadtran RTM package. LibRadtran is available from <http://www.libradtran.org>.

7. REFERENCES

1. Gupta S.K. A parameterization for longwave surface radiation from sun-synchronous satellite data. *J. Climate*, 2, 305-320, 1989.
2. Gupta, S.K., Darnell, W.L., Wilber, A.C. A parameterization for longwave surface radiation from satellite data: recent improvements. *J. of Appl. Meteorol.* 31, 1361-1367, 1992.
3. Harries, J.E., and the GERB Science Team, The Geostationary Earth Radiation Budget Project, *Bull. Amer. Meteorol. Soc.*, 86, 945-960, 2005

4. Hess, M., Koepke, P., Schult, I. Optical properties of aerosols and clouds: the software package OPAC. *Bull. Amer. Meteor. Soc.* 79, 831-844, 1998.
5. Koepke, P., Hess, M., Schult, I., Shettle, E. Global aerosol data set. *Technical Report MPI Meteorologie, Hamburg*, 243, 1997.
6. Laine, V., Venäläinen, A., Heikinheimo, M.; Hyvaerinen, O. Estimation of surface solar global radiation from NOAA AVHRR data in high latitudes. *J. of appl Meteorol.* 38, 1706-1719, 1999.
7. Mayer, B., Kylling, A. Technical note: The libRadtran software package for radiative transfer calculations - description and examples of use, *Atmos. Chem. Phys.*, 5, 1855-1877, 2005.
8. Mueller, R., Dagestad, K.F., Ineichen, P., Schroedter-Homscheidt, M., Cros, S., Dumortier, D., Kuhlemann, R., Olseth, J.A., Piernavieja, G., Reise, C., Wald, L., Heinemann, D. Rethinking satellite-based solar irradiance modelling: The SOLIS clear sky module. *Remote Sensing of Environment* 91, 160-174, 2004.
9. Ohmura A., Dutton, E.G.; Forgan, B. et al. Baseline surface radiation network (BSRN/WCRP): new precision radiometry for climate research. *Bull. Amer. Meteor. Soc.* 79, 2115-2136, 1998.
10. Pinker, R.T., Laszlo, I. Modelling surface solar irradiance for satellite applications on a global scale. *J. Appl. Meteor.* 31, 194-211, 1992.
11. Telegadas K., London J. A. physical model of the northern hemisphere troposphere for winter and summer. *Scientific Rep 1; Dept of Meteorology and Oceanography*, New York University, 1954.
12. Wilber, A.C., Kratz, D.P., Gupta, S.K. Surface emissivity maps for use in satellite retrievals of longwave radiation. *NASA Technical Paper, NASA/TP-1999-209362*, 1999.

COMPARISON OF SEVIRI CLOUD PRODUCT WITH BOTH THE POLDER AND THE GLAS SPACE LIDAR ONE

G. Sèze⁽¹⁾, F. Parol⁽²⁾, J. Pelon⁽³⁾, C. Vanbauce⁽²⁾, H. Legleau⁽⁴⁾, M. Derrien⁽⁴⁾, M. Lalande⁽¹⁾, J. Riedi⁽²⁾,
and J.C. Buriez⁽²⁾

(1) *Laboratoire de Météorologie Dynamique, Université Pierre et Marie Curie, 75252 Paris Cedex 05, France.
Email: seze@lmd.jussieu.fr*

(2) *Laboratoire d'Optique Atmosphérique, Université des Sciences et Technologies de Lille, 59655 Villeneuve d'Ascq
Cedex, France*

(3) *Service d'Aéronomie, Université Pierre et Marie Curie, 75252 Paris Cedex 05, France*

(4) *Centre de Météorologie Spatiale Météo-France, BP 50547, 22307 Lannion Cedex, France.*

ABSTRACT/RESUME

Cloud amount and cloud properties are key parameters of the climate system. They need to be adequately monitored. A promising way of improving cloud property retrieval is the combined use of new ensemble of data based on different measurement techniques. In the present study we focus on the comparison of cloud pressure distributions derived from four types of measurements: (1) the SEVIRI passive infrared measurements provided by the SAFNWC (Satellite Application Facility in support to NoWCasting), (2) spectral polarization measurements, and (3) absorption measurements in the oxygene A-band from the passive radiometer POLDER2 (POLarization and Directionality of the Earth's Reflectances) on board the ADEOS2 platform and (4) measurements from the space lidar GLAS (Geoscience Laser Altimeter System) on board the ICESAT platform. The October 2003 period is selected as both data from POLDER2 and GLAS are available at this period. The SAFNWC SEVIRI cloud top pressure, the POLDER Rayleigh cloud top pressure and the POLDER Oxygene cloud pressure distributions show the same global features and differences than those observed in a first SEVIRI/POLDER comparison for several days in June 2003. However, compared to the June 2003 results, for the October 2003 period, low cloud top pressure in the new version 1.2 of the SAFNWC SEVIRI products are closer to the POLDER Oxygene pressure. For high thick clouds, the SEVIRI and Rayleigh pressure are close. The more striking results of the preliminary comparison of the SEVIRI and space lidar GLAS cloud top pressure is that the cloud pressure distribution shapes are very similar over ocean as well as over land. As part of the A-train satellite constellation, PARASOL/POLDER has been launched in December 2004, the CALIPSO lidar and the CLOUDSAT radar have joined PARASOL and the A-Train in May 2006. Study of the relation between cloud properties observed from SEVIRI, POLDER and active measurements will be continued in this frame.

1. INTRODUCTION

Cloud amount and cloud properties are key parameters of the climate system. They need to be adequately monitored. Among the new generation of Earth-orbiting instruments designed for Earth's observation, the SEVIRI radiometer onboard Meteosat-8 provides high quality data with 3 km spatial resolution, 15 mn temporal sampling and 12 narrow spectral bands; the

POLDER radiometer launched on ADEOS-2 in December 2002 presents the particularity of having multispectral (8 solar spectral bands), multi-polarization and multi-directional (up to 14 different viewing angles) capabilities [1]. An overview of algorithms and products of the "Earth Radiation Budget, water vapor and clouds" line (hereafter "ERB & clouds") applied to POLDER data is presented in [2], [3] and [4]. POLDER2 "ERB & clouds" products are available from April 2003 to October 2003, the end of service of the ADEOS-2 platform. Six days in June 2003 were selected for comparison to preliminary SEVIRI output data of the SAFNWC (Satellite Application Facility in support to NoW Casting) cloud algorithm [5],[6]. On the other hand, a cloud classification based on a dynamical clustering method [7] was applied as an alternative method to SEVIRI radiance data provided by the Centre de Météorologie Spatiale (CMS) in Lannion (France). POLDER and SEVIRI cloud amount were compared and SEVIRI cloud type and cloud top pressure were checked against cloud pressure and thermodynamic phase retrieved from POLDER. Results of these comparisons were presented in [8].

In the present study we focus on the validity of cloud pressures derived from SEVIRI by the SAFNWC team. The October 2003 period is selected as data from the GLAS space lidar are also available at this period [9],[10]. Cloud top height and cloud layer structures provided by GLAS are used to help understanding the differences observed between the SEVIRI cloud pressures and the POLDER ones [8]. Section 2 presents a short description of the cloud parameters (pressure and cloud type) compared in this study. In section 3, SEVIRI cloud top pressure are checked against cloud pressure and thermodynamic phase retrieved from POLDER; quantitative comparison with results discussed in [8] but for June 2003 is presented. GLAS measurements, available for October 2003 but not coincident with POLDER overpass times, are compared to the SEVIRI cloud top pressure and cloud type in section 4. Conclusions and perspectives are given in section 5.

2. BRIEF DESCRIPTION OF THE CLOUD PROPERTY RETRIEVALS.

2.1 The SAFNWC SEVIRI cloud type and cloud top pressure retrievals

Presently, the SAFNWC provides cloud mask, cloud type and cloud top temperature/pressure/height maps, by using the multi-spectral capabilities of the SEVIRI radiometer [11], [6]. In the future, cloud top phase maps will be added to the cloud products. The first stage in the SAFNWC cloud product derivation is the sorting between cloud free and cloud contaminated pixels. It is based on a serie of sequential threshold tests. The process is stopped if one test is successful. The test that allows the cloud detection is stored and a quality flag is computed.

The main interest of the cloud type product developed within the SAFNWC framework is to provide a detailed cloud analysis to support nowcasting applications. Using spectral and textural features, cloudy pixels are classified first in two sets: (1) fractionnal and high semitransparent cloud, (2) low, medium and high thick. The separation between fractionnal, high semitransparent cloud and high semitransparent cloud over low or medium cloud is performed using spectral features. For thick cloud, the separation in very low cloud, low cloud, medium cloud, high cloud and very high cloud is performed using Numerical Weather Prediction (NWP) forecast temperature.

The cloud top pressure is retrieved from the $10.8 \mu\text{m}$ brightness temperature for low, medium and thick clouds. For high thin clouds, a correction for semi-transparency is applied using two infrared channels, a window ($10.8 \mu\text{m}$) channel and a sounding ($13.4 \mu\text{m}$, $7.3 \mu\text{m}$ or $6.2 \mu\text{m}$) one. For fractional clouds, the top pressure is not estimated.

The first set of data (June 2003) provided by the CMS and used in the first comparison of SEVIRI and POLDER [8] was from the product version 1.0 [11]. The product version of the data set coincident used in this study is 1.2 [12]. The major change between the two versions relates the estimation of the low cloud pressure in case of thermal inversion in the NWP forecast air temperature vertical profile at low level. This change tends to place the cloud top level under the low level inversion, e.g. at a lower pressure level. Results of a comparison of the cloud top pressure product version 1.2 with radio-sounding data and with ground based radar and lidar data are given in [13].

2.2 The POLDER cloud property retrievals

The POLDER cloud amount is determined by applying first a cloud detection algorithm to each full-resolution pixel ($6.2 \text{ km} \times 6.2 \text{ km}$) and for every viewing direction. Then the cloud cover is computed at the super-pixel scale (3×3 pixels) and a quality index is defined from concurrent responses to the different tests. See [2],[3] for a complete description of this algorithm.

For cloudy super-pixels, an algorithm for remotely determining the cloud-top thermodynamic phase is applied. The algorithm utilizes near-infrared polarized reflectance over a large range of scattering angles in order to discriminate between ice and liquid water

phases [4],[14]. Indeed, theoretical as well as experimental studies have shown that polarized signatures of water droplets and ice particles are quite different. The last version of the algorithm has been applied to the data used in this study. Compared to the version of the algorithm used for the June 2003 data set [8], this improved version uses more strict conditions in particular on the range of scattering angle required to estimate the phase. If this conditions are not met, a cloud phase is attributed from a rough estimation of the pressure. A quality index is attached to the cloud phase product.

For cloudy super pixels with optical thickness above 3, two different methods were developed to retrieve cloud pressure. The first one is derived from absorption measurements in the oxygen A-band and the second one is derived from spectral polarization measurements. The derivation of the "Oxygen pressure" P_{oxy} is based on a differential absorption technique using the radiances measured in the POLDER narrowband and wideband channels centred on the oxygen A-band. [15] have shown that P_{oxy} is found to be close to the mean pressure of clouds when compared to ARM/MMCR cloud boundary pressures. Another retrieved cloud pressure is the so-called "Rayleigh cloud pressure", P_{Ray} , derived from polarization measurements at 443 nm [3]. At this wavelength, the polarized reflectance is mainly related to the atmospheric molecular optical thickness above the observed cloud, at least for scattering angles ranging from 80° to 120° and outside the sunglint direction. That pressure is thus expected to be close to the cloud top pressure.

2.3. The GLAS cloud layer retrieval

The spaceborne lidar measurements are made under the track of the satellite using two channels, one operating at 532 nm and the other at 1064 nm . The swath is very narrow. The laser pulse rate of 40 Hz , yields vertical profiles at approximately 172 m spacing along a given orbit track with a vertical resolution of 76.8 m . A list of the GLAS data products is given in [10], [16]. The cloud layer boundaries (GLA09) are determined from the calibrated, attenuated backscatter cross sections (GLA07). For the cloud to be detected, the attenuated backscatter cross section must be larger than a given threshold on the signal-to-noise ratio reachable for a given horizontal-vertical resolution. During the October 2003 period, the 532 nm channel was more sensitive and has been used to determine cloud layers.

Cloud top heights from 532 nm are determined at four different sampling rates (horizontal resolution) in the following order: 4 s , 1 s , 0.2 s , and 0.25 s [16]. If a cloud layer height is found at 4 s time interval, then a search is performed at 1 s and so on down to the smallest time interval. In the present study, results at 1 s time interval (about 7 km horizontal resolution) have been used.

Another useful parameter given in the GLA09 product is the presence or absence of a surface echo. This

parameter allows to separate scenes completely covered by opaque clouds from scenes covered by thin or broken cloud layers. In the GLA09 product, not only the heights but also the pressure levels at top and base of detected cloud layers are given.

2.4 Selected data set

POLDER2 “ERB & Clouds” products are available for the April to October 2003 period. The initial on-orbit full operation of the GLAS instrument began on September 28, 2003 until November 18, 2003. For 86 GLAS orbits and 65 POLDER orbits distributed over 17 days in September–October 2003, (although the SEVIRI calibration was not final) the SAFNWC provided the SEVIRI radiance fields and its cloud products coincident in time with the GLAS or the POLDER overpasses. For GLAS, the time of the descending/ascending node is 7:30/19:30 and for POLDER, the time of the descending node is 10:30. Thanks to the 15' repeat cycle of Meteosat-8/SEVIRI, the time-lag is at the most of 7.5' between the SEVIRI and GLAS or the SEVIRI and POLDER coincident data sets.

POLDER “ERB & Clouds” products (final product at 18.5 km x 18.5 km resolution) and the 1s. GLAS cloud layer product (7.5km horizontal resolution) have been projected on the SEVIRI grid (3.3 km x 3.3 km at sub-satellite point).

3. POLDER AND SEVIRI CLOUD PRESSURES IN OCTOBER 2003

Figure 1 displays the SAFNWC cloud top pressure (Fig. 1a), the POLDER Rayleigh cloud top pressure (Fig. 1b), the POLDER Oxygen cloud pressure (Fig. 1c) and the POLDER cloud phase (Fig. 1d) retrieved for the October 20, 2003. The three cloud pressure maps, are in agreement with what has been presented in our previous paper on the comparison of SEVIRI and POLDER cloud properties [8]. The main characteristics of the two cloud top pressure maps (SEVIRI and POLDER Rayleigh pressure) are coherent with that found in the analysis of the SEVIRI cloud type maps (not shown) and POLDER cloud phase maps. As expected, the POLDER oxygen cloud pressure is on average higher than the cloud top pressures (see for example the stratocumulus cloud deck in the south part of the Atlantic ocean). If the main characteristics of the two cloud top pressure maps are coherent, some differences are however observed between them (see fig 1.a and fig 1.b). Pressure of low clouds is higher in the SEVIRI results than in the Rayleigh map. Some very low pressure values (high clouds) appear in the Rayleigh map.

The distributions and average values of the 3 cloud top pressures over ocean and over land are reported in Figure 2 and table 1. The shapes of these distributions obtained for 15 days in October 2003 are similar to those obtained for the 6 days of June 2003 already discussed in [8]. However, over ocean, the high pressure

peak of the SEVIRI distribution is shifted towards higher pressure value while the high pressure peak of the Rayleigh distribution is shifted towards lower pressure value. Both over ocean and over land, very low Rayleigh pressure values are observed in October; this is not the case in the SEVIRI cloud pressure distribution.

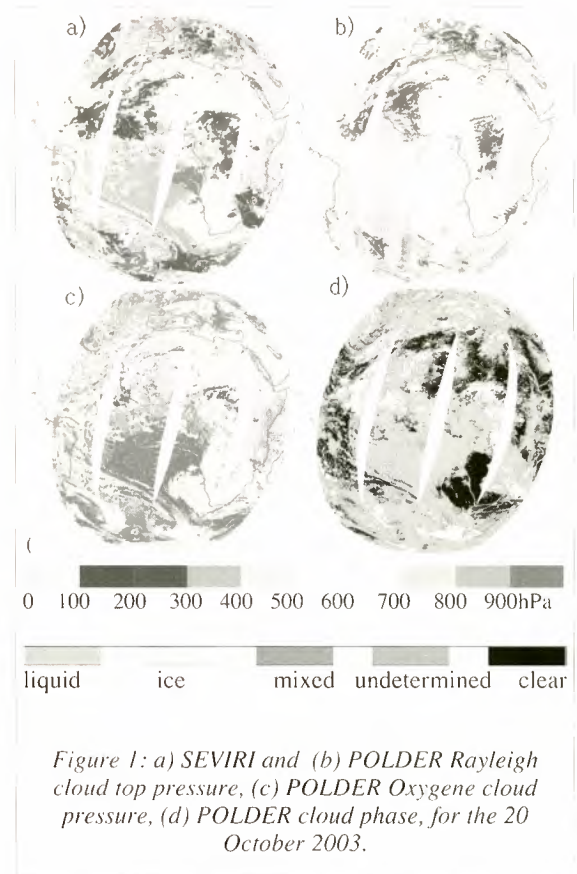


Figure 1: a) SEVIRI and (b) POLDER Rayleigh cloud top pressure, (c) POLDER Oxygen cloud pressure, (d) POLDER cloud phase, for the 20 October 2003.

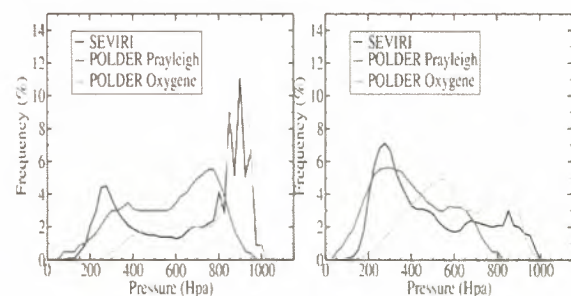


Figure 2: Cloud pressure distributions over ocean (left) and over land (right) for 15 days of October, 2003.

For the 3 cloud pressure distributions and for June and October over ocean and land, the average pressure as a function of cloud phase is given in table 2. When comparing June and October 2003, SEVIRI and Rayleigh pressure mean values for liquid clouds vary in an opposite manner. This is observed over ocean (Table 2) as well as over land (results not shown). On the average for ice clouds the SEVIRI pressure values remain the lowest.

The changes observed in the cloud pressure

distributions between the June and October data set are coherent with the changes performed in the SAFNWC algorithm for the estimation of low cloud pressure (see section 2.1 and 2.2).

Table1: SAFNWC, Rayleigh and Oxygene mean pressures in hPa for the October and June 2003 cases.

	Ocean			Land		
	SEV	Ray.	Oxy.	SEV	Ray.	Oxy.
Oct.	638	572	775	492	432	651
June	594	616	751	502	500	671

Table2: Average pressures in hPa for the October and June cases over ocean and land in function of POLDER cloud phase.

	Liquid			Ice		
	SEV.	Ray.	Oxy.	SEV.	Ray.	Oxy.
Oct.	685	593	809	331	357	525
June	635	640	786	350	403	538

4. GLAS AND SEVIRI

An example of simultaneous SEVIRI pressure fields and GLAS cloud layer profile is given in figure 3 for two cases on October 10, 2003. A high cloud system over west Africa is observed in the first case and a thick low cloud deck in the subsidence region offshore Namibia in the second profile.

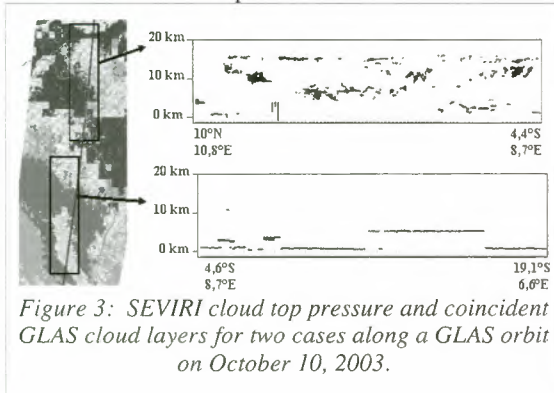


Figure 3: SEVIRI cloud top pressure and coincident GLAS cloud layers for two cases along a GLAS orbit on October 10, 2003.

4.1 GLAS and SEVIRI cloud types

The classification of GLAS cloudy column in cloud types is performed according to three criteria. The first criterion is the pressure of the highest layer. The atmospheric column is divided in ten levels of pressure. The second criterion discriminates thin/broken cloud scene from thick cloud scene using the surface echo flag. The third criterion classifies the cloudy columns in single layer and multi-layer cloud scene. The single layer case corresponds to cases for which clouds are gathered in only one of the ten pressure levels. The

multi-layer case corresponds to the other cases. In this classification, high clouds correspond to cloudy column with a cloud top pressure below 400hPa, medium correspond to cloudy column with a cloud top level between 400hPa and 700hPa and low clouds correspond to cloudy column with a cloud top pressure larger than 700hPa.

In the SAFNWC SEVIRI cloud type classification 10 cloud classes are defined: partial, very low, low, middle, thick high, very thick high, very thin cirrus, thin cirrus, cirrus, cirrus over.

In a first step of the analysis, SEVIRI cloud types as well as GLAS ones are merged into 4 main types, clear and low, middle, high clouds. It is found that over ocean/land for the 86 GLAS studied orbits distributed over 17 days in September-October 2003, 74%/72% of pixels fall in the same class. The pixels corresponding to the SAFNWC partial cloud class have been excluded of the comparison (16%/4% of the total).

The distribution of the 4 GLAS main cloud types has been studied for each SEVIRI cloud class. To this respect, the 10 SEVIRI cloud types have been gathered in 6 cloud types, clear, partial cloud cover, low, middle and high cloud, cirrus over another layer (called "cirrus over"). Results are reported in Figure 4. Over ocean as well as over land, for the SEVIRI high cloud type, GLAS has effectively detected a high cloud layer in more than 85% of the cases; for the SEVIRI "cirrus over" class, this percentage reaches 70%.

If the SEVIRI low cloud type is consistent with the GLAS classification in 75% of the cases over ocean, over land the percentage drops to only 45% of the cases. Both over ocean and over land for the SEVIRI middle cloud class the percentage of agreement with GLAS classification is less than 60%. Pixels classified in the SEVIRI partial cloud class do not belong to a well defined GLAS cloud class.

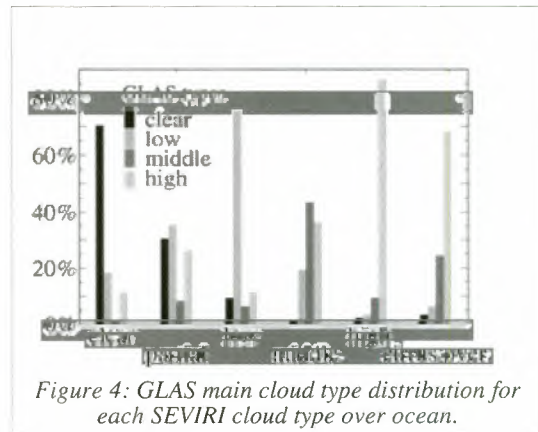


Figure 4: GLAS main cloud type distribution for each SEVIRI cloud type over ocean.

4.2 GLAS and SEVIRI cloud pressure

In this section we define the parameter "GLAS cloud pressure" as the top pressure of the highest cloud layer detected by GLAS.

For the 86 GLAS orbits distributed over 17 days in September and October 2003, the global shapes of the SEVIRI and GLAS cloud pressure distributions are "remarkably" similar (see Fig. 5). Over ocean the

distributions present two peaks with a strong decrease between 400 and 700hPa. Over land there is only one peak at low pressure values and a relatively uniform distribution between 500 and 850hPa over land. However, a bias towards higher pressure values appears in the SEVIRI curves compared to the GLAS ones.

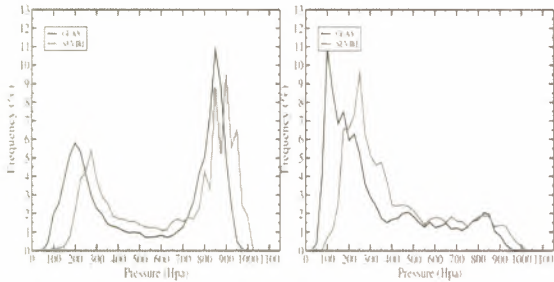


Figure 5: GLAS and SEVIRI cloud pressure distributions over ocean (left) and over land (right)

The bidimensional distribution of the two cloud pressures (not shown) indicates a good correlation between the two set of pressures and confirms the bias observed in figure 5 especially for high clouds. The mean difference between the SEVIRI and GLAS pressures is 67hPa and the RMS is 180hPa.

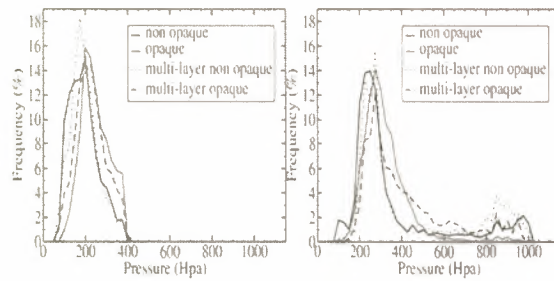


Figure 6: GLAS (left) and SEVIRI (right) cloud top distributions for the four GLAS high cloud classes over ocean.

Figure 6 shows the GLAS (left) and SEVIRI (right) cloud top distributions for the four GLAS high cloud types over ocean. For GLAS the non opaque curve presents the largest percentage of very low pressure. For the opaque case, we find more pressure values close to the 400hPa boundary (defined as the boundary for the high cloud type in the GLAS algorithm).

This is also the case for the SEVIRI pressure (right) for the GLAS opaque cloud classes. A non negligible percentage of cloud top pressure above 400hPa is found in the SEVIRI distributions, excepted for the opaque single layer curve.

It is for middle level clouds that the largest differences are found between the GLAS and SEVIRI cloud pressure distributions (not shown). For GLAS non opaque middle cloud type the SEVIRI pressures values are almost equitably distributed between 200 and 1000hPa. "Surprisingly", for opaque clouds, there are SEVIRI cloud top pressures below 400hPa.

A sub-classification of the GLAS low cloud depending on the cloud top pressure of the highest layer is performed. Over land and for the opaque GLAS single-

layered low cloud class, the SEVIRI cloud pressures are split in three sub-classes (cloud top pressure (1) between 700 and 850hPa, (2) between 850 and 925hPa and (3) above 925hPa). The results are shown in figure 7.

The three distributions obtained for SEVIRI move in agreement with the increase in the values of cloud pressures retained for GLAS. The percentage of pressure values below 600hPa is very small. Over ocean (not shown) distribution shapes are more peaked and very low pressure values are almost absent.

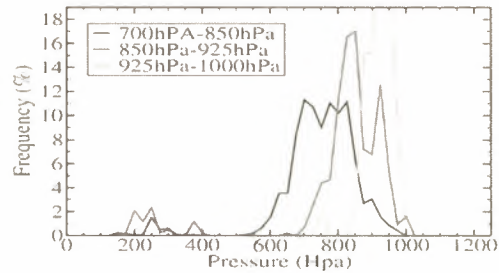


Figure 7: SEVIRI cloud pressure distribution for GLAS opaque single layer low clouds over land.

Table3 gives the mean differences between the SEVIRI and GLAS cloud top pressure and the RMS of the differences for the 3 main cloud types: high, middle and low clouds. Table 4 is equivalent to table 3 but for the single-layered opaque cloud case. A strong decrease in the mean and RMS differences is observed for high cloud when only the single-layered opaque cases are taken into account.

Table3: SEVIRI minus GLAS cloud top differences for GLAS high, middle and low clouds.

	Ocean		Land	
	Mean	Rms	Mean	Rms
High	148hPa	249hPa	104hPa	169hPa
Middle	42hPa	161hPa	-6hPa	119hPa
Low	5hPa	96hPa	-38hPa	135hPa

Table4: SEVIRI minus GLAS cloud top differences for GLAS high, middle and low single layer opaque cloud

	Ocean		Land	
	Mean	Rms	Mean	Rms
High	58hPa	99hPa	50hPa	92hPa
Middle	3hPa	123hPa	-21hPa	101hPa
Low	0.5hPa	93hPa	50hPa	140hPa

For the low level cloud over land, there is a bias of 50hPa when only single-layered opaque case is taken into account.

5. CONCLUSION AND PERSPECTIVES

Cloud pressure distributions derived from SEVIRI by

the SAFNWC team have been compared with the POLDER Rayleigh cloud top pressure and the Oxygene cloud pressure for several days in October 2003. These distributions show the same global features and differences than those observed in the first SEVIRI/POLDER cloud pressure comparison operated for several days in June 2003 [4].

However, for low cloud over ocean when comparing June and October 2003 there is a decrease of the Rayleigh pressures and an increase of the SEVIRI pressures. The SEVIRI cloud pressures increase according to the change in algorithm version from 1.0 to 1.2. In October over ocean, the SEVIRI low cloud top pressure is very close to the Oxygene cloud pressure. However, at the present time the Rayleigh pressure increase is not well explained.

For high thick clouds, the SEVIRI and Rayleigh cloud pressures are close and for high thin clouds the SEVIRI pressure is smaller than the Rayleigh one. In October 2003, some very low cloud pressure values are retrieved from the Rayleigh method whereas there were not present in June 2003.

For the same days in October 2003 SEVIRI cloud top pressure has been compared with the cloud top pressure of the highest layer observed with the space lidar GLAS. Unfortunately, accounting for the different overpass times, GLAS and POLDER data are not coincident. Both over ocean and over land the SEVIRI and GLAS pressure distribution shapes are very similar. There is a bias of 67hPa towards higher pressure values for the SEVIRI pressure compared to the GLAS pressure. 62% of the GLAS high clouds are classified high clouds by SEVIRI. For the GLAS single layer opaque high cloud, the bias between the SEVIRI and GLAS cloud top pressure is below 58hPa.

The GLAS middle cloud class does not correspond to a well defined level pressure in the SEVIRI data set. A more precise comparison must be performed to understand this behaviour, in particular the non negligible percentage of low SEVIRI cloud pressure.

Over ocean, for the GLAS low clouds when SEVIRI detects also clouds, the mean difference between the SEVIRI and GLAS cloud top pressure is almost zero but the RMS is close from 95hPa. Over land, more than 55% of SEVIRI low clouds are equally distributed in the clear, middle and high cloud GLAS classes.

As part of the A-train satellite constellation, PARASOL/POLDER has been launched in December 2004, the CALIPSO lidar and the CLOUDSAT radar have joined PARASOL and the A-Train in May 2006. Study of the relation between cloud properties observed from SEVIRI, POLDER and active measurements will be continued in this frame.

6. REFERENCES

- Deschamps, P. Y., F. M. Bréon, M. Leroy, A. Podaire, A. Bricaud, J. C. Buriez, and G. Sèze: The POLDER mission: Instrument characteristics and scientific objectives. *IEEE Trans. Geosci. Rem. Sens.*, **32**, 598-615, 1994.
- Buriez, J. C., C. Vanbauce, F. Parol, P. Goloub, M. Herman, B. Bonnel, Y. Fouquart, P. Couvert, and G. Sèze: Cloud detection and derivation of cloud properties from POLDER. *Int. J. Remote Sensing*, **18**, 2785-2813, 1997.
- Parol, F., J.C. Buriez, C. Vanbauce, P. Couvert, G. Sèze, P. Goloub, and S. Cheinet: Information Content on Clouds from ADEOS-POLDER. *IEEE Trans. Geosci. Remote Sens.*, **37**, 1597-1612, 1999.
- Parol F., J.C. Buriez, C. Vanbauce, J. Riedi, L. C.-Labonnote, M. Doutriaux-Boucher, M. Vesperini, G. Sèze, P. Couvert, M. Viollier, and F.M. Bréon: Review of capabilities of multi-angle and polarization cloud measurements from POLDER, *Adv. Space Res.*, **33**, 1080-1088, 2004.
- Derrien, M. and H. Le Gléau, 2005, MSG/SEVIRI cloud mask and type from SAFNWC. *International Journal of Remote Sensing*, **26**, 4707-4732.
- Derrien, M. and H. Le Gléau, SAFNWC/MSG SEVIRI Cloud Product, Proceeding of the EUMETSAT Meteorological Satellite Conference, 191-198, 2003.
- Sèze, G. and H. Pawlowska: Cloud Cover Analysis with METEOSAT-5 during INDOEX, *J. Geophys. Res.*, **D22**, 28,415, 2001.
- Sèze, G., F.Parol, J.C. Buriez, P. Couvert, M. Doutriaux-Boucher, H. Le Gléau, J. Riedi and C. Vanbauce: Comparison of cloud types observed from SEVIRI and POLDER2. ESA SP-582., 73-77, Proc Second MSG workshop. Salzburg, 9-10 September 2004.
- Schutz B.E., H.J. Zwally, C.A. Shuman, D. Hancock and J.P. DiMarzio: Overview of the ICESat Mission. *Geophys. Res. Lett.*, **32**, L21S01, doi:10.1029/2005GL0240009, 2005.
- Spinhirne, J.D., S.P. Palm, W.D. Hart, D.L. and E.J. Welton 2005: Cloud and Aerosol measurements from GLAS: Overview and initial results, *Geophys. Res. Lett.*, **32**, L22S03, doi:10.1029/2005GL023507.
- User Manual for the PGE01-02-03 of the SAFNWC/MSG: Scientific Part. To be downloaded from www.meteorologie.eu.org/safnwc
- Scientific report an Additional Tuning of MSG PGE01-02-03 following validation activities. To be downloaded from www.meteorologie.eu.org/safnwc
- Derrien, M., H. Le Gléau, J.F.Daloze, M.Haeffelin, 2005: Validation of SAFNWC/MSG cloud products with one year of SEVIRI data. Proceeding of the 2005 EUMETSAT Meteorological Satellite Conference, 95-103.
- Riedi, J., M. Doutriaux-Boucher, P. Goloub, P. Couvert: Global Distribution of Cloud Top Phase from POLDER/ADEOS1. *Geophys. Res. Lett.*, **28**,1707-1710,2000.
- Vanbauce, C., B. Cadet, and R.T. Marchand: Comparison of POLDER apparent and corrected oxygen pressure to ARM/MMCR cloud boundary pressures. *Geophys. Res. Lett.*, **30** (5), 1212, doi:10.1029/2002GL016449, 2003.
- Palm, S., W.Hart, D. Hlavka, E.J. Welton, A. Mahesh, and J. Spinhirne 2002: Geoscience Laser Altimeter System (GLAS) atmospheric data products, algorithm theoretical basis document, version 4.2, pp 137, NASA Goddard Space Flight Center, Greenbelt, Md.

REMOTE SENSING OF WATER AND ICE CLOUDS FROM MSG/SEVIRI

Bernhard Mayer, Luca Bugliaro, Hermann Mannstein, Tobias Zinner, Waldemar Krebs, and Peter Wendling

Deutsches Zentrum für Luft- und Raumfahrt (DLR), Oberpfaffenhofen, 82234 Weßling, Germany

ABSTRACT

Clouds and their interaction with radiation are still one of the main uncertainties in our understanding of present and the prediction of future climate. Within the framework of the MSG RAO-project we have developed a new water and ice cloud detection and microphysical properties remote sensing algorithm, APICS (Algorithm for the Physical Interpretation of Clouds with SEVIRI). An MSG cirrus detection algorithm (MeCiDA) was developed with special emphasis on optically thin ice clouds. Finally, a fast method to derive top-of-atmosphere radiation fluxes from MSG was developed. With these tools we studied the impact of air traffic on cirrus cloud cover and on the Earth's radiation budget. Our current work concentrates on the generation of artificial satellite images, combining our experience with remote sensing of inhomogeneous clouds and radiative transfer. This manuscript is an update of the paper produced for the 2nd RAO workshop and summarizes the final results.

Key words: radiative transfer, cloud, cirrus.

1. INTRODUCTION

According to [1] probably the greatest uncertainty in future projections of climate arises from clouds and their interaction with radiation. A better understanding of clouds and their microphysical and optical properties is therefore crucial for improving the accuracy of climate predictions. The new spectral channels and the absolute calibration of MSG/SEVIRI allow the quantitative determination of cloud optical and microphysical properties. In addition to snapshots, which can also be obtained from polar orbiting satellites with even higher spatial resolution, the high repetition rate of MSG/SEVIRI allows to study diurnal variation of clouds as well as their formation and dissipation and their average lifetime. This will certainly help to gain better insights into the relevant processes required to better represent clouds in general circulation models. Also, the improved detection capability of MSG/SEVIRI will allow a better validation of the parameterization of clouds and in particular their interaction with radiation in general circulation models. Long time series are required for this purpose and we plan to extend our 15 year

European Cloud Climatology (ECC) [2] into the future using MSG/SEVIRI data. While the 15 year time series is subject to the orbital drift of the NOAA satellites which causes a slow shift in the overpass time, this is completely avoided when we make use of the data which are available every 15 Minutes.

In the following, the remote sensing methods developed by our group are described, including a brief outline of the libRadtran radiative transfer model, the cloud remote sensing package APICS, the cirrus detection algorithm MeCiDA, and the retrieval of shortwave and longwave top-of-atmosphere radiative fluxes. A brief summary of some results is given - for a more detailed description an ample list of references is provided where the results are already published or will be published soon.

2. MATERIALS AND METHODS

2.1 Radiative transfers simulations

libRadtran [3] is a flexible and user-friendly model package to calculate radiance, irradiance, and actinic flux for nearly arbitrary input conditions. The model has been jointly developed by one of us (Bernhard Mayer) and Arve Kylling (NILU, Norway) since more than 10 years. The model handles absorption and scattering by molecules and aerosols, as well as detailed water and ice clouds. The underlying surface may be described in terms of a Lambertian albedo or a bi-directional reflectance distribution function (BRDF): Angular models for vegetation [4, 5] and water surfaces including waves and whitecap [6, 7, 8] are implemented. libRadtran provides a choice of radiative transfer solvers, including the discrete ordinate code DISORT [9], a fast two-stream code [10], a polarization-dependent solver (polRadtran) [11], and a three-dimensional radiative transfer code, MYSTIC [12, 13] which is our benchmark tool for radiative transfer under cloudy conditions. To simulate satellite radiance, we usually employ the DISORT solver, version 2.0, which is ideally suited to accurately handle the highly detailed phase functions of water and ice clouds.

libRadtran allows different choices for spectral calculations, including a line-by-line option, different correlated-k distributions, as well as a pseudo-spectral

option based on the LOWTRAN three-term exponential sum fit with a spectral resolution of 20cm^{-1} , adopted from the SBDART code [14]. For the simulation of satellite radiance we currently use the latter, with 15 spectral grid points for each MSG/SEVIRI channel.

The optical properties of water clouds are calculated using Mie theory and tabulated as function of the effective droplet radius. For ice clouds, where the assumption of spherical particles is not applicable, a parameterization of the optical properties by [15, 16] is used. We extended these data (which covered only the solar spectral range), applying the procedure by [15] to a new set of ice particle optical properties kindly provided by Ping Yang to get a consistent parameterization for the complete spectral range covered by MSG/SEVIRI. A double-Henyey-Greenstein approximation of the phase function is used which has been shown to be a good approximation of the theoretical and observed scattering phase functions of non-spherical ice particles [17], even for the calculation of radiance.

2.2 Retrieval of cloud optical properties

We have developed a cloud classification and microphysical property retrieval scheme, APICS (Algorithm for the Physical Interpretation of Clouds with SEVIRI). Cloud classification is based on a prototype of EUMETSAT's scenes analysis software. For cloud detection we use a classical threshold method combining various channels. To retrieve the optical properties of water and ice clouds, a two-channel retrieval scheme has been developed, exploiting a channel without cloud absorption ($0.6\mu\text{m}$) and one with cloud absorption ($1.6\mu\text{m}$). The method follows the traditional approach by [18, 19], with the major difference that for the absorbing channel we selected the $1.6\mu\text{m}$ channel instead of the $3.9\mu\text{m}$ channel. Fig. 1 shows as an example some of the products retrieved from an MSG observation on September 4, 2005 at 12:00 UTC.

2.3 MSG cirrus detection algorithm-MeCiDA

A sophisticated cirrus retrieval scheme MeCiDA (Me-teosat Second Generation Cirrus Detection Algorithm) has been developed for MSG/SEVIRI which is based exclusively on the thermal IR channels and therefore allows a consistent retrieval of cirrus cloud properties for day and night. The retrieval uses threshold tests based on radiative transfer calculations as well as structural tests. For the latter, the water vapor channels proved to be extremely useful: The water vapor absorption screens out the lower atmosphere, thus efficiently separating the high cirrus clouds from low- and mid-level clouds. Due to their characteristic spatial structure, cirrus clouds can easily be separated from water vapor. A reasonable agreement of the MeCiDA results with TERRA/MODIS (Moderate Resolution Imaging Spectroradiometer) data is found: As an example, Fig. 2 shows a comparison between the standard MODIS cirrus product and the MeCiDA output. The agreement is very good, except close to the edges where MeCiDA fails to detect the thin,

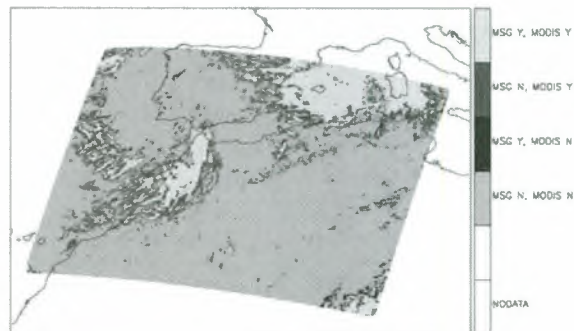


Figure 2. Comparison between the MODIS standard cirrus cloud product and the MeCiDA cloud mask for a specific daytime case. “MSG Y, MODIS Y” indicates pixels where both MODIS and MSG found cirrus clouds etc.

broken cirrus clouds. On average, MeCiDA detects about 60% of the cirrus identified by MODIS. The lower detection rate is to be expected, due to the considerably lower spatial resolution of SEVIRI and the exclusive use of thermal infrared channels by MeCiDA. This slight disadvantage, however, is easily compensated by the 15-minute time resolution of the geostationary MSG which allowed us e.g. to study the correlation between air traffic and cirrus clouds, see below. Details of the retrieval and the validation is described by [20]. A publication is in preparation.

2.4 Shortwave and longwave fluxes from SEVIRI

To study the role of clouds in the radiation budget of the Earth, we have developed an algorithm to derive the reflected solar and the emitted thermal irradiance from MSG/SEVIRI observations. The method is based on a large number of forward simulations with libRadtran which have been used to train a neural network. The method is very fast and compares reasonably well to TERRA/CERES (Clouds and the Earth's Radiation Energy System). The thermal irradiance shows no bias compared to the CERES data while in the solar range our results are higher by up to 10%. A detailed evaluation is in progress. A publication of the method and the validation is in preparation.

3. RESULTS

3.1 Impact of air traffic on climate

According to [21] and the update by [22], the generation of new or the modification of existing cirrus clouds by aircraft exhaust is the least known, but potentially most important effect of air traffic on climate. While the level of understanding of the effect of line-shaped contrails is “fair” according to [21], the so-called “contrail cirrus” is the only component with a “poor” scientific understanding. The reason for this poor understanding is that contrail cirrus cannot be simply distinguished from natural

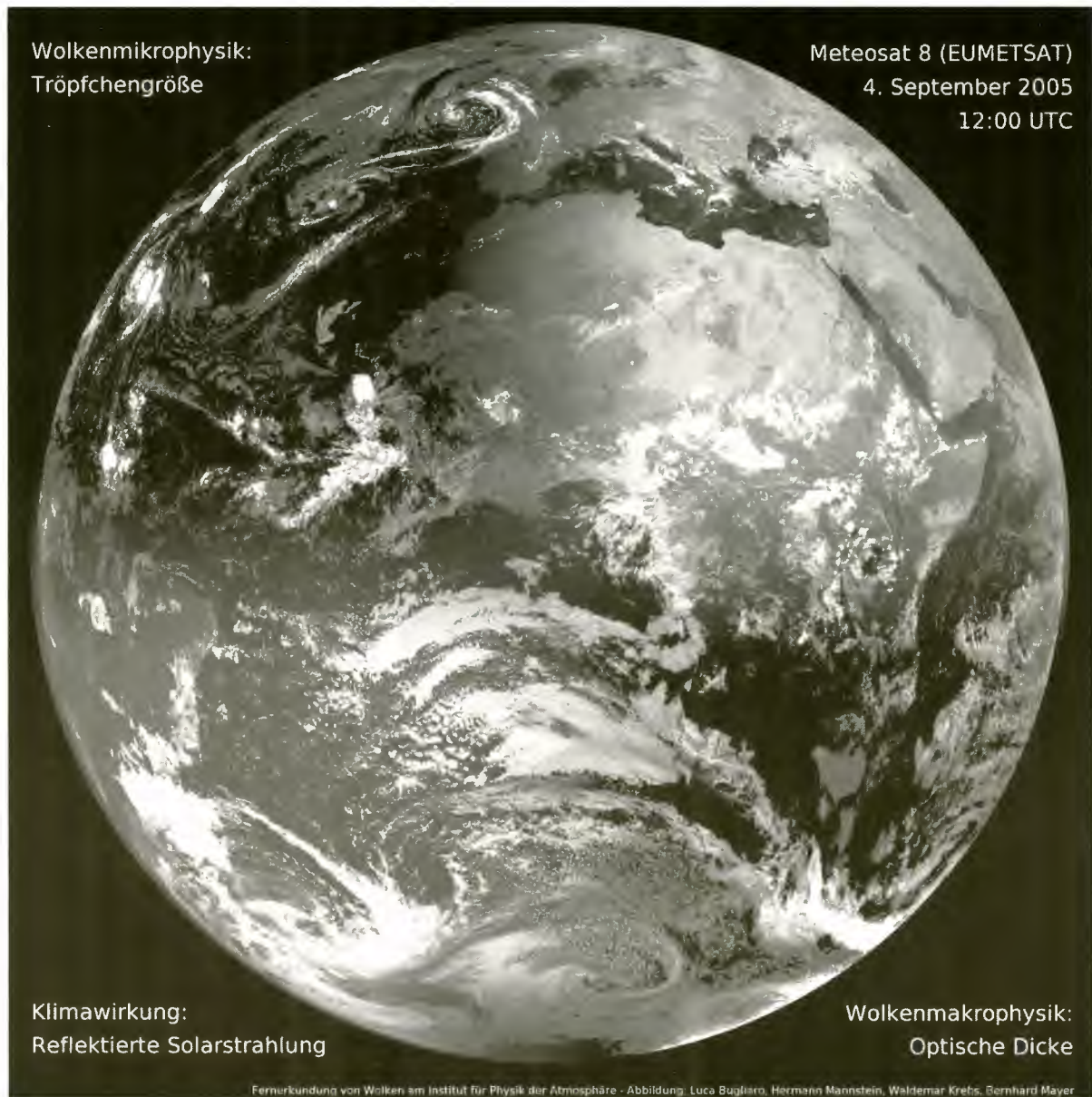


Figure 1. APICS products: (top right) false color composite from the 0.6 μm , 0.8 μm , and 10.8 μm channels; (bottom right) cloud optical thickness; (top left) droplet/particle effective radius; (bottom left) reflected shortwave radiation at top-of-atmosphere.

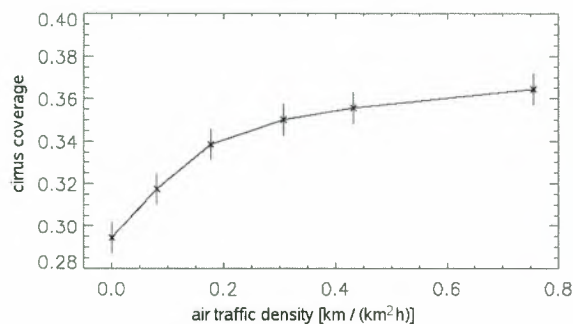


Figure 3. Correlation of cirrus coverage and air traffic density over Europe, averaged over February - December 2004. The air traffic density is defined as the distance flown by aircraft per unit time in a unit area.

cirrus in satellite images. A quantitative characterization of contrail cirrus coverage and radiative forcing can only be done either by relating satellite observations to air traffic data, or by tracing each contrail cirrus starting from a time shortly after its generation where it still can be identified as aircraft contrail by its shape. Following the first strategy, [23] found a significant correlation between air traffic density and cirrus clouds, based on two months of data. Cirrus coverage was derived from Meteosat/MVIRI data. Their results indicated that “the aircraft induced cirrus over Europe is about ten times larger than that of linear contrails in the same region. Radiative forcing from the additional cirrus may be 10 times higher than that of linear contrails and aviation induced CO₂ increases.”

In an ESA DUE project “CONTRAILS” where DLR/IPA was the main contractor, this question was studied in more detail. Fig. 3 shows as an example the correlation between air traffic and cirrus coverage over Europe, averaged over February - December 2004. For the calculation, all MSG/SEVIRI observations every 15 minutes for the complete 11 months have been taken into account. The figure shows a clear increase of cirrus coverage with air traffic. The correlation is statistically significant at 2σ , indicated by the error bars. Details of the analysis, in particular the statistical treatment of the data and the removal of the auto-correlation are described by [20]. A publication is in preparation. The shape of the curve has already been explained by [23]: Persistent contrails form only in regions super-saturated with respect to ice for which reason the cirrus coverage does not increase to 100% but quickly saturates at a much lower value of about 37% in this example. If it is assumed that the aircraft randomly fill the super-saturated areas, an exponential approach towards the saturation limit is expected. To determine the coverage by contrail-cirrus, the curve in Fig. 3 has to be weighted with the frequency of occurrence of air traffic density which results in 1.1% in this case. That is, air traffic over Europe increases the natural cirrus cover over Europe from 29% to 30% according to this study. The next step (which is work in process) is to determine the radiative forcing due to contrail cirrus. A first correlation of the solar and thermal top-of-atmosphere irradiance (derived from MSG/SEVIRI) with air traffic density indicates that air-traffic could have a warming potential much higher than previously assumed, but the uncertainty

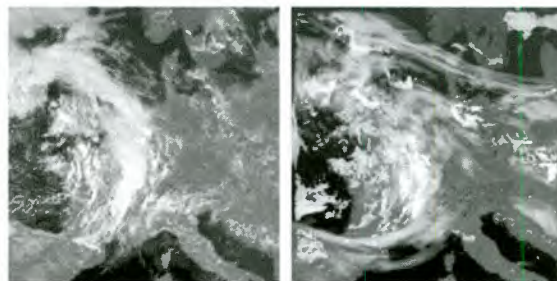


Figure 4. (Left) False color composite of a real MSG/SEVIRI observation from August 12, 2005. (Right) Simulated satellite observation, for the same date and time and processed by the same false color algorithm; the radiative transfer simulation is based on a forecast by the “Lokalmodell” (LM) of the German Weather Service (DWD).

of the preliminary results is rather large. Further studies are required.

3.2 MSG end-to-end simulations

Validation of cloud properties retrieved from space is complex, due to the three-dimensional structure of clouds and their rapid variations in space and time. Coincident observations of cloud microphysical properties in-situ and from space are rare. Most cloud classification schemes are based on threshold tests which are not objective. Furthermore, three-dimensional radiative transfer effects can currently not be considered in retrievals: rather, it is assumed (i) that the cloud properties are constant within the field-of-view of the instrument; (ii) that individual satellite pixels may be considered independent of each other. Both assumptions are not true and cause uncertainties the magnitude of which depends on the resolution of the instrument. One of us (Tobias Zinner) has finished his PhD studies on this subject last year, the results are published in [24, 25].

To overcome these problems, we have started an effort to simulate satellite observations as realistically as possible. With such artificial satellite scenes where the cloud properties as well as the simulated radiation field are known, the performance and accuracy of satellite retrievals can be tested. E.g. the ability of detecting thin cirrus clouds can be tested, or the uncertainty of the retrieved optical thickness for inhomogeneous or broken clouds can be assessed. Fig. 4 shows an example of such a simulated satellite scene. The most critical part in such simulations, in addition to accurate radiative transfer simulations (see section 2.1 of this manuscript), are realistic water and ice clouds. In previous work we have gained experience with highly realistic small-scale clouds, e.g. [24, 25]. However, while these have very high spatial resolution, their size is far too small to simulate any significant part of a satellite scene. For the simulation in Fig. 4, output of the “Lokalmodell” (LM) of the German Weather Service (DWD) was used. The resolution of the operational version of this model is 7 km. The area covered by the image is about 2000 x 2000km². The radiation simulation

was done in one-dimensional approximation, neglecting 3D effects, but considering multiple scattering in water and ice clouds in full detail, using the DISORT2 radiative transfer solver. In future studies, we plan to use either the regional version of the Lokalmodell with enhanced resolution or to down-scale the cloud properties using knowledge about the statistical properties of water and ice clouds.

4. SUMMARY AND CONCLUSIONS

The MSG RAO project formed the framework for a variety of activities in our group where we made extensive use of MSG/SEVIRI data. Funding for this work was provided from a variety of sources, including ESA, EUMETSAT, the European Union, as well as basic funding of DLR.

ACKNOWLEDGMENTS

MSG/SEVIRI data were received and archived in close collaboration with the German Remote Sensing Data Center (DFD). The work on the impact of air traffic contrails and contrail cirrus on climate was funded by the ESA DUE project CONTRAILS. A study on the use of the high-resolution-visible (HRV) channel was funded by EUMETSAT. The development of the cloud property retrieval and the required extensions to the libRadtran radiative transfer code were funded by the DLR PAZI2 project. Last but not least we want to thank ESA and EUMETSAT for the perfect organization of the three RAO workshops which offered a unique opportunity to discuss and exchange MSG-related results.

REFERENCES

- [1] J.T. Houghton, Y. Ding, D.J. Griggs, M. Noguer, P.J. van der Linden, X. Dai, K. Maskell, and C.A. Johnson. Climate change 2001: The scientific basis. Technical report, Intergovernmental Panel on Climate Change (IPCC), IPCC Secretariat, c/o World Meteorological Organization, Geneva, Switzerland, 2001.
- [2] R. Meerkötter, C. König, P. Bissolli, G. Gesell, and H. Mannstein. A 14-year European cloud climatology from NOAA//AVHRR data in comparison to surface observations. *Geophysical Research Letters*, 31:doi:10.1029/2004GL020098, 2004.
- [3] B. Mayer and A. Kylling. Technical Note: The libRadtran software package for radiative transfer calculations: Description and examples of use. *Atmos. Chem. Phys.*, 5:1855–1877, 2005.
- [4] H. Rahman, M.M. Verstraete, and B. Pinty. Coupled surface-atmosphere reflectance (CSAR) model. 1. Model description and inversion on synthetic data. *Journal of Geophysical Research*, 98(D11):20779–20789, 1993.
- [5] H. Rahman, M.M. Verstraete, and B. Pinty. Coupled surface-atmosphere reflectance (CSAR) model. 2. Semiempirical surface model usable with NOAA advanced very high resolution radiometer data. *Journal of Geophysical Research*, 98(D11):20791–20801, 1993.
- [6] C. Cox and W. Munk. Measurement of the roughness of the sea surface from photographs of the sun's glitter. *Journal of the Optical Society of America*, 44(11):838–850, 1954.
- [7] C. Cox and W. Munk. Statistics of the sea surface derived from sun glitter. *Journal of Marine Research*, 13:198–227, 1954.
- [8] T. Nakajima and M. Tanaka. Effect of wind-generated waves on the transfer of solar radiation in the atmosphere-ocean system. *J. Quant. Spectrosc. Radiat. Transfer*, 29(6):521–537, 1983.
- [9] K. Stamnes, S.C. Tsay, W. Wiscombe, and K. Jayaweera. A numerically stable algorithm for discrete-ordinate-method radiative transfer in multiple scattering and emitting layered media. *Applied Optics*, 27(12):2502–2509, 1988.
- [10] A. Kylling, K. Stamnes, and S.-C. Tsay. A reliable and efficient two-stream algorithm for spherical radiative transfer: documentation of accuracy in realistic layered media. *Journal of Atmospheric Chemistry*, 21:115–150, 1995.
- [11] K.F. Evans and G.L. Stephens. A new polarized atmospheric radiative transfer model. *J. Quant. Spectrosc. Radiat. Transfer*, 46(5):413–423, 1991.
- [12] Bernhard Mayer. I3RC phase I results from the MYSTIC Monte Carlo model. In *Intercomparison of three-dimensional radiation codes: Abstracts of the first and second international workshops*. University of Arizona Press, 1999. ISBN 0-9709609-0-5.
- [13] R.F. Cahalan, L. Oreopoulos, A. Marshak, K.F. Evans, A. Davis, R. Pincus, K. Yetzer, B. Mayer, R. Davies, T.P. Ackerman, Barker, H.W., E.E. Clothiaux, R.G. Ellingson, M.J. Garay, E. Kasianov, S. Kinne, A. Macke, W. O'Hirok, P.T. Partain, S.M. Prigarin, A.N. Rublev, G.L. Stephens, F. Szczap, E.E. Takara, T. Varnai, G. Wen, and T.B. Zhuraleva. The International Intercomparison of 3D Radiation Codes (I3RC): Bringing together the most advanced radiative transfer tools for cloudy atmospheres. *Bulletin of the American Meteorological Society*, 86(9):1275–1293, 2005.
- [14] P. Ricchiazzi and C. Gautier. Investigation of the effect of surface heterogeneity and topography on the radiation environment of Palmer Station, Antarctica, with a hybrid 3-D radiative transfer model. *Journal of Geophysical Research*, 103(D6):6161–6178, mar 1998.
- [15] J.R. Key, P. Yang, B.A. Baum, and S.L. Nasiri. Parameterization of shortwave ice cloud optical properties for various particle habits. *Journal of Geophysical Research*, 107(D13):10.1029/2001JD000742, 2002.
- [16] P. Yang, K.N. Liou, K. Wyser, and D. Mitchell. Parameterization of the scattering and absorption

- properties of individual ice crystals. *Journal of Geophysical Research*, 105(D4):4699–4718, 2000.
- [17] A. Gonzalez, P. Wendling, B. Mayer, J.-F. Gayet, and T. Rother. Remote sensing of cirrus cloud properties in the presence of lower clouds: An ATSR-2 case study during the Interhemispheric Differences in Cirrus Properties From Anthropogenic Emissions (INCA) experiment. *Journal of Geophysical Research*, 107:10.1029/2002JD002535, 2002.
- [18] T. Nakajima and M.D. King. Determination of the optical thickness and effective particle radius of clouds from reflected solar radiation measurements. Part I: Theory. *Journal of the Atmospheric Sciences*, 47:1878–1893, 1990.
- [19] T. Nakajima, M.D. King, J.D. Spinhirne, and L.F. Radke. Determination of the optical thickness and effective particle radius of clouds from reflected solar radiation measurements. Part II: Marine stratocumulus observations. *Journal of the Atmospheric Sciences*, 48:728–750, 1991.
- [20] W. Krebs. *Analyse des Einflusses des Flugverkehrs auf die natürliche Zirrusbewölkung über Europa, Nordafrika und dem Nordatlantik*. PhD thesis, Fakultät für Physik der Ludwig-Maximilians-Universität München, 2006.
- [21] J.E. Penner, D.H. Lister, D.J. Griggs, D.J. Dokken, and M. McFarland. Aviation and the global atmosphere. Technical report, Intergovernmental Panel on Climate Change (IPCC), IPCC Secretariat, c/o World Meteorological Organization, Geneva, Switzerland, 1999.
- [22] R. Sausen, I. Isaksen, V. Grewe, D. Hauglustaine, D.S. Lee, G. Myhre, M.O. Köhler, G. Pitari, U. Schumann, F. Stordal, and C. Zerefos. Aviation radiative forcing in 2000: An update on IPCC (1999). *Meteorologische Zeitschrift*, 14(4):555–561, 2005.
- [23] H. Mannstein and U. Schumann. Aircraft induced contrail cirrus over Europe. *Meteorologische Zeitschrift*, 14(4):549–554, 2005.
- [24] T. Zinner, B. Mayer, and M. Schröder. Determination of 3D cloud structures from high resolution radiance data. *Journal of Geophysical Research*, 111(D8):doi:10.1029/2005JD006062, 2006.
- [25] T. Zinner and B. Mayer. Remote sensing of stratocumulus clouds: Uncertainty and biases due to inhomogeneity. *Journal of Geophysical Research*, 2006. accepted.

MSG FOG AND LOW STRATUS PRODUCTS AT LCRS (SOFOS)

Jan Cermak, Jörg Bendix, Thomas Nauß

Laboratory for Climatology and Remote Sensing, University of Marburg,
Deutschhausstr. 10, 35037 Marburg, Germany,

Email: cermak@staff.uni-marburg.de, bendix@staff.uni-marburg.de, nauss@staff.uni-marburg.de

ABSTRACT

This paper presents the Satellite-based Operational Fog Observation Scheme (SOFOS) developed at the Laboratory for Climatology and Remote Sensing (LCRS), University of Marburg, Germany, based on Meteosat 8 SEVIRI data. The scheme currently consists of four components: Daytime very low stratus detection, daytime ground fog delineation, fog dissipation modelling and nighttime low stratus detection. Each of these is briefly introduced in the following.

1. MOTIVATION AND OBJECTIVES

Fog, which often occurs in Central European winter can lead to severe obstructions to air, road and sea traffic. It also impacts on air quality and acts as a modifier in the climate system. The spatially distinct nowcasting of fog using NWP (*N*umerical *W*eather *P*rediction) models, statistical procedures or point observations is still problematic [1].

The Meteosat 8 SEVIRI system with its advanced temporal, spectral and spatial resolutions is an excellent tool for the detection and very short range forecasting of fog, fog properties and fog dynamics.

The current study based on Meteosat 8 data has four main goals:

- (1) Introduce a technique for operational daytime low stratus detection
- (2) Offer a proper discrimination between ground fog and low stratus.
- (3) Predict the dissipation time for fog areas identified from satellite imagery.
- (4) Present a stable technique for nighttime low stratus detection.

The algorithms developed are based on satellite data alone, with the potential for unsupervised and operational application.

This paper presents results obtained in the development of the SOFOS fog detection and description scheme at the Laboratory for Climatology and Remote Sensing, University of Marburg, Germany.

2. DAYTIME LOW STRATUS DETECTION

The classification approach presented here relies on a combination of tests based on the spectral properties of individual pixels and a spatially oriented approach, focussing on the properties of a spatially coherent group of pixels in its individual context (see figure 1).

Initially, spectral tests serve to separate cloudy from clear pixels (10.8 μ m, 3.9 μ m), exclude snow pixels

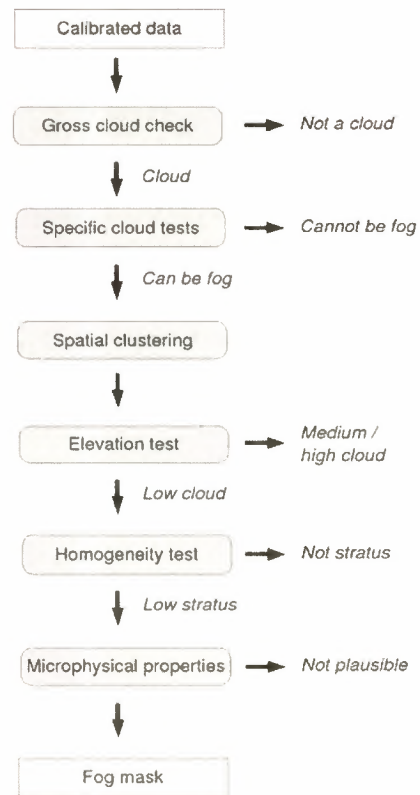


Fig. 1. Outline of the daytime low stratus detection scheme

(0.6 μ m, 0.8 μ m, 1.6 μ m, 10.8 μ m), remove ice clouds (8.7 μ m, 10.8 μ m, 12.0 μ m) and identify small droplet cloud areas (3.9 μ m). This provides an initial orientation as to what pixels may potentially be covered by fog. These pixels are then taken as the basis for spatial testing.

In spatial testing, spatially coherent and discrete areas of these potential fog pixels are assigned individual IDs and henceforth treated as separate entities. Each of these entities then undergoes two simple tests:

a) Cloud altitude test

The purpose of this test is to identify whether or not a given cluster could be a low cloud. The 10.8 μ m brightness temperature differences between each of the marginal pixels and any adjacent clear pixels are determined. The maximum difference is taken as the point of reference. At this point, the surface elevation of each of the two compared pixels is extracted from a digital elevation model (DEM). Using an assumed

atmospheric temperature gradient and a predefined 'low cloud' threshold temperature, the cluster is now either classified as a potentially low cloud or taken out of the classification scheme.

b) Cloud top height homogeneity test

Based on the assumption that fog should have a fairly homogeneous surface height at the inversion, the second spatially oriented test probes for this property. Since no direct information about cloud to height is available and only relative information is needed, 10.8 μm brightness temperature is taken as a proxy.

The method is described in detail in [2].

3. DAYTIME GROUND FOG DELINEATION

In order to distinguish between low stratus without ground contact and genuine ground fog (i.e. cloud in touch with the ground), some information on cloud geometry is needed (see figure 2). Along the lines of this concept, a comparison between cloud base height and ground surface elevation can serve to decide whether or not ground fog is present in a given location.

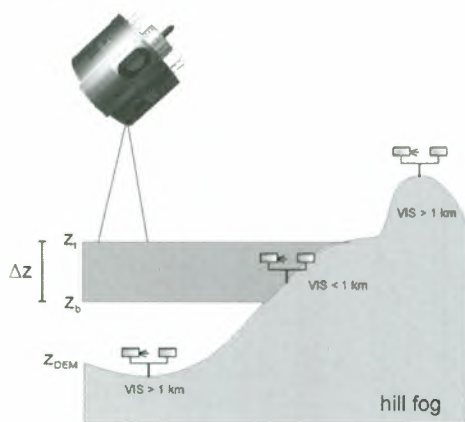


Fig. 2. The problem of fog / low stratus distinction from satellites

Surface elevation is known from a digital elevation model (GTOPO30, [3]). Cloud base height is a function of cloud top height and cloud geometrical thickness. Cloud top height is retrieved using an entity-based spatial interpolation of margin-pixel elevations partly derived from the DEM and partly computed using atmospheric lapse rates, depending on the relief situation.

Cloud base height is retrieved using a subadiabatic model of cloud microphysics. Based on a range of cloud observations, this model approximates the development of cloud liquid water content with altitude above cloud base. The input fed into this model are

- cloud liquid water path (LWP) retrieved from SEVIRI imagery following the method proposed by [4]
- cloud top height

- cloud top temperature (with atmospheric corrections)

The model is then run several times for each given set of parameters until optimum agreement between model LWP and actual, satellite-retrieved LWP is reached. The corresponding cloud base height is then compared with the DEM surface elevation to compute a ground fog probability level. The method is described in full in [5].

4. FOG DISSIPATION MODEL

The very short range forecasting of fog clearance is of great importance especially for sea, air and road traffic management. Nowadays, numerical models are still too slow for the forecasting of fog clearance in space in the short temporal range [1]. For that reason, a straightforward thermodynamical model of fog clearance was developed and applied to NOAA AVHRR data. It uses in situ data of air temperature, lapse rate at model start, spatial interpolation techniques and a digital elevation model for the retrieval of fog geometrical thickness [6]. The model has recently been adapted to Meteosat 8 SEVIRI data with some slight modifications:

- (1) The radiation scheme was improved by using the model equations of [7].
- (2) The calculation of broadband albedo makes use of SEVIRI band 1 (0.635 μm).
- (3) Initial fog temperature is now calculated from SEVIRI band 9 (10.8 μm), with a correction for atmospheric transmission and fog optical depth [8, 9].
- (4) Fog optical and microphysical properties are retrieved by using the approach of [9].
- (5) Fog geometrical thickness is estimated by using fog optical depth and the empirical equation of [10].

Model performance was analysed in detail for 5 November 2003. Fog covers most river valleys in the lower mountain ranges of Germany and the pre-Alpine basins at 10 UTC. The binary fog mask shows that most fog layers have cleared until 12 UTC. Only the fog layer in the upper Rhine valley and some small patches on the Swiss plateau and in the Po Valley area persist.

The model mask for 12 UTC reveals encouraging agreement with the real situation. However, some pixels clear too early or too late (e.g. Po Valley fog).

Sensitivity studies have shown that fog geometrical / optical thickness and LWP are the most crucial parameters for proper model results. The estimates of these values should therefore be as accurate as possible. Accurate retrievals are especially problematic in cases of mixed pixels as can be seen in the upper Rhine valley fog patch. Rim pixels and the pixel for the city of Freiburg clear too quickly because optical depth (and as a result geometrical thickness) and LWP are underestimated. A pilot study using MODIS showed that the Heidinger and Stephens formula underestimates fog thickness with increasing optical depth. Future activities will investigate the accuracy of the model. It will be used in an auto-adaptive scheme where fog clearance time is updated every 15 minutes in accordance with Meteosat 8's temporal resolution. A special treatment of mixed pixels using the HRV channel is under

investigation.

5. NIGHTTIME LOW STRATUS DETECTION

The detection of low stratus layers from nighttime satellite imagery has a long tradition. Most studies rely on the 3.7 μm band of the AVHRR sensor aboard the NOAA satellite series [e.g. 12, 13]. The common technique utilizes differences in small-droplet emissivities at 11 μm and 3.9 μm [14]. On Meteosat SEVIRI however, this method cannot be applied with a fixed threshold due to instrument design: the 3.9 μm band is exceptionally wide and overlaps with the 4 μm CO₂ absorption band (see figure 3).

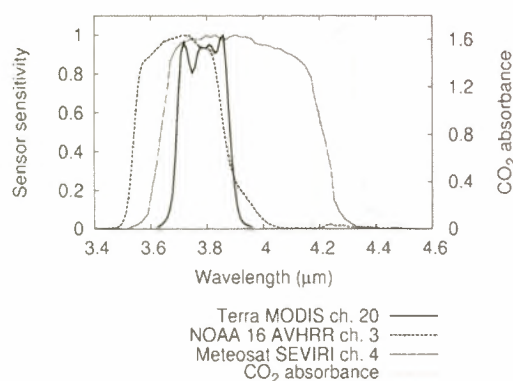


Fig. 3. Overlap between the SEVIRI MIR channel and the CO₂ band.

The effect of CO₂ absorption therefore reduces the SEVIRI 3.9 μm radiance signal. The strength of this effect varies with season and the length of the atmospheric path, i.e. satellite viewing angle. Therefore a new method was developed that dynamically determines a 10.8 μm -3.9 μm blackbody temperature difference threshold based on latitude-dependent histogram analysis. A description of this scheme and validation cases are found in [15].

6. CONCLUSIONS AND OUTLOOK

The fog detection scheme introduced in this paper has been tested in operational processing and is being further developed. Selected validation results can be found in [2, 3]. The combination of pixel-based and spatially oriented techniques provides for a fairly stable performance. A major issue to be tackled in the near future is that of nighttime ground contact. Also, the inclusion of the High Resolution Visible (HRV) channel information at daytime promises to provide access to further spatial information.

The fog clearance model also shows encouraging results in the initial static version implemented to date. Once included in operational processing as an auto-adaptive scheme, significant improvements are expected.

ACKNOWLEDGEMENTS

This research is generously funded by the German Research Council DFG (BE 1780/8-1, 3) within the NEKAMM project. The study is part of the EU COST action 722 and the ESA/EUMETSAT MSG RAO PI programme (ID 141).

REFERENCES

1. Jacobs W., et al. (eds.), *COST 722 Phase 1 Report: Very Short Range Forecasting of Fog and Low Clouds: Inventory Phase on Current Knowledge and Requirements by Forecasters and Users*. <http://www.lcrs.de>, 184pp, 2003.
2. Cermak J. and Bendix J., A Novel Approach to Fog/Low Stratus Detection using Meteosat 8 Data *Atmospheric Research*, accepted.
3. USGS, Digital elevation models, *United States Geological Survey technical report*, 1993.
4. Kawamoto K., et al., A Global Determination of Cloud Microphysics with AVHRR Remote Sensing. *J. Clim.*, 14, 2054-2068, 2000.
5. Cermak J., *SOFOS -- A New Satellite-based Operational Fog Observation Scheme*. PhD thesis, Philipps-Universität Marburg, Fachbereich Geographie, 2006.
6. Reudenbach Ch. and Bendix J., Experiments with a straightforward model for the spatial forecast of fog/low stratus clearance based on multi-source data. *Met. Appl.*, Vol. 5, 205-216, 1998.
7. Iqbal M., *An introduction to solar radiation*, Academic press, Toronto, 1983.
8. Saunders R.W., Cloud-top temperature/height: A high-resolution imagery product from AVHRR data. *Met. Mag.*, Vol 117, 211-221, 1988.
9. Nakajima T.Y. and Nakajima T., Wide-area determination of cloud microphysical properties from NOAA AVHRR measurements for FIRE and ASTEX regions. *J. Atm. Sci.*, 52, 4043-4059.
10. Heidinger A.K. and Stephens G.L., Molecular line absorption in a scattering atmosphere. Part II: Application to remote sensing in the O₂ A band. *J. Atm. Sci.*, 57, 1615-1634, 2000.
11. Bendix J., A Satellite-Based Climatology of Fog and Low-Level Stratus in Germany and Adjacent Areas. *Atm. Res.*, Vol. 64, 3-18, 2002.
12. Eyre J.R., Brownscombe J.L. and Allam R.J., Detection of fog at night using Advanced Very High Resolution Radiometer (AVHRR) imagery. *Meteorological Magazine*, 113, 266-271, 1984.
13. Underwood S. J., et al. A Multiple-Case Analysis of Nocturnal Radiation-Fog Development off California Utilizing GOES Nighttime Fog Product. *J. Appl. Met.*, Vol. 43, 297-311, 2004.
14. Hunt G.E., Radiative properties of terrestrial clouds at visible and infra-red thermal window wavelengths. *Quarterly Journal of the Royal Meteorological Society*, 99, 346-369, 1973.
15. Cermak J. and Bendix J., Dynamical Nighttime Fog/Low Stratus Detection Based on Meteosat SEVIRI Data - A Feasibility Study. *submitted to Journal of Pure and Applied Geophysics*

ENERGY-SPECIFIC SOLAR RADIATION DATA FROM MSG: THE HELIOSAT-3 PROJECT

Marion Schroedter-Homscheidt, Jethro Betcke¹, Hanne Breitzkreuz, Annette Hammer¹, Detlev Heinemann¹, Susanne Heinicke¹, Elke Lorenz¹, Sibylle Petrak¹, Thomas Holzer-Popp, Lucien Wald²

*Deutsches Zentrum für Luft- und Raumfahrt e.V. (DLR)
Deutsches Fernerkundungsdatenzentrum (DFD)
Oberpfaffenhofen, D-82234 Weßling, Germany
phone: ++49-8153-28-2896, fax ++49-8153-28-1445
e-mail: Marion.Schroedter-Homscheidt@dlr.de*

¹ Universität Oldenburg, Abteilung Energie- und Halbleiterforschung

² Armines / Ecole des Mines de Paris

ABSTRACT

Solar energy technologies such as photovoltaics, solar thermal power plants, passive solar heating/cooling systems and day lighting in buildings are expected to continue their very rapid growth. In this context the availability of reliable solar radiation data is of high economic value both for planning and operating these systems.

HELIOSAT-3 aims the quantification of surface solar irradiance in cloud free and cloudy situations and additional energy-specific parameters as direct normal and diffuse irradiance over Europe and Africa using the enhanced capabilities of MSG. Emphasis is laid on clouds, water vapor, aerosols and ozone and their influence on surface solar irradiance.

Several projects as e.g. the HELIOSAT-3 and PVSAT-2 European Commission FP5 and the ENVISOLAR (ESA Earth Observation Market Development Program) projects made profit from the data access and additional MSG product information obtained through the RAO program. The paper focuses on results obtained during the RAO project based on funding in HELIOSAT-3, PVSAT-2 and ENVISOLAR projects.

INTRODUCTION

The Heliosat method [1, 2] was developed for Meteosat First Generation to calculate surface solar irradiance from measurements in the visible channel. It is supposed that the sunlight reflected by clouds is inversely related to the sunlight transmitted by them. The scheme takes the variability of the cloud field and its impact on hourly global and diffuse irradiance into account. Together with a sophisticated model of clear sky irradiance [3] this method gives reliable results for Europe for most of the year.

Potential for improvement is expected in winter time especially in snow covered areas, during morning and evening hours due to three-dimensional effects of clouds to be described with cloud physical parameters and in the clear sky case using more detailed input information on aerosols and water vapor. Therefore, a

new scheme called Heliosat-3 was developed in the MSG-RAO and EU FP5 programs (Fig. 1).

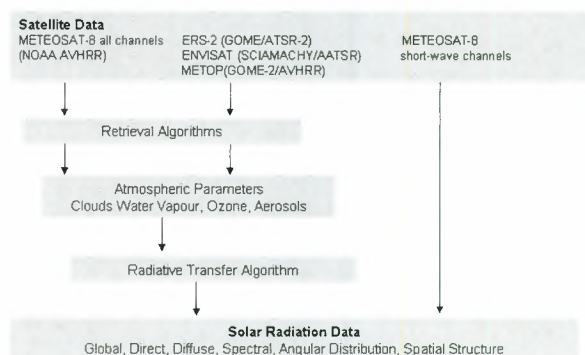


Figure 1. Heliosat-3 scheme [4]

SNOW COVER

The old Heliosat method fails in wintertime, when snow is covering the surface under clear skies. Due to their high reflectances these cases are falsely classified as overcast, which leads to a remarkable error in the global irradiance values. Fig. 2 gives an example of an existing photovoltaic (PV) system showing high energy yield on 11th February 2006 while the satellite-based estimate is lower due to an error in snow-cloud discrimination.

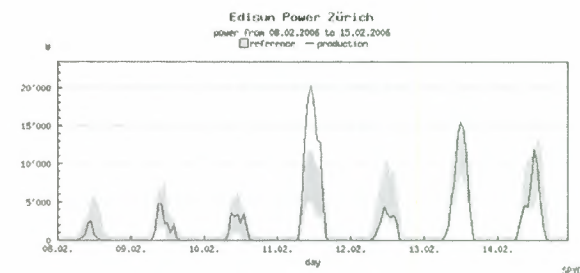


Figure 2. Hourly effective energy production (solid line) and reference yields (yellow) of a PV plant (Source Enecolo SPYCE service).

Even the opposite effect is observed as e.g. in Fig. 3. In this case the PV system delivers an energy yield close to zero due to snow cover on the modules while the satellite-based energy production estimate reaches 1500

W as usual for a sunny situation in wintertime. In case the snow cover is known, the assumption of a total hardware failure can be denied and a false alarm to the system maintenance staff can be avoided.

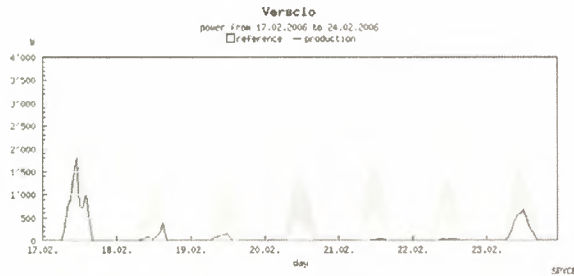


Figure 3. Hourly effective energy production (solid line) and reference yields (yellow) of a PV plant (Source Enecolo SPYCE service).

The MSG channels give the opportunity to discriminate snow from clouds and to reduce this error source. A multi-temporal snow cover detection algorithm was developed [5, 6]. Snow maps are derived in 3x3 km² nadir SEVIRI pixel resolution and superimposed to cloud index maps derived from HRV reflectances (1x1 km²) by an adapted Heliosat method. Results are given in Fig. 4. While some falsely detected snow pixels lead to an overestimation of global irradiance, the remarkable underestimation of a method without snow detection vanishes.

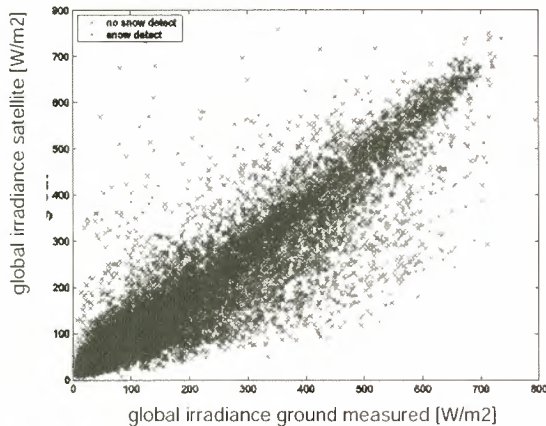


Figure 4. Hourly global irradiance with (blue) and without snow detection (red) for 20 German stations in February – March 2005

GEOMETRICAL CORRECTION USING CLOUD HEIGHT

MSG has another opportunity to gain a better quality in the derived surface irradiance, namely the higher resolution in space and time compared to MFG. When

making full use of this high resolution data, a three dimensional consideration is optimal. A cloud in the sky has its largest effect on the irradiance measured at the ground when it is affecting the direct beam. For a given pixel the clouds between pixel and sun must be analyzed instead of the clouds between the pixel and the observer (MSG). For a geometric correction of this effect cloud top height is needed and can be provided by MSG SEVIRI. In a first approach a standard cloud of 1 km thickness and a seasonal variation of cloud top height was assumed. Fig. 5 gives validation results for global irradiances measured at the ground station Vaulx-en-Velin (France) for the period March – August 2004 and November 2004 – February 2005. Fig. 6 presents the same analysis but for Freiburg (Germany). A remarkable improvement in monthly root mean square errors (RMSE) can be noticed. The next step will be the use of MSG based cloud top height information.

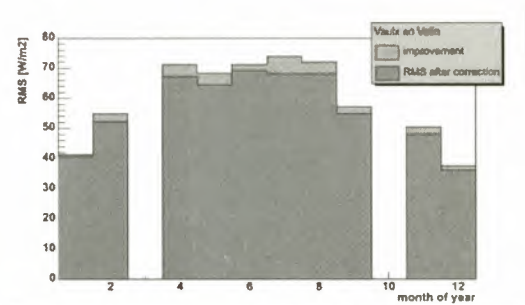


Figure 5. Improvement in monthly RMSE of hourly global irradiance for Vaulx-en-Velin (France) due to a geometrical correction for cloud height.

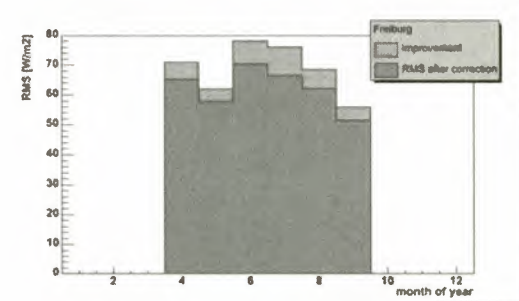


Figure 6. Improvement in monthly RMSE of hourly global irradiance for Vaulx-en-Velin (France) due to a geometrical correction for cloud height.

VALIDATION OF THE HELIOSAT-3 METHOD

Taking the better spatial resolution of MSG-HRV in comparison to the old Meteosat satellite, the new capabilities for snow detection and a basic geometrical correction into account, an overall validation has been performed for 20 DWD ground stations measuring global irradiance for the full year of 2005 (Fig. 7). The overall bias for hourly values decreases from -1.2% for

METEOSAT-7 to 0.4% for METEOSAT-8 and the standard error decreases from 19.5% to 17.8%.

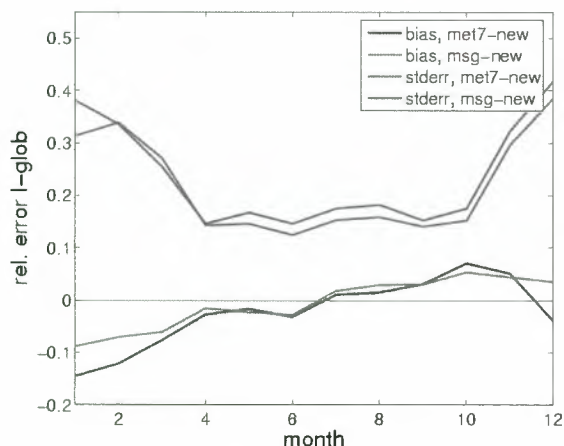


Figure 7. Improvement in monthly bias and standard error of hourly global irradiance for 20 DWD ground stations in 2005.

A significant improvement can be noticed in the winter months due to snow detection. During the summer months a slight improvement in standard error can also be noticed which is attributed to the increased spatial resolution of the HRV channel.

NEED FOR AEROSOL INFORMATION

It has been stated e.g. by [7] that accurate aerosol information is crucial for irradiance calculations in the clear sky case. Climatologies or model output data sets with a typical grid size of 3 to 5° are currently available. Fig. 8 shows the RMSE in aerosol optical thickness at 550 nm to be expected for hourly values if such climatologies are used.

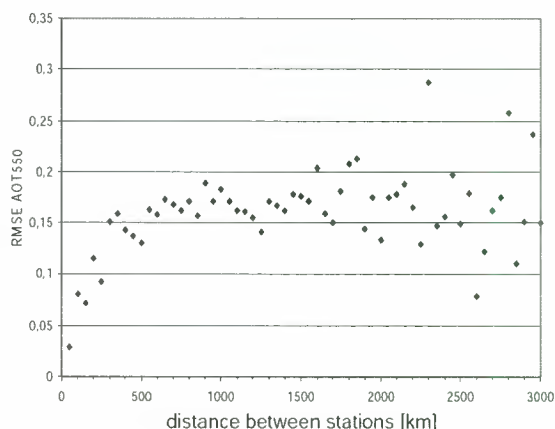


Figure 8. Variogram based on 30 European AERONET ground measurements of AOT at 550 nm in 2003.

This analysis was performed using AERONET ground measurements [8] for 30 European stations in 2003. Data from the year 2004 reveal similar results. From that analysis it can not be expected that new global data sets with a spatial resolution of several degrees can improve the situation remarkably. This is in line with the findings of the solar energy community that the use of different existing aerosol climatologies or recently made available model data sets did not increase the accuracy.

On the other hand, the new ENVISAT and the upcoming METOP satellites with the SCIAMACHY and GOME-2 instruments and a pixel size around 0.5° have the potential to deliver aerosol information in a spatial resolution more suitable for this user community. Yet, to account for the temporal and spatial variability of aerosols, an optimum retrieval scheme would deliver products in the same temporal and spatial resolution as MSG-SEVIRI.

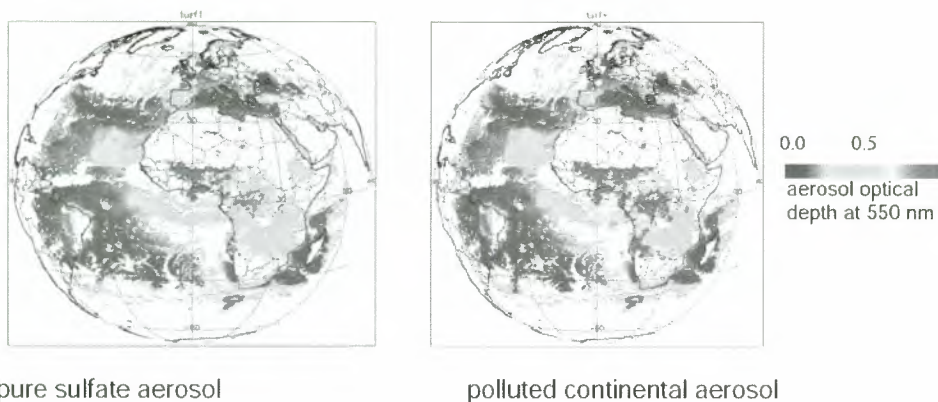


Figure 9. Aerosol optical depth at 550nm derived from MSG SEVIRI on 1st August 2004 assuming fixed aerosol types.

AEROSOL STUDY BASED ON MSG

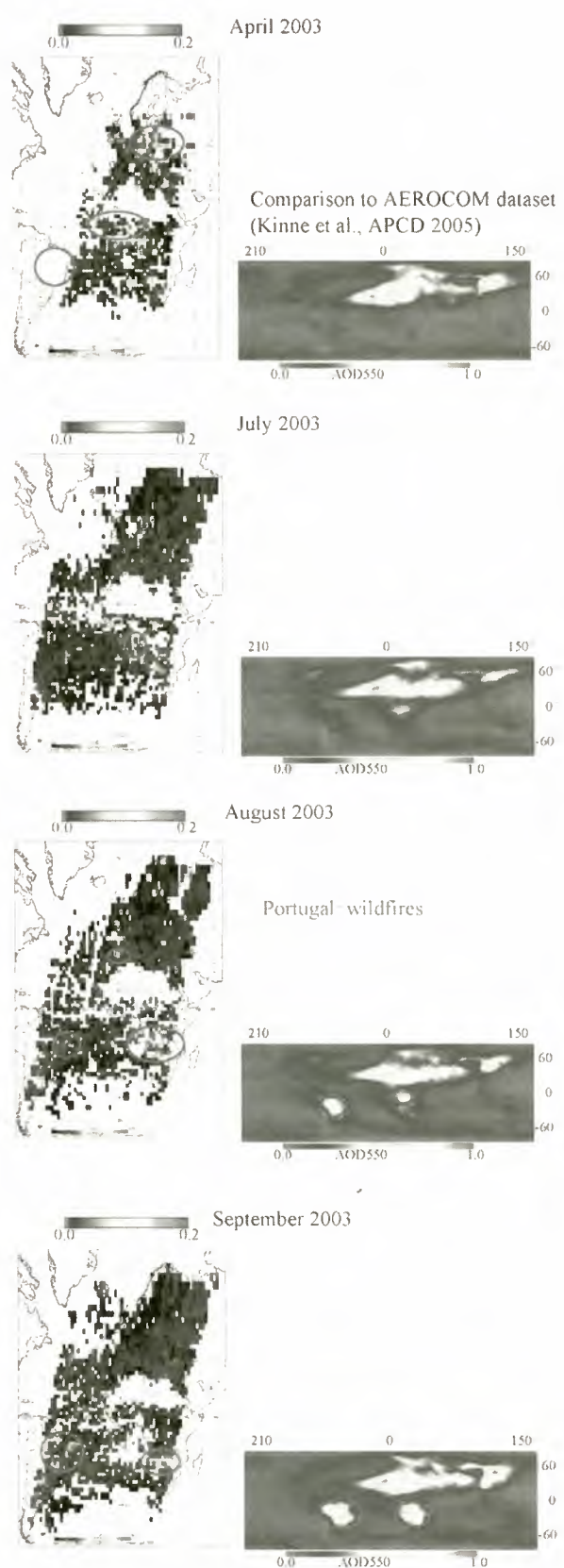
Therefore, the SYNAER method was applied for SEVIRI. The SYNAER method (SYNergetic AERosol Retrieval, [Holzer-Popp]) delivers boundary layer aerosol optical depth (AOD) and type over both land and ocean. After cloud detection, AOD is calculated over automatically selected and characterized dark pixels and surface albedo correction for a set of 40 different pre-defined boundary layer aerosol mixtures is performed. A least square fit of a simulated spectrum based on the corrected surface albedo to the MSG SEVIRI channels delivers the AOD value. Unfortunately, MSG SEVIRI has no blue channels, which means that the spectrum is not covered complete. Therefore, accurate aerosol retrieval cannot be expected. Nevertheless, in the HELIOSAT-3 project a case study was made to quantify the dependence on aerosol type for an example case. Fig. 9 gives the SYNAER results for MSG-SEVIRI on 1st August 2004 assuming fixed aerosol types of pure sulfate and of a polluted continental aerosol. Large differences in quantitative values can be observed due to the missing aerosol type information as result of the missing spectral resolution of SEVIRI in the blue spectral region.

This test trial reveals clearly, that aerosol type information has to be provided as auxiliary data set to a SEVIRI-based aerosol retrieval scheme. It is proposed to provide such information from polar satellites as e.g. ENVISAT and in future METOP as they have opportunities to separate major aerosol types. Therefore, the next section reports on recent results in retrieving aerosol type information from ENVISAT AATSR and SCIAMACHY using SYNAER in the PROMOTE project.

AEROSOLS FROM ENVISAT

For ENVISAT, the high spatial resolution of the AATSR instrument (Advanced Along Track Scanning Radiometer) permits accurate cloud detection, dark pixel selection and surface albedo correction. After spatial integration to the larger pixels of the spectrometer SCIAMACHY (SCanning Imaging Absorption spectroMeter for Atmospheric Cartography) these parameters are used to simulate SCIAMACHY spectra for the same set of different aerosol mixtures.

SYNAER has been implemented for operational processing at the German Remote Sensing Data Center within the ESA GSE PROMOTE (Protocol Monitoring for the GMES Service Element; see also <http://www.gse-promote.org>) and delivers daily near-real time observations (within the same day) and an evolving archive of historic data.



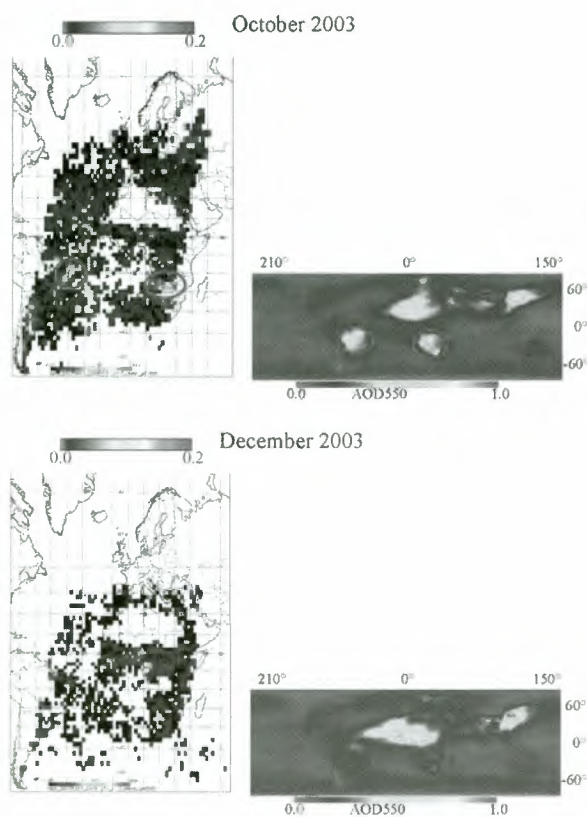


Figure 9: Seasonal variation of soot: monthly mean maps of soot aerosol optical depths for the months April, July, August, September, October 2003, and December 2005 are shown from top to bottom. As comparison the AEROCOM climatology [10] is given.

The seasonal behavior visible in the SYNAER data is shown in Fig. 9 for the soot component. Here, three major features can be seen: From July to September the tropical African biomass burning moves South and East together with its plume over the Atlantic (which is slightly visible). The Amazonian biomass burning season mainly extends from August to October. Over large parts of Europe, no data are available in December (due to low sun, high cloudiness and snow cover). Highest European soot concentrations are detected, when observations are becoming available still in the heating season (April). Additionally, wildfires in August (hot summer 2003) contribute to elevated soot over the Iberian peninsula.

CONCLUSIONS

Starting from the fact that large inconsistencies in existing irradiance data bases available for solar energy engineering, the Heliosat-3 RAO project aimed at using the enhanced temporal, spatial and spectral resolution of the Meteosat Second Generation SEVIRI instrument for an improved derivation of global and direct irradiance.

It was shown, that cloud top height is needed to account for basic three-dimensional effects of clouds in radiative transfer. In future, SEVIRI derived cloud top heights will be included in a modified cloud index scheme as part of the new Heliosat-3 method.

Additionally, snow detection allows avoiding errors due to misdetection of clouds as snow and vice versa. It helps to decide on a possible hardware failure in automatic failure detection routines for photovoltaic system monitoring.

A parameterization scheme (SOLIS, [3]) based on radiative transfer calculations was developed which allows to take actual information on aerosol optical depth, angstrom coefficient and water vapor concentration into account. There is an urgent need for improved aerosol optical depth information in a better spatial and temporal resolution than available nowadays from global models and climatologies. Therefore, SYNAER aerosol retrievals were analyzed both for a test trial with MSG SEVIRI and for ENVISAT. The trial for SEVIRI shows the clear need for aerosol type information as input for any aerosol optical depth retrieval scheme using SEVIRI.

ENVISAT based SYNAER results show first successful results on the discrimination of water soluble and soot results, while the large aerosol particles from mineral and sea salt sources are still a subject of further work.

Follow-on activities will be performed in the virtual Institute of Energy Meteorology (vIEM), the ESA GSE PROMOTE and on the market development for solar energy services based on Earth observation within the ESA EOMD project ENVISOLAR.

REFERENCES

1. Cano, D., Monget, J., Albuissou, M., Guillard, H., Regas, N., and Wald, L., A method for the determination of the global solar radiation from meteorological satellite data, *Solar Energy*, 37, 31–39, 1986.
2. Beyer, H., Costanzo, C., Heinemann, D., Modifications of the Heliosat procedure for irradiance estimates from satellite images, *Solar Energy*, 56, 207–212, 1996.
3. Müller, R.W., K. F. Dagestad, P. Ineichen, M. Schroedter-Homscheidt, S. Cros, D. Dumortier, R. Kuhlemann, J.A. Olseth, G. Piernavieja, C. Reise, L. Wald, D. Heinemann, Rethinking satellite-based solar irradiance modeling - The SOLIS clear-sky module, *Remote Sensing of Environment*, 91, 160-174, 2004.
4. Zelenka, A., Science Review ENVISOLAR project, <http://www.envisolar.com>, 2004
5. Heinicke, S., Schneerkennung auf Basis von multispektralen und multitemporalen Meteosat-8-Informationen - Einbettung in das bestehende Verfahren der Heliosat-Methode, Diploma Thesis University of Oldenburg, 2006

6. De Ruyter de Wildt, M., Seitz, G., Grün, A., Snow mapping using multi-temporal Meteosat-8 data, *EARSEL eProceedings* 5, 1/2005.
7. Gueymard, C. A., Direct solar transmittance and irradiance predictions with broadband models. Part I: detailed theoretical performance assessment, *Solar Energy*, 74, 355-379, 2003.
8. Holben, B.N., et al, AERONET: A federated instrument network and data archive for aerosol characterization, *Remote Sensing of Environment*, 66, 1-16, 1998.
9. Holzer-Popp, T., Schroedter, M., & Gesell, G., Retrieving aerosol optical depth and type in the boundary layer over land and ocean from simultaneous GOME spectrometer and ATSR-2 radiometer measurements: 1. Method description, *Journal of Geophysical Research*, 107(D21), 4578, 2002.
- 10 Kinne, S., An AeroCom initial assessment – optical properties in aerosol component modules of global models, *Atmos. Chem. Phys. Discuss.*, 5, 8285–8330, 2005.

IMPROVEMENT AND VALIDATION OF THE OZONE COLUMN PRODUCT DERIVED FROM THE SEVIRI 9.7 MICRON CHANNEL

F. Karcher, A. Drouin, L. El Amraoui, V. Ferreira, and A. Pacini,

*Centre National de Recherches Météorologiques, Météo-France and CNRS URA 1357,
42 avenue Coriolis, 31057 Toulouse cedex, France, Email fernand.karcher@meteo.fr*

ABSTRACT

Using operational SEVIRI Level 1.5 production, a set of 50 full disk ozone images taken once per week at 12 UT between February 2004 and January 2005 was produced. The horizontal resolution was reduced near 1 degree to fit the resolution of TOMS and assimilated Sciamachy products that are available on public websites. A first comparison revealed systematic errors as large as 50 D.U. dependent both on latitude and zenith distance of observation.

The error could be interpreted as the result of a biased learning profile data set that was used to calculate the regression equations providing approximate background and foreground temperatures. Using a new climatology built with profiles of ozone, temperature and water vapour extracted from the analyses of ECMWF and the RTTOV fast radiative transfer code provided by the SAF on Numerical Weather Prediction, the systematic errors could be limited in the range (5% to 15%) over the full disk in the latitude range 60S to 60N.

1. INTRODUCTION

With his unprecedented horizontal and temporal resolutions, the SEVIRI 9.7 micron channel provides a novel insight on the atmospheric ozone distribution. Earlier papers (see for instance [1]) have shown the potential interest of SEVIRI total ozone images for severe cyclogenesis prediction in operational weather forecasting. The aim of this paper is to assess the absolute accuracy of the SEVIRI total ozone product. Important applications like calculation of surface UV irradiation and derivation of cross tropopause ozone fluxes are directly dependent of the quantitative ozone measurements that can be obtained with SEVIRI. The work presented here is the start for further comparisons, mainly to be performed for the partial ozone column that is also derived from the 9.7 micron channel, and that will benefit from the comparison routines which have been prepared.

The second section describes the SEVIRI data and the external data that are used as references for the comparisons.

The third section presents the results of the comparisons, for an initial a corrected version of the SEVIRI Total Ozone (STO) algorithm.

The steps of the correction process applied to the algorithm are presented in section 4.

Finally, Section 5 is a discussion of the results and a proposal for further validations and improvements of the STO algorithm.

2. DESCRIPTION OF THE DATA SETS

Since MSG-01 has been positioned at longitude 3.7 degree West and declared operational at the end of January 2004, high resolution total ozone columns can be derived with a temporal frequency of 15 minutes and a sub-satellite resolution of 3 km over more than half an hemisphere (called here the Meteosat disk). Other measurements are however not available at the same resolutions. Due to the high variability observed in [1] on MSG total ozone, we chose to compare the derived total ozone images with results of assimilation experiments now made available with the processing of results of the ENVISAT mission. The good simultaneity that is achieved in such comparing conditions is however subject to the quality of the motion field of the model that is used in the data assimilation process.

The objectives of the comparison are:

- to estimate the systematic bias of the ozone column products derived from SEVIRI,
- to detect possible variations with the zenith angle of observation, with latitude, and more generally as a function of the geographical location on the Meteosat disk,
- to detect seasonal variations of the bias.

In order to validate the SEVIRI retrieval algorithm over the whole disk, we took the option to perform the comparison with global satellite observations and results of assimilation experiments, without any direct comparison with ground based observations.

As no high horizontal resolution ozone data were available, we averaged the MSG columns over areas of 1 degree latitude and 1.5 degree longitude, thus degrading the resolution to that of the Sciamachy assimilation output and compared all data sets on a such grid over the Meteosat disk.

The variations in the diurnal cycle have not been investigated yet, since they would require comparative data at high temporal frequency, only available with results of assimilation experiments and that are not currently distributed. All retrieved ozone columns correspond to the universal time of 12 hours.

The seasonal variations of MSG ozone systematic errors are analysed with a set of 50 images selected over a time interval spanning from February 2004 to January 2005 at the frequency of one image per week.

The MSG pixel ozone columns (also called SEVIRI Total Ozone or STO) are provided with indication of an uncertainty value that is a noise level, and that reflects the random error on each individual measurement due to the radiometric noise of the instrument and to local observing conditions (cloud type). It is called Small Scale Noise (SSN). As we want to cancel possible interferences with such errors and as we focus on clear sky and low cloud conditions, the noisiest STO observations, with a SSN value over 20 Dobson Units were discarded.

Finally, for the purpose of the comparisons, an individual STO original image shown in Fig. 1 is transformed into a longitude-latitude gridded STO image like the one shown in Fig. 2.

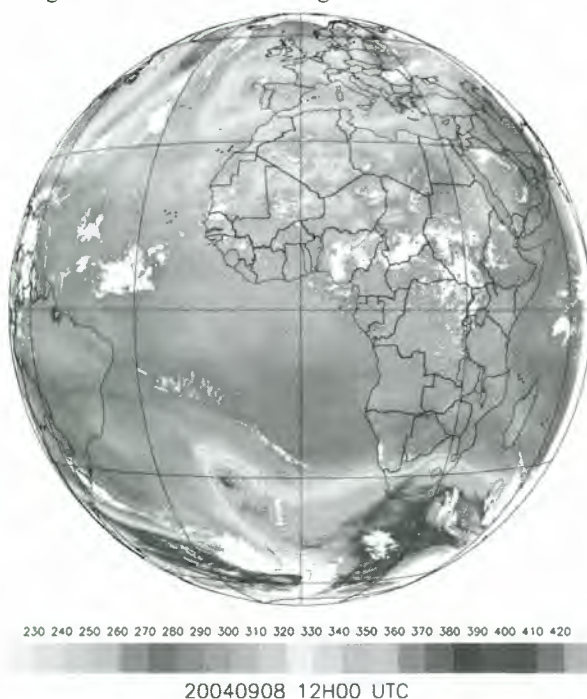


Figure 1: STO product in D.U., version 2 of Apr. 2006, at the original resolution, with SSN<30 D.U.

In addition, the STO algorithm has 2 versions: a first version dated November 2004 corresponding to the results shown in [1], and a second version of April 2006 modified after the first comparison experiment.

The Sciamachy observations are not used directly, since we preferred simultaneous data provided by the assimilation experiment performed at KNMI (The Netherlands Royal Meteorological Institute) with their TM3 Data Assimilation Model TM3DAM. The experiment is described in [2] and the data can be downloaded from the site referenced in [3]. TM3DAM

is a chemistry and transport model that is driven by the meteorological analyses of the European Centre for Medium-Range Weather Forecasts (ECMWF). It has a resolution of $2^\circ \times 3^\circ$ and assimilates near real time total ozone columns derived from the Sciamachy instrument on board ENVISAT. The accuracy of the assimilated Sciamachy data set is better than 3% on average.

Level 3 observations from the Total Ozone Mapping Spectrometer of NASA/Earth Probe satellite were also used for comparisons. These data are put on a grid of $1^\circ \times 1.25^\circ$ and were interpolated onto the common grid used for all observations ($1^\circ \times 1.5^\circ$). These data are not simultaneous with the STO data since the measurement are performed at constant local time close to 11 a. m.. The time difference with other data at 12 UT lays therefore in the interval (-6, 4) hours. Comparisons made for the 50 days selected over years 2004 and 2005 with assimilated Sciamachy data showed however a good agreement and confirm the accuracy of 3%

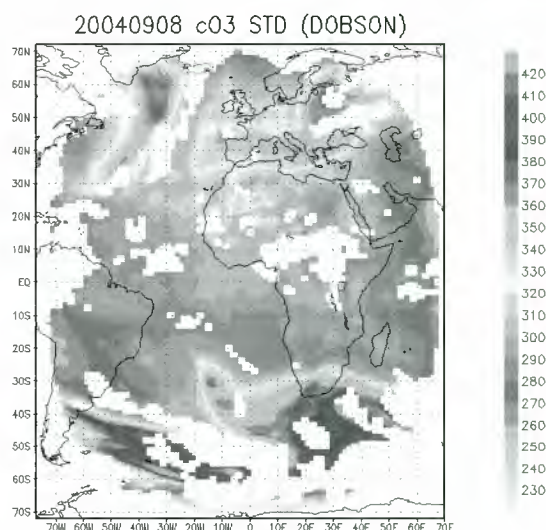


Figure 2: STO product in D.U., version 2 of Apr. 2006, on a $1^\circ \times 1.5^\circ$ lat. x lon. grid, with SSN<20 D.U.

announced for these data (see Figs. 3 and 4 for the average and standard deviations of the relative differences between the two data sets).

Ozone columns were also calculated from the “model level” ozone concentrations provided by the operational analysis of ECMWF. The daily operational forecast assimilates ozone partial columns provided by satellite observations of the instruments TOMS, GOME (Global Ozone Monitoring Experiment on ERS-2), and SBUV (Solar Backscattering of UV on NOAA Polar Orbiting Environmental Satellites). The model has high horizontal resolution (close to 0.5°) and has a linearised ozone chemistry. The ECMWF operational output provides a 3D ozone fields from which our partial column can be compared. This comparison was however not our first priority since the tropospheric

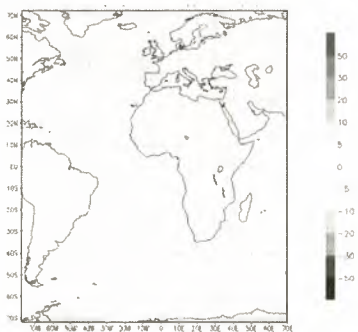


Figure 3: annual average of relative difference between Sciamachy and TOMS in %.

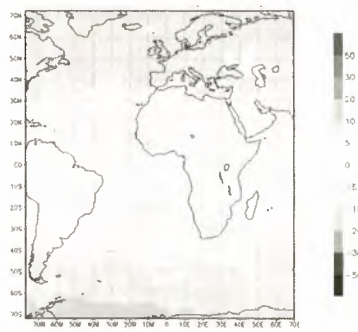


Figure 6: annual standard deviation of relative difference between ECMWF and TOMS in %

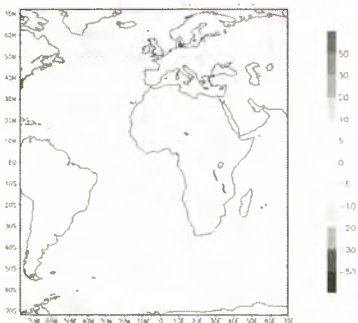


Figure 4: annual standard deviation of relative difference between Sciamachy and TOMS in %

distributions are not taking into account the polluting emissions at the surface. Ozone total columns of ECMWF shows generally an increase with latitude in both hemisphere when compared to TOMS or assimilated Sciamachy data as can be seen in Figs. 5 and 6.

In the rest of this paper, we will only compare our STO product with the output of the Sciamachy assimilation that should be accurate within 3%, with the possible exception of the higher latitude regions.



Figure 5: annual average of relative difference between ECMWF and TOMS in %

3. COMPARISON OF THE SEVIRI PRODUCTS WITH THE SCIAMACHY ASSIMILATED DATA.

Fig. 7 shows a Sciamachy individual ozone map plotted in the same conditions of resolution and with the same ozone column scale as the STO version 2 product of Fig. 2. The relative difference between the 2 ozone maps is shown in Fig. 8 and exhibits a large variability at synoptic scale, rather uniformly distributed over the Meteosat disk. We feel that this variability stems mainly from the different ways these data are produced.

More information can be obtained through the comparisons of the annual average of the relative differences between STO and Sciamachy. The average relative differences of both STO versions with respect to Sciamachy are shown in Figs. 9 and 10.

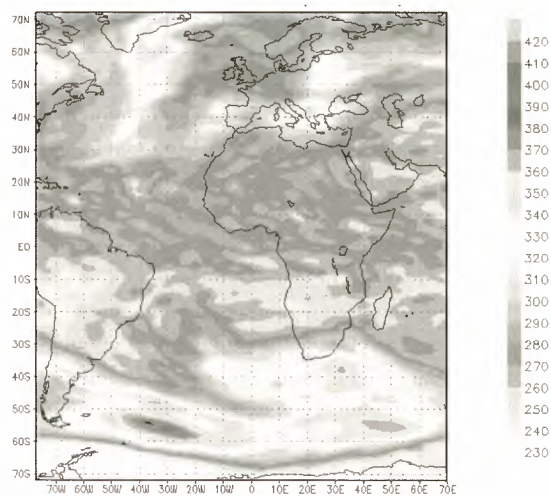


Figure 7: Assimilated Sciamachy total ozone of Sept. 8, 2004, 12 UT plotted in the same conditions as STO in Fig. 2

For the STO version of November 2004 (see Fig. 9), large systematic differences were observed as function of zenith distance of observation, as a function of

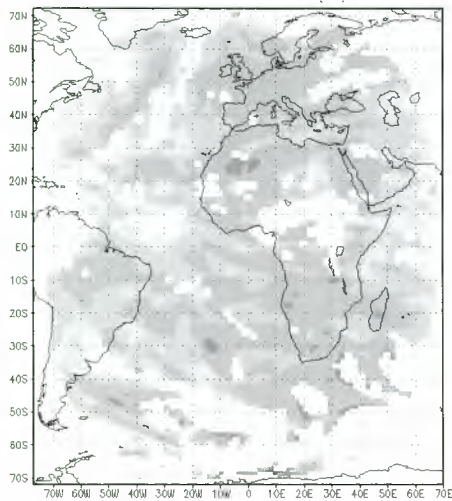


Figure 8: relative difference between ozone maps of STO vers. 2 and Sciamachy for Sept. 8, 2004, 12 UT

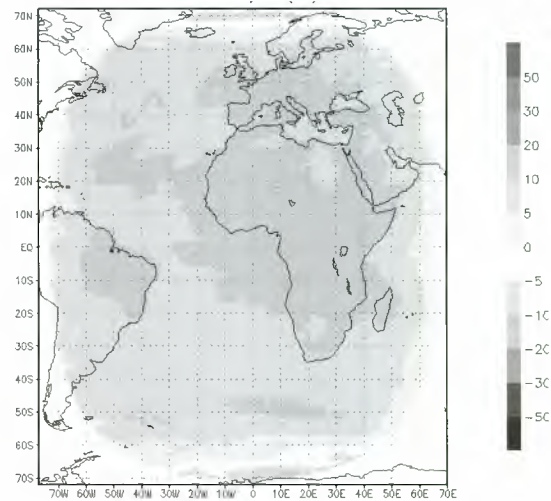


Figure 10: average relative difference between ozone of STO (vers. 2) and Sciamachy (STO-SCI)/SCI in %.

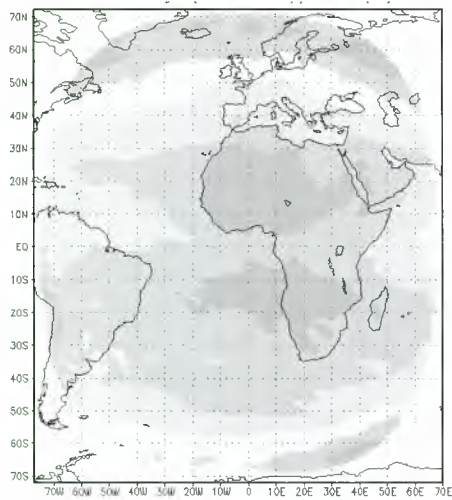


Figure 9: average relative difference between ozone of STO (vers. 1) and Sciamachy (STO-SCI)/SCI

latitude, and as a function of the surface type. The first two dependences could be corrected rather well in version 2 of April 2006 (see Fig. 10). The decrease of STO when moving from the centre to the edge of the Meteosat disk could be removed properly as well as most of the latitudinal variation that was present in both hemispheres between latitudes 40° and 60°. At latitudes above 60N, a decrease still remains in version 2, but one has to keep in mind that:

- the SEVIRI zenith distance is close to, or higher than 70°,
- the Sciamachy observations are less accurate at high latitudes, and that
- the average difference is less than the standard deviation even at these latitudes as can be seen on Fig. 11.

Fig. 11 reveals also an overestimation of STO over land as compared to the sea, especially over the Mediterranean Sea, Africa and Brazil. The origin of the artefact is the land surface emissivity difference in channels 9.7 and 10.8 microns. This effect is not yet corrected in version 2. A correction is being designed on a pixel by pixel basis through an optimisation process that takes advantage of the constant observing zenith angle specific for geostationary satellites.

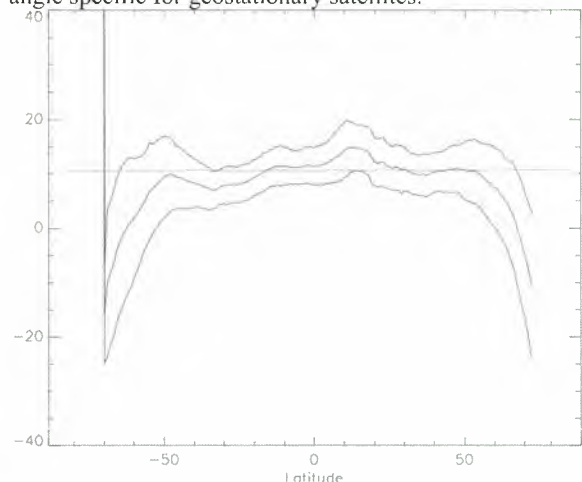


Figure 11: annual latitudinal variation of the relative difference of version 2 (STO-SCI)/SCI computed in % for longitudes between 30W and 30E of the Meteosat disk (central line). The upper and lower curves represent the average ± 1 standard deviation

We can observe in Fig. 11 that the steepest latitudinal variations of the average difference occur most at those latitudes affected by the land sea difference. These differences are indeed at their maximum for our data set at noon, when the surfaces are close to their maximum temperature.

Figs. 12 and 13 show the seasonal variations of the relative differences $(STO-SCI)/SCI$ for versions 1 and 2 of the STO algorithm.

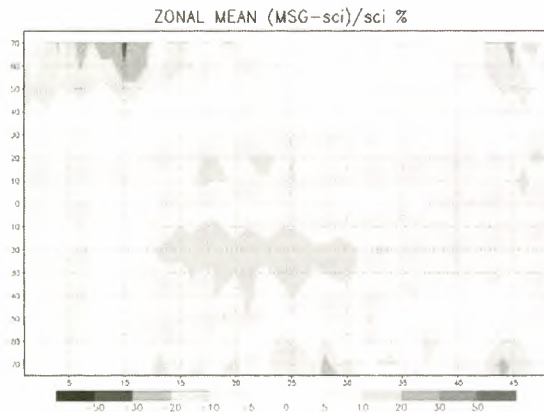


Figure 12: Relative difference (%) of STO (vers. 1) and Sciamachy ozone as zonal averages represented as a function of the week of the year (from Feb. 2004 to Jan. 2005). The scale is the same as in Fig. 10.

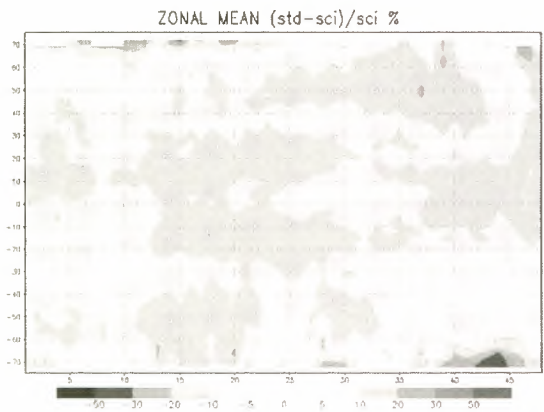


Figure 13: same as Fig. 12 for STO vers. 2.

Fig. 13 shows that, in the latitude interval $(-60, +60)$ degrees, most of the seasonal variations present in version 1 (Fig. 12) could be removed. Like in Figs 9 and 10, the land sea artefact is also included in this seasonal display and contributes slightly to enhance the STO product at tropical latitudes in spring and summer.

4. CHANGES OF THE STO ALGORITHM FOR VERSION 2

The physical principle of the STO algorithm, which consists in deriving the stratospheric transmittance τ in channel 9.7 microns prior to the determination of ozone columns has not been changed from version 1 of November 2004 to version 2 of April 2006. Its calculation from Eq. 1:

$$\tau = (R_9 - B_9(T_F)) / (B_9(T_B) - B_9(T_F)) \quad (1)$$

was not changed, but the regression equations providing the foreground and background temperatures T_F and T_B were changed. Likewise, the regression equations providing the total ozone column and the partial ozone column from the transmittance τ were also changed. The regression equations use mainly SEVIRI brightness temperatures (see [4]) as predictors and are determined from a learning data set of brightness temperatures, foreground and background temperatures, transmittances calculated with a radiative transfer code from a set of atmospheric profiles and surface conditions.

The atmospheric profile data set used earlier was gathered at 22 radiosonde stations, at various latitudes covering the whole latitude range. This process introduced a random bias with latitude because each station has its own climatology which is different from the climatology of the zonal average at the same latitude. For the new version, we used a set of profiles of temperature, water vapour and ozone extracted from the ECMWF operational analyses, covering the whole Meteosat disk, at 8 days of the year 2004, and at 4 times in each day in order to get a high variability in the atmospheric conditions at a given latitude together with a high consistency in the latitude dependences as well as for the 3 parameters of each profile: temperature, water vapour and ozone.

For the radiative transfer calculations, we used the RTTOV 8.7 code of the Satellite Application Facility for Numerical Weather Prediction. We checked that this code produced regression equations very similar to those of calculated earlier with FASCOD-3 (see details in [4]) when using the radiosonde profiles dataset.

For the zenith angle dependence, we corrected first an inappropriate sampling of the zenith distance in the synthetic radiance data set used for the calculation of the regressions. In the initial data set, the radiances for each profile were calculated for 6 discrete values at $\zeta = 0, 14, 28, 42, 58, 80$ degree. In the new version, the set of model profiles extracted from the ECMWF archive was associated to its exact zenith distance on the Meteosat disk and the sampling of these profiles appears on Fig. 15. This method produces a much larger amount of different zenith angles ranging from 0 to 80 degrees. Secondly, the zenith angle dependence used in the regression equations was changed from a function of $\zeta, \cos\zeta, \sin\zeta, \cos2\zeta$ to a function of $\cos\zeta, \sin\zeta, \cos2\zeta, \sin2\zeta, \cos3\zeta, \sin3\zeta$ which introduces more high frequencies in the truncated Fourier series representation of this function. In order to test the validity of the zenith distance variations of each of the regressed quantities $\tau, T_F,$ and $T_B,$ a regression equation using the new type of function was calculated with a profile data set corresponding to a given disk study case (see Fig. 14 for a real distribution of foreground temperatures) and immediately applied on the same profile data set. We could observe the difference

between true and regressed quantities (Fig. 15). As no major differences appear in any region of the disk, we can be confident that the zenith angle dependence is correctly fitted in the new version of the STO algorithm.



Figure 14: Synthetic foreground temperature (K) calculated for March 31, 2004

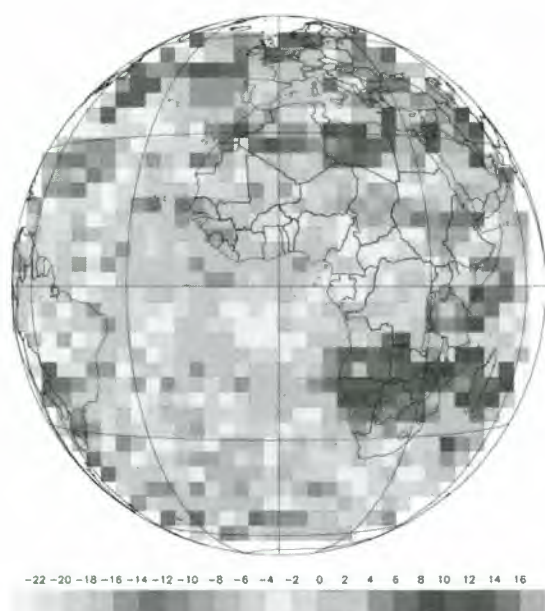


Figure 15: Difference between regressed and true foreground T (0.1 K) for the case of March 31, 2004 for which a regression equation was calculated.

5. Discussion

A study on the systematic errors of the SEVIRI Total Ozone product has been conducted by the means of comparisons, over a complete year, with assimilated Sciamachy ozone columns. The quality of the reference data set has been controlled through comparisons with TOMS observations. The comparison has revealed systematic errors that are dependent with zenith angle of observation, with latitude and with surface type (land or sea). The first two dependences could be corrected by an improvement of the regression equations used to derive the foreground and background temperatures and the total ozone product. The dependence with surface type is being corrected with other methods not described in this paper.

The result of the evaluation of the corrected algorithm is that STO overestimates quite uniformly the total ozone column by 10% when compared to the assimilated Sciamachy data. This overestimate is roughly constant with latitude, zenith angle and with the season of the year. It reflects the overestimation of the ECMWF total ozone compared to the Sciamachy assimilation because ECMWF extracted ozone column were used for the learning process of the regression equation used to derive the ozone column from the transmittance in channel 9.7. The improvement performed on the SEVIRI Total Ozone algorithm opens the way for more accurate estimation of surface UV radiation and for the estimation of cross tropopause ozone fluxes. They will also help for a more accurate correction of surface emissivity effects.

6. References

1. Drouin A., and F. Karcher, High resolution ozone column derived from SEVIRI 9.7 ozone channel, Proceedings of the Second MSG RAO Workshop, Salzburg, 9-10 September 2004, ESA SP-???, December 2004.
2. Eskes H. J., R. J. van de A, E. J. Brinksma, J. P. Veefkind, J. F. de Haan, and P. J. M. Valks, Retrieval and validation of ozone columns derived from measurements of SCIAMACHY on Envisat, *Atmos. Chem. Phys.*, 0000, 0001-15, 2005.
3. Tropospheric Emission Monitoring Internet Service (TEMIS), <http://www.temis.nl/protocols/O3global.html>
4. F. Karcher, Y. J. Orsolini, J.-P. Meyer, S. Muller, P. Armand, D. Blaison, H. Kelder, M. Allaart, and V. Pultau, Study on the exploitation of the ozone channel on MSG for the extraction of wind information, Eumetsat contract EUM/CO/96/439/MPe, 1998.

MODELING NATURAL SURFACE UV RADIATION WITH METEOSAT AND MSG

Jean Verdebout

*European Commission - Joint Research Centre - Institute for Health and Consumer Protection
Via E. Fermi, 21020 Ispra (VA), Italy, Email: jean.verdebout@jrc.it*

ABSTRACT

The method for mapping surface UV radiation using MSG follows the general scheme previously used with METEOSAT, with the additional use of the 1.6 μm band for a better snow/cloud discrimination. This adaptation and improvement of the algorithm allows the continuation of the climatological dataset of UV radiation over Europe, covering the period from 1984 to present. A near-real time version of the processor has also been devised to produce UV index maps within a few minutes of the MSG image reception via Eumetcast. MSG data are also used in a human UV exposure model that takes into account the actual activity schedule of a person. In this case, the surface radiance field is modelled in order to estimate the exposure of various parts of the body.

1. INTRODUCTION

Exposure to high levels of UV radiation is harmful to human health (skin cancer, cataract, immunosuppression), and influences many natural biological processes (marine life, plant physiology). Inversely, a sufficient exposure is necessary to avoid vitamin D deficiency. The awareness of these effects has been raised by ozone depletion, which leads to an increase in the intensity of the UV radiation reaching the Earth surface in some regions of the world. It is now felt important to monitor the changes that occur in this environmental parameter. Although the ground radiometers will remain the reference in terms of accuracy, they are too few to offer a comprehensive geographical coverage. Hence the development of methods those aim at mapping the surface UV radiation intensity by combining modelling and satellite data.

The method presented here is using the full resolution images from EUMETSAT's geostationary meteorological satellites. Over Europe, the spatial resolution is typically 5 km (degrading at high latitudes because of the increasing viewing angle). Both instantaneous dose rate and daily dose maps can be generated. The modelling has also been adapted to estimate the human exposure, taking into account behavioural data and the body geometry.

2. METHOD FOR MAPPING IRRADIANCE

It basically consists in using a standard radiative transfer code (UVspec) [1] and in exploiting various sources of information for assigning values to the parameters influencing the surface UV radiation. MVIRI/SEVIRI data are used to derive cloud optical thickness (COT) and to detect the presence of snow. The algorithm uses the visible and infrared bands of MVIRI or the 0.6 μm , 1.6 μm and 12 μm bands of SEVIRI. The NIR band of SEVIRI provides an additional discriminator between snow and clouds.

The mapping methodology is described in detail elsewhere [2, 3]. To summarize, UV radiation maps over Europe are generated with a spatial resolution of 0.05 deg.. The surface UV dose rate is obtained by interpolation in a look up table (LUT) of modelled irradiance, the entries of which are solar zenith angle, total column ozone amount, cloud optical thickness (COT), near surface horizontal visibility, surface elevation and UV albedo. The LUT was computed with the UVspec code of the libRadtran package. Both satellite and non-satellite (synoptic observations, digital elevation model) data are exploited to assign values to the influencing factors. The total column ozone is extracted from the gridded TOMS data or other ozone sensors data (e.g. NNORSY-TOVS [4], GOME). The aerosol optical thickness is tentatively taken into account by gridding daily measurements of near surface horizontal visibility performed by about 1,000 ground stations. The digital elevation model is the GTOPO30 data set from United States Geological Survey (USGS).

With the help of another LUT simulating the "at sensor radiance" (proportional to the image digital count in the visible band), METEOSAT data are processed to retrieve the cloud optical thickness. The entries of this second LUT are solar zenith angle, METEOSAT viewing zenith angle, relative azimuth between illumination and viewing vectors, effective surface albedo and cloud optical thickness. A preliminary step consists in generating an effective surface METEOSAT albedo map by finding cloud free pixels in a series of ten consecutive days. In most cases, the cloudless pixel is chosen as the one corresponding to the lowest signal in the visible band. However, if the surface reflectance is high, the surface may be snow covered and the

darkest visible signal does not necessarily indicate the absence of clouds. Therefore, if the effective surface reflectance is found to be above a certain threshold, the discrimination is refined by also using the thermal infrared band. The rationale for this second algorithm is that the pixel brightness temperature should be higher when cloud free than when cloud covered, even if snow is present. However, a threshold for discrimination can only be defined locally as the surface temperature varies considerably with geographical location. The land surface was therefore divided in zones according to latitude and geophysical characteristics. In particular, the main mountainous areas (the Alps, the Pyrenees, the Caledonian range in Scandinavia) constitute such zones. In mountain areas, the zone is further subdivided in altitude classes. For each class, the histogram of the infrared METEOSAT brightness temperature over ten days is fitted as a sum of Gaussian functions. The cloud free pixels are associated with the "warmest" Gaussian and a threshold is determined on this basis.

When using SEVIRI, an additional criterion for distinguishing snow from clouds was introduced, using the NIR band at 1.6 μm . In this band, snow and ice appear darker than water clouds. In order to reject ice clouds pixels (dark in NIR but cold) as candidates for snow, a discriminator was built, dividing the brightness temperature (in K) by the digital count in the NIR band. It was then assumed that snow corresponds to the highest values of this discriminator. The same algorithm as for the brightness temperature, based on a multi-Gaussian fit of the histogram, was used to determine a threshold.

Once the composite cloudless digital count image has been constructed, it is transformed in an effective albedo map by inversion, using the LUT reduced to the cloudless case. The effective albedo map is then used to estimate the cloud optical thickness for the day and time of interest, by inversion using the full LUT. The UV surface albedo is assigned uniform values for land (0.03) and sea/ocean (0.06), except in the presence of snow. In this case it is given a value proportional to the METEOSAT effective albedo. The rationale for proportionality between the albedos in the two spectral ranges is that partial snow cover should affect them in a similar way. The outputs of the METEOSAT processing are fed into the UV map processor to generate surface UV irradiance maps or dose rate maps when a spectral weight is applied.

The daily dose is constructed by numerical integration of the dose rate estimated at half-hourly intervals from and including the local solar noon (for each pixel). The COT time dependence is described with a stepwise

function with as many time intervals as the number of images used per day.

3. CLIMATOLOGICAL UV DATA SET

With the method outlined above, it has been undertaken to build a European climatology of UV radiation. As of today it consists in daily dose maps from January 1st 1984 to present. For practical reasons (processing time and amount of data) one image per day only has initially been used. The data set is progressively upgraded to using 3 images per day; this is already the case for March and July from 1990. Although only erythemal doses are shown here, the model output is spectral and the dose corresponding to any desired action spectrum can be generated on request.

These data are available from JRC for scientific purpose (e.g. impact studies). Fig. 1 shows an example of how the data set documents the year-to-year variability of the surface UV radiation over Europe. Extracts of this data set have been used in the European project UVAC (UV and Arctic Cod), which studied the influence of the natural UV radiation variability on the annual population strength of the North East Atlantic cod. Data have also been provided to a number of external users, for ecological impact studies (e.g. on frogs in mountain lakes), for assessing the effect of UV on crop yield, for completing a data set on the UV exposure of schoolchildren, for supporting assessments of vitamin D deficiency and for local climate studies.

4. NEAR REAL TIME UV INDEX MAPS

The algorithm was slightly modified to generate the erythemal radiation maps within a few minutes of the SEVIRI data reception via Eumetcast. The main change was to substitute the daily data of visibility (aerosols) and total column ozone by climatological averages. The daily data for these two parameters are indeed not available in near-real time. Also the UV index scale was used, obtained by dividing the erythemal dose rate expressed in mW/m^2 by a factor 40. The UV index was defined by WMO as a mean of communicating the UV radiation strength to the public in a more readable way; over Europe the UV index takes values between 0 and ~ 10 . Fig. 2 shows the comparison with measurements of the instantaneous UV index in Innsbruck. Fig. 3 shows an example of a daily UV index map over Europe (maximum value during the day).

DEVIATION OF THE MONTHLY AVERAGED ERYTHEMAL DAILY DOSE WITH RESPECT TO THE 1984–2005 MEAN (MARCH)

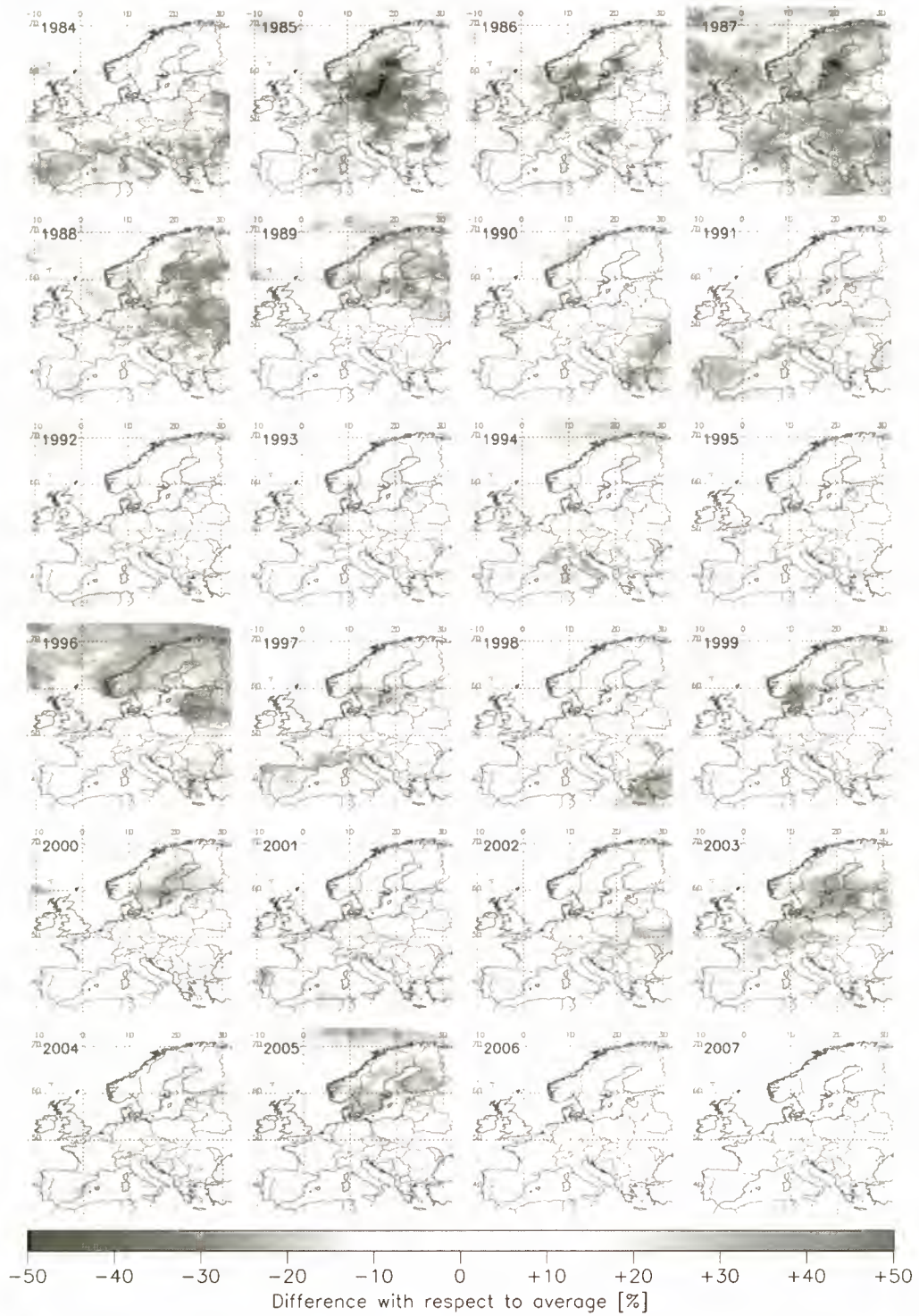


Figure 1. Year to year variability of the monthly averaged erythemal daily dose in March.

A version of this near-real time processor has been installed at the Medical University of Innsbruck, where the UV index map of Austria is operationally produced and published on the web (<http://www.uibk.ac.at/projects/uv-index>). In this particular case, the software does not provide the UV index directly but a cloud attenuation factor that has been integrated in the previous processor at Innsbruck. This last one is using the measurements from the Austrian UV network [5] and takes better into account the altitude (with a higher spatial resolution than the MSG images). The result are UV index maps that show both the spatial details of the clouds and the mountains and that are anchored to measurements. Recently, the software has also been installed at the Aristoteles University of Thessaloniki in view of producing UV index maps for Greece.

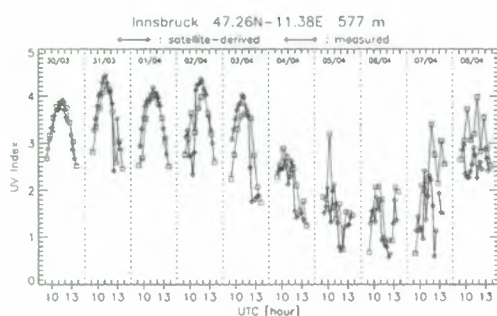


Figure 2. Comparison of measured and modelled UV index values at Innsbruck

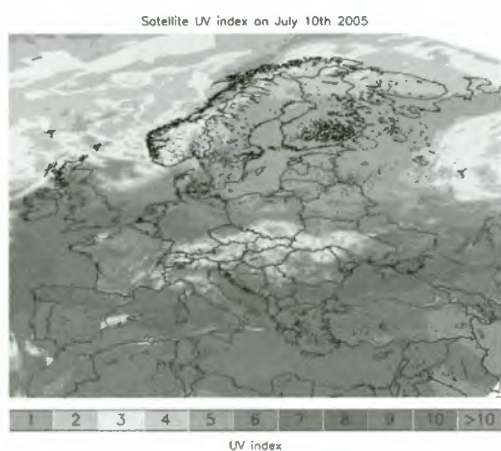


Figure 3. UV index map on July 10th 2005

5. HUMAN EXPOSURE MODEL

Modelling the “erythemal risk” of an individual or of a population requires much more than the intensity of the natural UV radiation. Such a model must take into account behavioural data, in particular activities, their schedule and location. Another very important variable is the un-equal sensitivity of individuals’ skins to the same exposure.

The first objective of the model is to estimate a realistic UV exposure of a person’s body starting from behavioural information, including location, activity and clothing. The first step is to compute the physical UV radiation field at the location of the person. This calculation takes into account the various physical factors influencing the UV radiation intensity (solar zenith angle, ozone column, cloudiness, aerosols, surface albedo and altitude). The output of this calculation is the erythemal UV radiance field (both direct and diffuse). The values attributed to the physical influencing parameters can be set according to a scenario, from local measurements and/or be extracted from MSG images, which allows taking into account the geographical variability of the radiation. As the radiance calculation needs to be performed many times (e.g. every 15 minutes within the exposure time windows of the person) only a plane-parallel radiative transfer model is practicable (due to CPU time). Such a model cannot take into account the local environment (buildings, trees, local topography). In a later stage, it is conceivable to build a database of local environment correction factors (to be applied to the radiance field) by using a 3-dimensional radiative transfer models. In the first version of the exposure model, the local environment corrections will be introduced as reduction factors directly on the exposure. A number of such reduction factors can be found in the literature, usually obtained from experimental work. Fig. 4 shows three different radiance fields as computed with the UVspec code.

Having the radiance field, the exposure of an arbitrarily oriented surface can be computed. A very simple example is to select three orientations: horizontal, vertical and 45 degrees. As a very first approximation, they may be representative of the shoulders, face and nose of a person in an upright position. Exposure of different parts of the body can then be estimated as weighed averages on the orientation, which are dependent on the activity (e.g. standing when walking or running, lying when sun tanning on a beach, etc.). At this stage reduction factors corresponding to clothing or the use of sun creams can be taken into account.

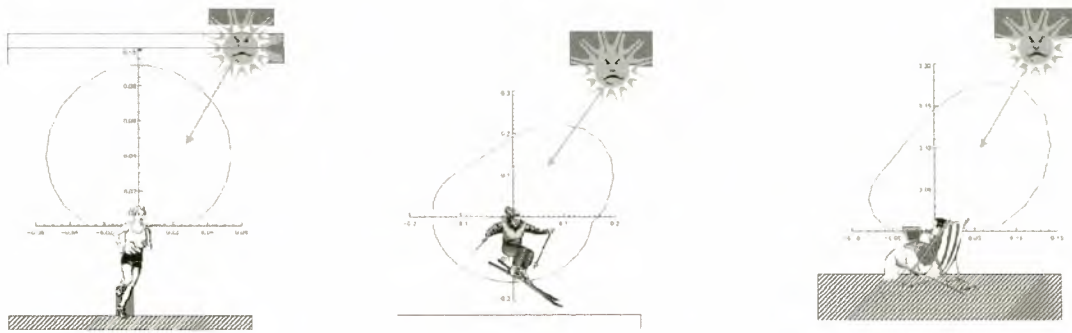


Figure 4. radiance fields as computed with UVspec for (from left to right): low surface albedo and cloudy conditions, high albedo (snow) and clear sky conditions and low albedo – clear sky conditions.

As an example, Fig. 5 shows the potential daily face exposure of a hypothetical office worker living in Düsseldorf. On working days, he is exposed on his way to and from the office and when he is jogging at lunchtime. He is more strongly exposed during the week-ends as a result of outdoor activities (sport, gardening). He is also spending a week skiing in Kitzbühel in March and having a two weeks holiday period on a Greek island (Rhodes) in August. The exposure is expressed in MEDs (Minimal Erythral Dose) for a skin type II (typical of a northern European). The MED is the dose, which if exceeded will produce an erythema. The main conclusion would be that the office worker in Düsseldorf has practically no risk of erythema in his daily life; the risk exists only during holidays. One can also notice that the holiday periods, even if short, account for about half of the total yearly exposure.

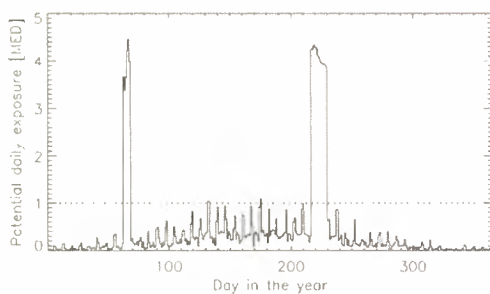


Figure 5. Potential daily face exposure (in MEDs) of a hypothetical office worker living in Düsseldorf

These results are very difficult to validate. Comparison with dosimetry measurements performed by positioning polysulphone films on mannequins (Fig. 6) for various periods and meteorological conditions have nevertheless

shown that the model succeeds in catching the variability of the exposure of various parts of the body (Fig. 7).



Figure 6. Dosimetry measurements on mannequins

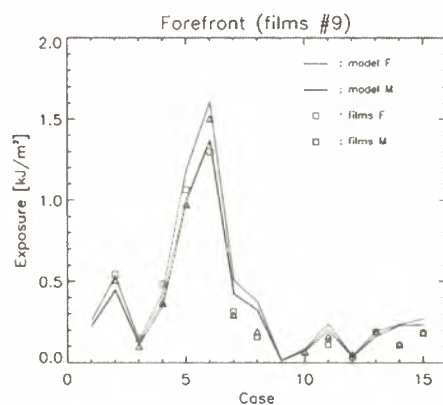


Figure 7. comparison of measured and modelled doses on the forehead (the cases correspond to various exposure times in various meteorological conditions)

6. CONCLUSION

MSG is allowing continuing the climatological dataset of UV radiation over Europe that had been undertaken with METEOSAT 2 to 7. These data have been and are used for impact studies in various fields. With the higher temporal frequency of the images and tanks to the near-real time reception via Eumetcast it has also enabled other practical applications such as near-real time UV index maps and human exposure modelling taking into account the activity schedule of a person.

7. ACKNOWLEDGMENTS

The author wishes to thank EUMETSAT for providing the many METEOSAT images used in this work and the set of MSG data (in the framework of RAO project 160).

8. REFERENCES

1. Mayer, B and Kylling A, Technical note: The libRadtran software package for radiative transfer calculations - description and examples of use, *Atmos. Chem. Phys.*, 5, 1855-1877, 2005.
2. Verdebout, J., A method to generate surface UV radiation maps over Europe using GOME, Meteosat, and ancillary geophysical data, *J. Geophys. Res.*, 105, 5049-5058, 2000.
3. Verdebout J. and Gröbner J., Mapping natural surface UV radiation with MSG: maps series in spring 2004, comparison with METEOSAT-derived results and reference measurements, *Proc. Second MSG RAO Workshop*, Salzburg, Austria, 9-10 September 2004, ESA SP-582, 51-56, 2004.
4. Kaifel, A. K. and Müller M. D., Results of TOVS ozone retrieval with neural networks, in: J. Le Marshall and J. D. Jasper (Eds.), *Techn. Proc. 11th Int. ATOVS Study Conference*, Budapest, Hungary, 20-26 September 2000, 153-165, International ATOVS Working Group, Bureau of Meteorology Research Centre, Melbourne, Australia, 2001.
5. Blumthaler M., Quality assurance and quality control methodologies used within the Austrian UV monitoring network, *Radiation Protection Dosimetry*, vol. 111, No 4., 359-362, 2004.

NET AIR-SEA FLUX ESTIMATES FOR THE TROPICAL AND SUBTROPICAL ATLANTIC OCEAN BASED ON SATELLITE DATA

Kristina B. Katsaros⁽¹⁾, Rachel T. Pinker⁽²⁾, Abderrahim Bentamy⁽³⁾, James A. Carton⁽²⁾,
William M. Drennan⁽¹⁾, and Alberto M. Mestas-Nuñez⁽⁴⁾

⁽¹⁾University of Miami, Department of Applied Physics, 4600 Rickenbacker Causeway, Miami, FL 33149 USA

⁽²⁾University of Maryland, Department of Atmospheric and Oceanic Science, College Park, MD 20742 USA

⁽³⁾Institut Français de Recherche pour l'Exploitation de la Mer, B.P. 70, 29280, Plouzane, France

⁽⁴⁾Texas A&M University, College of Science and Technology, 6300 Ocean Drive, Corpus Christi, TX 78412 USA

ABSTRACT

The objective of our work is to estimate the net heat exchange across the air-sea interface in the tropical and subtropical Atlantic Ocean using mainly satellite data. The net flux and the various terms will be used to study the processes in the upper ocean related to changes in sea surface temperature (SST). This variable influences atmospheric circulations and is indicative of upper ocean circulations in this area. We employ data from METEOSAT-7 and 8 and from the Special Sensor Microwave/Imager (SSM/I) for the shortwave and long-wave radiative fluxes and for estimates of SST. For turbulent flux calculations, we use the bulk aerodynamic method with satellite estimates for wind speed and atmospheric humidity and temperature. We expect our work to shed light on rainfall regimes in Africa and South America and on the changes and slope of the tropical thermocline structure in the Atlantic Ocean.

1. BACKGROUND

Climate variability associated with phenomena such as frequency of hurricanes, precipitation in western Africa and northeastern Brazil, results from interactions between the atmosphere and oceans. From the atmosphere's perspective, this exchange is reflected in varying SSTs. It is, therefore, important to look at the sources of the Tropical Atlantic Variability (TAV), as discussed in [1]. The relevance of TAV to climatic variability can be illustrated by considering the leading empirical mode of North Atlantic SST anomaly variability [2]. This mode shows large amplitudes over the tropical (and extra-tropical) North Atlantic and is dominated by multi-decadal time scales. On these long time scales, the North Atlantic mode is associated with changes in tropical Atlantic hurricane activity [3]. On shorter interannual-to-decadal time scales, the relevant factor behind TAV is the SST meridional gradient. In the west, it affects the West African Monsoon (WAM). In the east, the SST gradients influence atmospheric circulation, leading to increased wind speeds and a shift in the location of the Inter-Tropical Convergence Zone (ITCZ), thereby affecting precipitation in the Nordeste province of Brazil [4,5]. SST anomalies in this

region appear to be very closely coupled to surface heat flux variations [6,7,8]. Since the key environmental variable for Atlantic climate is SST, understanding the surface heat fluxes which force the observed SST variability is at the heart of Atlantic climate research.

The Atlantic Ocean provides a very good test region for attempting to sum all the flux terms and arrive at a reasonable net flux, because there are surface buoys in the tropical region, research vessels, and many volunteer observing ships to provide in situ data for anchoring the satellite estimates. The separate terms and the net can be tested independently by using the satellite-derived fluxes with an upper ocean reanalysis model (e.g., the Simple Ocean Data Assimilation (SODA) model [9]) to compare with forcing provided by atmospheric reanalysis models. The satellite net flux estimates can be also evaluated by comparison with the net gain or loss of heat by the ocean in certain regions to altimetric estimates of the sea surface height change over time.

Our period of study overlaps the African Multidisciplinary Monsoon Analysis (AMMA), which has Special Observing Periods scheduled in 2006 with a research vessel, the *Ronald H. Brown*, stationed in a region west of Africa. Patterns of SST and their variability in time and space will be investigated in relationship to the West African Monsoon and its variability.

We aim to evaluate accurately all the following terms in the air-sea energy exchange for the period 1992-2006.

$$H_{\text{net}} = \text{SW up} + \text{SW down} + \text{LW up} + \text{LW down} + \text{LHF} + \text{SHF} \quad (1)$$

where H_{net} is the net energy budget, with a positive value indicating loss from the ocean, i.e., vertical coordinate positive upwards; SW refers to solar radiation at the air-sea interface directed up or down; LW is the surface logwave radiation, 3-50 μm , directed up or down; LHF is latent heat flux due to evaporation; and SHF is sensible heat flux.

In section 2 we describe the methods and data used for the radiative transfer calculations, which are central to the METEOSAT-8 work. In section 3 we briefly describe the

methods and data used for the turbulent fluxes of heat and water vapor [10]. Section 4 presents the evaluation of the accuracy of the fluxes, and section 5 presents examples of the fields we are producing with some discussion. Section 6 gives a short summary and presents the plans for completing the collection of all the variables needed to force an ocean circulation model independent of atmospheric numerical models.

2. METHODS FOR RADIATIVE FLUXES

A key role in the budget is played by the radiative fluxes. Under the International Satellite Cloud Climatology Project (ISCCP), e.g., [11], time series of cloud cover were produced, as well as surface radiative flux estimates at 2.5° resolution and 3-hourly time scale and are available for a period of about 20 years [12,13]. The temporal variability of clouds has a strong effect on the estimated surface fluxes, and the low spatial resolution of ISCCP, therefore, limits use of its data in smaller scale studies. The recent observations from METEOSAT-8 developed by the European Space Agency (ESA) and the European Organization for the Exploitation of Meteorological Satellites (EUMETSAT) [14,15] are well suited to improve estimates of radiative fluxes. Our strategy to obtain long term information on radiative fluxes is: evaluation of SW radiative fluxes as available for longer time periods from geostationary platforms against the improved METEOSAT-8 observations during periods of overlap, so the inaccuracies in the longer time series can be estimated; development of an approach to derive long-wave fluxes; and development of capabilities to account for the radiative effects of aerosols. The SW radiative fluxes to be evaluated against METEOSAT-8 are based both on the ISCCP DX data gridded at 0.5° resolution and the high resolution METEOSAT-7 (Fig. 1).

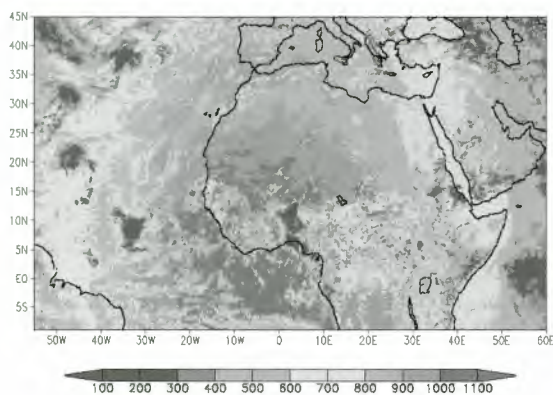


Figure 1. METEOSAT-7 SW downward flux (Wm^{-2}) for Sept. 5, 12 UTC.

In the original version of the University of Maryland Surface Radiation Budget (UMD/SRB) algorithm [13], cloud information is derived from the relevant visible

channel and used to infer surface SW fluxes. A modified version of this algorithm allows for the use of independent information on clouds and aerosols. Such a version [16] was used to derive SW fluxes from METEOSAT-8. The cloud information was derived independently (R. Hollmann, private comm.). A preliminary comparison between METEOSAT-7 and 8 over part of the Atlantic is shown in Fig. 2.

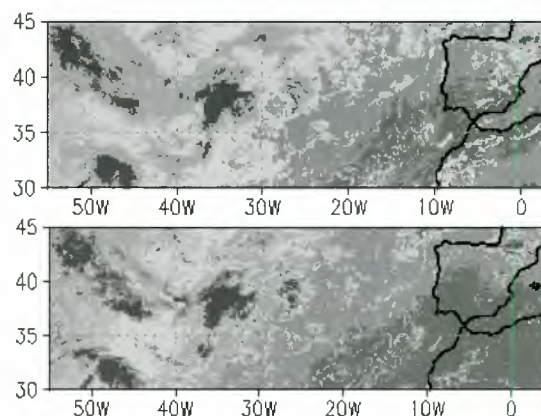


Figure 2. Initial comparison of SW fluxes from METEOSAT-7 (upper panel) and 8 (lower panel) for Sept. 5, 12 UTC.

Observations from METEOSAT-8 are well suited to improve estimates of surface radiative fluxes and can serve as a calibrator of longer time series and as a precursor of the next generation of U.S. geostationary satellites, GOES-R. Only recently, large scale information on aerosol properties is becoming available [17,18]. Over oceans, aerosol information is available from several sources, e.g., the Goddard Institute for Space Studies (GISS), the Moderate Resolution Imaging Spectroradiometer (MODIS), from chemical transport models (COGART), and from amalgamation of satellite products, chemical transport models, and observations (e.g., AERONET). We have improved our surface radiative flux retrieval methodology by incorporating a representation of aerosol optical properties [19].

SST is an important factor in determining the net heat fluxes at the sea surface; it enters into the calculation of the net long wave radiation and the turbulent fluxes of both sensible and latent heat. Errors in satellite SST have been identified as major contributors to errors in the flux fields. Algorithms to estimate SST from Spinning Enhanced Visible and Infra-Red Imager (SEVIRI) observations have been developed [20], implemented, and partially evaluated. An example of SST over the Atlantic as derived from the SEVIRI four channel algorithm is shown in Fig. 3. Several methods have been implemented to derive downwelling LW. We used the approach of [21] implemented with the brightness temperatures of SSM/I microwave channels (as provided by R. Ferraro, private comm.). (See the lower

panel of Fig. 5 in section 4, where an example of LW flux is presented.) Eventually, the derived fluxes will be compared against independent sources of such information (e.g., as produced by the Simulation, Analysis and Forecasting Center) [22].

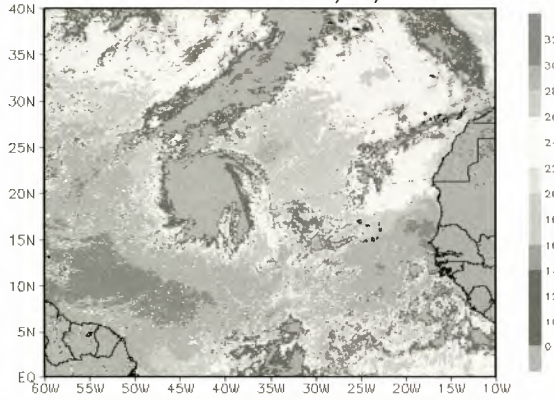


Figure 3. SST from the SEVIRI-4 channel algorithm for September 27, 2004.

3. METHODS AND DATA USED FOR TURBULENT FLUXES

The two energy budget terms, LHF and SHF, are obtained from the bulk aerodynamic formulas of [23]:

$$\text{LHF} = -\rho \cdot L \cdot C_E (U_a - U_0) (q_a - q_s) \quad (2)$$

where U_a is the mean wind speed at 10 m height and U_0 is the current speed at the sea surface, usually set to zero; q_s is the saturation vapor pressure at the sea surface, corrected for salt effects, and simply a function of SST; q_a is the atmospheric humidity at the reference height, 10 m; C_E is the exchange coefficient for water vapor; and L is latent heat of evaporation. C_E is the exchange coefficient calculated from [24].

SHF has a similar equation:

$$\text{SHF} = -\rho C_p C_H (U_a - U_0) (T_a - T_s) \quad (3)$$

where T_s is SST; T_a is the air temperature at 10 m height; C_p is the specific heat at constant pressure; ρ is air density; and C_H is the exchange coefficient for sensible heat.

Turbulent exchange coefficients are crucial for the calculations of the turbulent fluxes, namely the Dalton number, C_E , and the Stanton number, C_H , which we set equal to C_E . The most recent summary of work on C_E in the past 25 years is found in Fig. 4 after [25].

Estimates of the surface wind are a product of merged data of vector winds from scatterometers including those on European Remote Sensing satellites 1 and 2 (ERS 1 and 2),

the NASA scatterometer (NSCAT), and Quikscat with wind speed estimates from microwave radiometers. Estimates of the humidity difference between the air-sea interface and the atmosphere are made using SSTs to obtain q_s . The term q_a is proportional to the column integrated water vapor, obtained from the SSM/I in the U.S. Defense Meteorological Satellite Program [26,27,28]. The protocol for the flux calculations is the one developed by the satellite group at the Institut Francais de Recherche pour l'Exploitation de la Mer (IFREMER), [10].

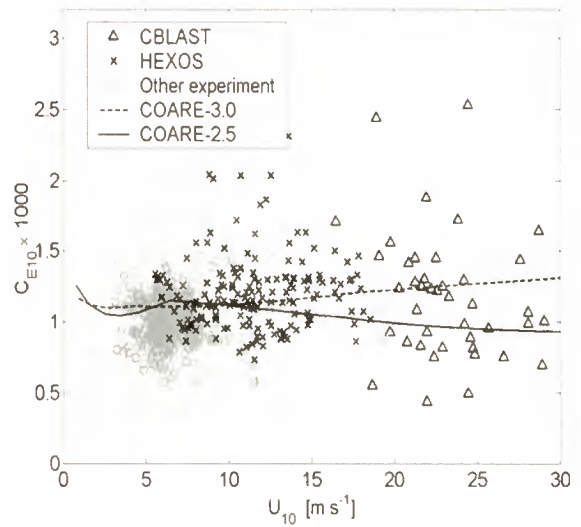


Figure 4. Dalton number at high winds are recent results from [25] obtained from aircraft in the CBLAST program plotted together with the HEXOS program fit from [29]. The symbols represent various experiments (details are not repeated here).

The sensible heat flux calculation using Eq. 3 requires that one obtain the atmospheric air temperature T_a at a reference height of 10 m from space. As proposed by [30], T_a can be estimated using the Bowen ratio, which is defined by:

$$\beta = \frac{C_p C_H (T_s - T_a)}{L C_c (q_s - q_a)} \quad (4)$$

where β is the Bowen ratio; the other variables are defined above. The method assumes a constant value for the Bowen ratio which is an approximation that is quite good in the tropics, where the value is close to the chosen value, 0.1. Eventually, some other method may be found for SHF, or atmospheric numerical models at high resolution and with data assimilation may increase in accuracy beyond what this method offers. (See work by [31], who attempt this idea.) Since SHF is typically a small term in the tropics, our approximate method is not a serious handicap for our objectives.

We plan to calculate a time series of all the energy flux terms for the period 1992 through 2006. However, the accuracy will be somewhat variable over that time span. In order to minimize uncertainties and still retain the interesting spatial and temporal variability, we focus on weekly averages and $0.5\text{-}1.0^\circ$ resolution in the gridded flux fields. We expect this to be an adequate time resolution for the ongoing ocean modeling work. At the minimum, it will provide the required check for biases in flux products of the atmospheric reanalysis.

4. EVALUATION OF THE SURFACE FLUXES

Individual terms in the surface energy budget will be checked against fluxes calculated from mean meteorological measurements at buoy sites of the Pilot Research moored Array in the Tropical Atlantic (PIRATA), e.g., [32].

The net surface energy budget will be evaluated in three ways:

- (1) through estimation of the local storage and horizontal advection of heat based on simultaneous reanalysis of ocean temperature and currents. This will be a check on the net heat storage [33].
- (2) through comparison with the heat budget at fixed mooring sites in the tropics, which can be used to check on our integrated net flux, e.g., [4].
- (3) through comparison with changes in steric sea level estimates from satellite altimetry as a further check on net heat loss or gain.

5. SOME RESULTS

We have been able to follow wind bursts and the associated evaporation variations across the Atlantic Ocean and into the Caribbean [34]. We present here just one example of three individual terms in Eq. 1. Fig. 5 shows three-month averages over the months of January, February, and March in 1996 of latent heat flux, short wave downward radiation, and net longwave heat flux. We note the effects of the cloudiness associated with the ITCZ just north of the equator in the SW radiation and the maximum solar heating south of the equator at this time of year. The net longwave flux is close to zero in the deep tropics due to the humid atmosphere and cloudiness causing large values of downward longwave radiation. To the north and south, there are relatively large net longwave losses in the clearer, drier atmosphere of the subtropical high pressure regions. Latent heat flux is very small from the cold upwelling waters off Africa, both north and south of the equator. The role of the tradewinds in enhancing the evaporation is clearly seen with very large values just north of South America and along the Gulf Stream.

6. SUMMARY AND PLANS

We have methods and data to obtain all the terms in Eq. 1 using satellite techniques. We will analyze the net heat flux for the integrated values over months and years and study

the relationship to known advection in the ocean, SST changes and climate signals, such as the drought in West Africa. We will then test whether these fluxes produce more realistic oceanic circulations when forcing the ocean reanalysis models (compared with atmospheric model fluxes).

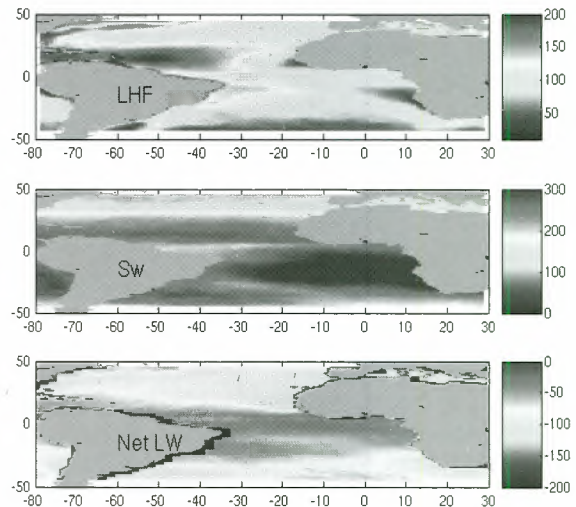


Figure 5. Averages of three flux terms over the first three months of 1996. Scales are in $W m^{-2}$.

For the complete oceanic model, we need in addition to the heat flux, the momentum flux and the net mass flux. The momentum flux for a daily gridded field is obtained already quite accurately. Net heat flux will be available as a weekly gridded field (due to the uncertainty in the latent heat flux), but the radiative fluxes can be had at finer temporal resolution.

To fully cover the forcing fields that drive the ocean circulations, one also needs the mass flux, i.e., the net salt flux as a difference between evaporation and precipitation. We plan to use the evaporation calculation together with existing precipitation estimates, such as produced by [35] from multiple satellites and spectral regions (microwave, IR, and visible measurements). From these sources we can then calculate the salt flux/salinity variation.

Future satellite systems will improve the coverage and accuracy of all the sensors employed today. However, in order to develop a long time series worthy of a climate record, we also must use the existing time series as soon as possible. This requires that we continuously test and refine our methods, as presented here, and work towards better measurements and increased sampling of the relevant variables. The existing data already allow analysis of the variability and trends in the tropical atmosphere and ocean structure, and their relationship to important human environments such as continental Africa, South America, and the North American storm track region.

ACKNOWLEDGMENTS

We express our appreciation for the international collaboration of the METEOSAT Second Generation Research and Applications Program with its free and open access to the data that allows use of the best of all available data products, in this case METEOSAT-8, for our scientific goals. The participation in the MSG-RAO significantly enriched our experiences.

REFERENCES

1. U.S.-CLIVAR Atlantic Implementation Plan, J. Hurrell and M. Visbeck (co-chairs), http://www.usclivar.org/Pubs/ATLANTIC_IMPL_DEC00.PDF, 2000.
2. Mestas-Nuñez, A. M., and Enfield, D. B., Rotated global modes of non-ENSO sea surface temperature variability, *J. Climate*, Vol. 12, 2734-2746, 1999.
3. Goldenberg, S. B., Landsea, C. W., Mestas-Nuñez, A. M., and Gray, W. M., The recent increase in Atlantic hurricane activity: Causes and implications, *Science*, Vol. 293, 474-479, 2001.
4. Foltz, G., Grodsky, S. A., Carton, J. A., and McPhaden, M., Seasonal mixed layer heat budget of the tropical Atlantic, *J. Geophys. Res.*, Vol. 108, No. C5, 10.1029/2002JC001584, 2003.
5. Foltz, G., Grodsky, S. A., Carton, J. A., and McPhaden, M., Seasonal salt budget of the northwestern tropical Atlantic Ocean along 38°W, *J. Geophys. Res.*, Vol. 109, No. C3, 10.1029/2003JC002111, 2004.
6. Carton, J. A., Cao, X., Giese, B. S., and da Silva, A. M., Decadal and interannual SST variability in the tropical Atlantic Ocean, *J. Phys. Oceanogr.*, Vol. 26, 1165-1175, 1996.
7. Delworth, T. L., and Mehta, V. M., Simulated interannual to decadal variability in the tropical and subtropical North Atlantic, *Geophys. Res. Lett.*, Vol. 25, 2825-2828, 1998.
8. Xie, S.-P., and Carton, J. A., Tropical Atlantic variability: Patterns, mechanisms, and impacts, In *Earth's Climate: The Ocean-Atmosphere Interaction*, C. Wang, S.-P. Xie, and J.A. Carton, Eds., American Geophysical Union, Geophysical Monograph Series, Vol. 147, 2004.
9. Carton, J. A., and Giese, B. S., SODA: A reanalysis of ocean climate, *J. Geophys. Res.*, submitted, 2006.
10. Bentamy, A., Katsaros, K. B., Mestas-Nuñez, A. M., Drennan, W. M., Forde, E. B., and Roquet, H., Satellite estimates of wind speed and latent heat flux over the global oceans, *J. Climate*, Vol. 16, No. 4, 636-656, 2003.
11. Rossow, W. B., and Duenas, E. N., The International Satellite Cloud Climatology Project (ISCCP) web site, *Bull. Amer. Meteorol. Soc.*, Vol. 85, No. 2, 167-172, 2004.
12. Gupta, S. K., Stackhouse, P. W., Cox, S. J., Mikovitz, J. C., Zhang, T., and Hinkelma, L. M., The NASA GEWEX surface radiation budget, AGU 2006 Spring Meeting, Baltimore, MD, May 23-26, 2006.
13. Pinker, R. T., Zhang, B., and Dutton, E. G., Do satellites detect trends in surface solar radiation? *Science*, Vol. 308, No. 5723, 850-854, 2005.
14. Schmetz, J., Pili, P., Tjemkes, S., Just, D., Kerkmann, J., Rota, S., and Ratier, A., An introduction to Meteosat Second Generation (MSG), *Bull. Amer. Meteorol. Soc.*, Vol. 83, No. 7, 977-992, 2002.
15. Govaerts, Y., Wagner, S., and Clerici, M., *SEVIRI Native Format Pre-Processing Toolbox User's Guide*, Version 2.2, EUMETSAT, Rept. No. EUM/OPS-MSG/TEN/03/0011, 2005.
16. Pinker, R. T., Wang, H., King, M., and Platnick, S., First use of MODIS data to cross-calibrate with GEWEX/SRB data sets, *GEWEX News*, Vol. 13, No. 4, 4-5, 2003.
17. Curran, R., Mishchenko, M., Tegen, I., and Geogdzhayev, I., Global Aerosol Climatology Project (GACP): Structure, early products, and plans, *GEWEX News*, Vol. 8, No. 4, 3-4, 1998.
18. Mishchenko, M., Penner, J., and Anderson, D., Editorial: Global Aerosol Climatology Project (GACP), *J. Atmos. Sci.*, Vol. 59, No. 3, 249-249, 2002.
19. Liu, H., Pinker, R. T., and Holben, B. N., A global view of aerosols from merged transport models, satellite, and ground observations, *J. Geophys. Res.*, Vol. 110, No. D10, doi:10.1029/2004JD004695, 2005.
20. Sun, D., and Pinker, R. T., Surface temperature retrieval from MSG-SEVIRI observations, Part I: Methodology, *Int'l. J. Remote Sens.*, in review, 2006.
21. Schlüssel, P., Schanz, L., and Englisch, G., Retrieval of latent heat flux and longwave irradiation at the sea surface from SSM/I and AVHRR measurements, *Adv. Space Res.*, Vol. 16, No. 10, 10107-10116, 1995.
22. Brisson, A., Le Borgne, P., and Marsouin, A., *Downward Long-Wave Irradiance Product Manual*, Version 1.1, Ocean and Sea Ice, SAF, November, 2001.
23. Drennan, W. M., On parameterisations of air-sea fluxes, In *Atmosphere-Ocean Interactions*, Volume 2, W. Perrie, Ed., WIT Press, 1-32, 2006.
24. Smith, S. D., Coefficients for sea surface wind stress, heat flux, and wind profiles as a function of wind speed and temperature, *J. Geophys. Res.*, Vol. 93, 15,467-15,472, 1988.
25. Drennan, W. M., Zhang, J., French, J. R., and Black, P. G., Latent heat fluxes in the hurricane boundary layer, *Proc., 27th Conf. on Hurricanes and Tropical Meteorology*, Monterey, CA, April 24-28, 2006, American Meteorological Society, Boston, CD-ROM, 2006.

26. Liu, W. T., and Niiler, P. P., Determination of monthly mean humidity in the atmospheric surface layer over oceans from satellite data, *J. Phys. Oceanogr.*, Vol. 14, No. 9, 1451-1457, 1984.
27. Schulz, J., Schlüssel, P., and Graßl, H., Water vapor in the atmospheric boundary layer over oceans from SSM/I measurements, *Int. J. Remote Sens.*, Vol. 14, 2773-2789, 1993.
28. Schulz, J., Meywerk, J., Ewald, S., and Schlüssel, P., Evaluation of satellite-derived latent heat fluxes, *J. Climate*, Vol. 10, No. 11, 2782-2795, 1997.
29. DeCosmo, J., Katsaros, K. B., Smith, S. D., Anderson, R. J., Oost, W., Bumke, K., and Chadwick, H., Air-sea exchange of water vapor and sensible heat: The Humidity Exchange Over the Sea (HEXOS) results, *J. Geophys. Res.*, Vol. 101, No. 5, 12,001-12,006, 1996.
30. Kubota, M., and Shikauchi, A., Air temperature at ocean surface derived from surface-level humidity, *J. Oceanogr.*, Vol. 51, 619-634, 1995.
31. Yu, L., Weller, R. A., and Sun, B., Improving latent and sensible heat flux estimates for the Atlantic Ocean (1988-1999) by a synthesis approach, *J. Climate*, Vol. 17, 373-393, 2004.
32. Grodsky, S. A., Carton, J. A., Provost, C., Servain, J., Lorenzetti, J. A., and McPhaden, M. J., Tropical instability waves at 0°N, 23°W in the Atlantic: A case study using Pilot Research moored Array in the Tropical Atlantic (PIRATA) mooring data, *J. Geophys. Res.*, Vol. 110, C08010, doi:10.1029/2005JC002941, 2005.
33. Wang, J., and Carton, J. A., Modeling climate variability in the tropical Atlantic atmosphere, *J. Climate*, Vol. 16, No. 23, 3858-3876, 2003.
34. Katsaros, K. B., Mestas-Nuñez, A. M., Bentamy, A., and Forde, E. B., Wind bursts and enhanced evaporation in the tropical and subtropical Atlantic Ocean, In *Interhemispheric Water Exchange in the Atlantic Ocean*, G. Goni and P. Malanotte-Rizzoli, Eds., Elsevier Oceanographic Series, 463-472, 2003.
35. Adler, R. F., Huffman, G. J., Bolvin, D. T., Curtis, S., and Nelkin, E. J., Tropical rainfall distributions determined using TRMM combined with other satellite and rain gauge information, *J. Applied Met.*, Vol. 39, No. 12, 2007-2023, 2000.

OPERATIONAL DERIVATION OF SURFACE ALBEDO AND DOWN-WELLING SHORT-WAVE RADIATION IN THE SATELLITE APPLICATION FACILITY FOR LAND SURFACE ANALYSIS

Bernhard Geiger^{1,2}, Dominique Carrer¹, Catherine Meurey¹, and Jean-Louis Roujean¹

¹Météo-France, CNRM/GMME, 42 avenue Gaspard Coriolis, 31057 Toulouse Cedex, France

²Instituto de Ciência Aplicada e Tecnologia, Campo Grande, 1749-016 Lisboa, Portugal

ABSTRACT

The Satellite Application Facility for Land Surface Analysis hosted by the Portuguese Meteorological Institute in Lisbon generates and distributes value added satellite products for numerical weather prediction and environmental applications in near-real time. Within the project consortium Météo-France is responsible for the land surface albedo and down-welling short-wave radiation flux products. Since the beginning of the year 2005 Meteosat Second Generation data are routinely processed by the Land-SAF operational system. In general the validation studies carried out so far show a good consistency with in-situ observations or equivalent products derived from other satellites. After one year of operations a summary of the product characteristics and performances is given.

Key words: Surface Albedo; Down-welling Radiation; Land-SAF.

1. INTRODUCTION

The land surface albedo and down-welling surface short-wave radiation flux (DSSF) products are both derived from the $0.6\mu\text{m}$, $0.8\mu\text{m}$, and $1.6\mu\text{m}$ channels of the SEVIRI instrument. Albedo maps are provided once a day based on the most recent cloud-free observations available. Instantaneous estimates of the short-wave radiation flux are calculated with a temporal frequency of 30 minutes. The products are currently classified as “pre-operational” which signifies according to the relevant EUMETSAT terminology that they are “able to satisfy the majority of applicable requirements” and have been considered “suitable for early distribution to SAF users with documented limitations”. Four continental windows (Europe, North of Africa, South of Africa, and South America) are separately processed in the Land-SAF system. The product files are disseminated in the native MSG/SEVIRI projection with a specified timeliness of three hours via the Land-SAF website (<http://landsaf.meteo.pt/>) and by the EUMETSAT broadcast system EUMETCast.

2. SURFACE ALBEDO

The surface albedo quantifies the fraction of incident solar radiation that is reflected by the Earth’s surface. It constitutes an important element for characterising the surface energy balance. Since the albedo is “relatively close” to the physical measurements obtained by remote sensing one can expect to retrieve this quantity with a reasonable accuracy.

2.1. Methodology

The retrieval scheme comprises four successive steps: First the measured top-of-atmosphere radiances delivered by the satellite instrument are corrected for atmospheric effects in order to convert them into the corresponding top-of-canopy (TOC) reflectance factor values. The spectral TOC-reflectances then serve as the input quantities for the inversion of a linear model of the bi-directional reflectance distribution function (BRDF) which quantifies the dependence on the illumination and observation geometry. Spectral albedo values in the instrument channels are determined from the angular integrals of the model functions with the retrieved parameter values. Finally, a narrow- to broad-band conversion is performed with a linear regression formula.

Technically the processing chain comprises two distinct modules - one for atmospheric correction and one for model inversion and directional and spectral integration. The atmospheric correction module is applied separately on each image directly after acquisition. The inversion and albedo calculation module, on the other hand, operates on a set of TOC-reflectance images collected during one day. By using the previous inversion result as a priori information in a recursive scheme, a temporal composition of the information over a longer time period can be achieved in order to guarantee the coherence and completeness of the product while still preserving a rather high temporal resolution. The physical and mathematical background of the algorithm is explained in the Product User Manual [1] available on the project website. Relevant references are also listed in this document.

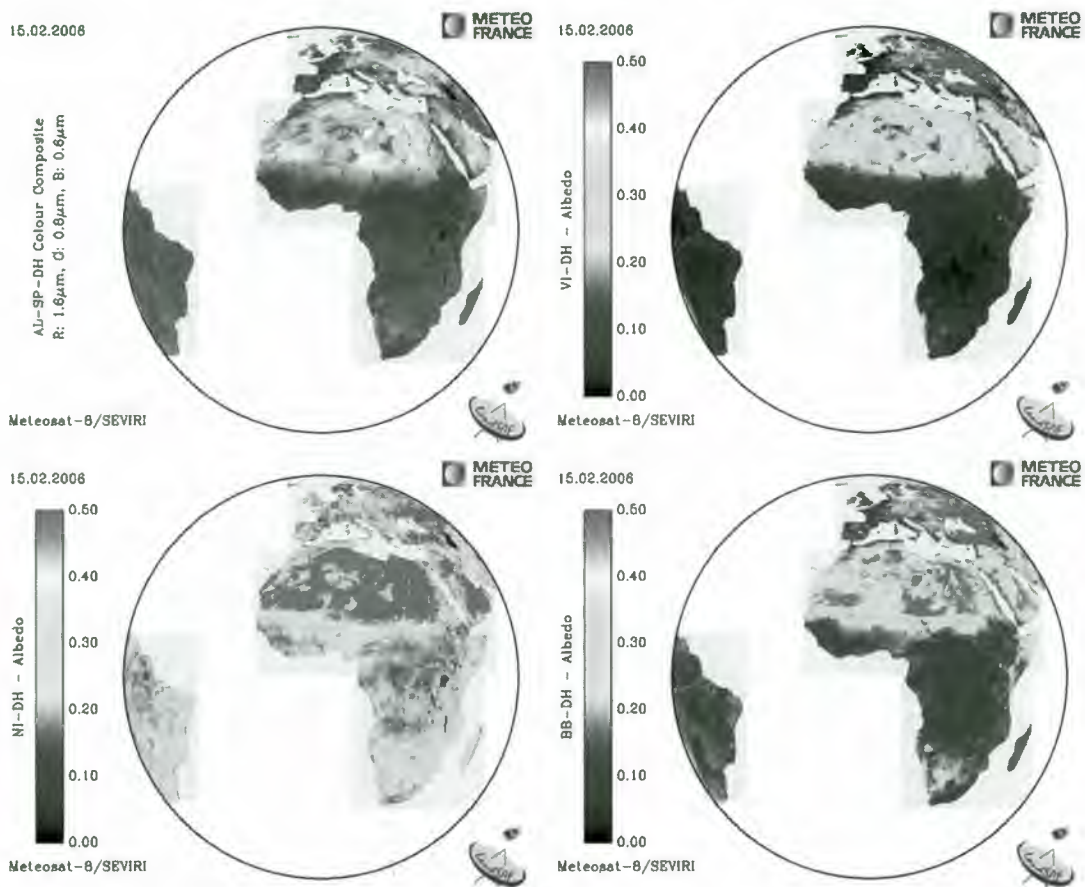


Figure 1. Directional-hemispherical albedo product images for the 15th of February 2006. Top Left: Colour composite of the three spectral albedo estimates. Top Right: Visible broad-band. Bottom Left: Near infrared broad-band. Bottom Right: Total short-wave broad-band.

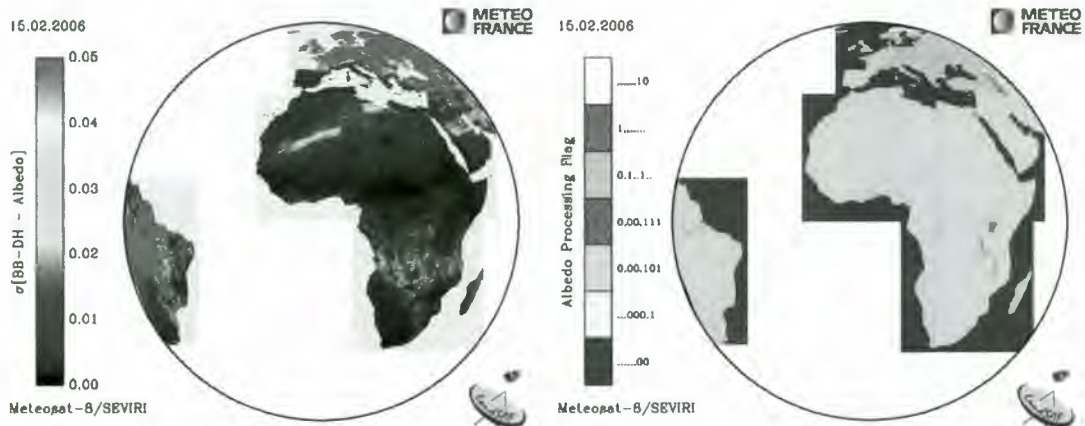


Figure 2. Left: Example for the uncertainty estimates (total broad-band directional-hemispherical). Right: The quality (or processing) flag for the 15th of February 2006. The processed areas appear in green, light blue (continental water), or grey (snow), and unprocessed areas in blue (ocean) and yellow.

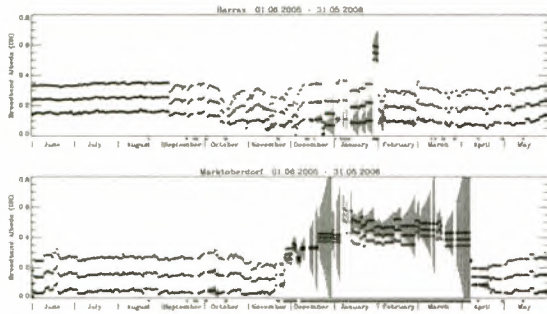


Figure 3. Time series of directional-hemispherical broadband albedo estimates for the image pixels corresponding to the location of Barrax (Albacete, Spain) and Marktobendorf (Allgäu, Germany). The colours grey, blue, and green, respectively, correspond to the total short-wave range, to the visible, and to the near infrared. The vertical bars indicate the respective uncertainty estimates. A red cross on the time axis indicates that no product file was generated by the operational system for the respective day. The blue star indicates that the pixel was flagged as snow covered.

2.2. Product Characteristics

The albedo product is generated on a daily basis. It comprises spectral albedo estimates corresponding to the three used SEVIRI channels as well as broad-band albedo estimates for the visible $[0.4\mu\text{m}, 0.7\mu\text{m}]$, near infrared $[0.7\mu\text{m}, 4\mu\text{m}]$, and total short-wave $[0.3\mu\text{m}, 4\mu\text{m}]$ intervals. Full disk example images generated by re-composing the four continental windows are shown in Fig. 1. The provided quantities include the directional-hemispherical (or ‘black-sky’) albedo at local solar noon and, for the spectral and total broad-band estimates, also the bi-hemispherical (or ‘white-sky’) albedo. The latter is relevant for a completely diffuse sky while the former corresponds to the presence of direct illumination only.

For each of the albedo quantities an uncertainty estimate is calculated by propagating estimates for the non-correlated (random) part of the input data errors through the model inversion (see the Product User Manual for details). The resulting values therefore quantify the contribution to the uncertainty due to random error sources and depend mainly on the number of observations available, the estimated TOC-reflectance errors, and the respective angular configuration. Sources of systematic errors, e.g. instrument calibration, are not taken into account in these uncertainty estimates. An example is depicted in Fig. 2. The quality flag also shown in this figure contains information about the land/water mask, the processed regions and potential snow cover.

Finally, Fig. 3 shows the resulting time series for two example sites. The largest albedo changes are provoked by snowfall and snowmelt. The seasonal evolution of vegetation and changes of soil humidity also induce temporal variability of the surface albedo. The product time series

may still contain high frequency noise caused by uncorrected atmospheric effects (e.g. due to variations of the aerosol concentration on small time scales) or by potential problems in the elimination of observations affected by clouds or cloud shadows. The rapidly increasing uncertainty estimates that can be seen for example at the end of December reflect the lack of information during periods without useful observations due to persistent cloudiness.

2.3. Validation

The albedo product has been (indirectly) validated by comparing it to the respective product derived from observations of the MODIS instrument [2], which is generally considered as being of good quality and suitable as a reference quantity. We re-projected the higher resolution MODIS product to the MSG/SEVIRI grid within the European continental window. For each original MODIS pixel the ‘closest’ SEVIRI pixel was determined and afterwards the albedo estimates for all MODIS pixels assigned to a given SEVIRI pixel were averaged. The MODIS product is generated with a temporal composition window of 16 days. In order to reproduce the temporal characteristics as closely as possible with the MSG data, the internal TOC-reflectance files provided by the operational system were re-processed to generate daily albedo estimates, which were then averaged over the relevant MODIS period. For expressing the validation results in a quantitative way we determine the bias - defined as the average of the difference between the two estimates - and the standard deviation of that difference. The temporal evolution of the validation statistics from June 2005 to March 2006 is visualised in Fig. 4. The position of the symbols in the graphs indicates the bias, and the length of the bars (from the centre to each end) corresponds to the standard deviation as defined above. The calculation of the statistics was restricted to those pixels for which the Land-SAF uncertainty estimate is below 0.10 and the MODIS quality flag indicates a high confidence.

Until the month of October, the biases between the Land-SAF and MODIS products are negligible for the near-infrared and total short-wave ranges and in the order of +0.015 for the visible range. The standard deviation in absolute units ranges between 0.015 for the visible and up to 0.03 for the near-infrared and total short-wave ranges. However, owing to the lower level of the albedo values, the discrepancies in relative units are the largest for the visible broad-band estimates. The results tend to deteriorate during winter, which may be related to the unfavourable observation conditions (clouds, low solar elevation), the smaller number of data points entering the validation statistics, and the different treatment of snow cover in the Land-SAF and MODIS algorithms. The validation studies will be pursued in more detail by considering the spectral albedo quantities and by investigating the performance as a function of season, geographic position, surface type, snow cover, precipitation, or atmospheric composition.

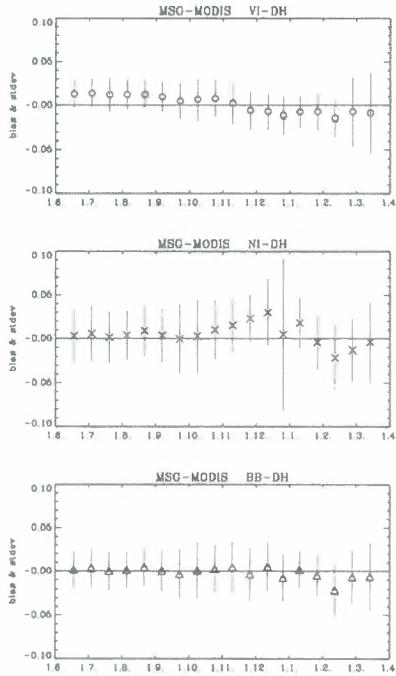


Figure 4. Time series of the directional-hemispherical albedo validation statistics (in absolute units) from June 2005 to April 2006. Top: Visible broad-band. Middle: Near infrared broad-band. Bottom: Total short-wave broad-band.

3. DOWN-WELLING SURFACE SHORT-WAVE RADIATION

The down-welling surface short-wave radiation flux (DSSF) refers to the radiative energy in the wavelength interval $[0.3\mu\text{m}, 4.0\mu\text{m}]$ reaching the Earth's surface per time and surface unit. It essentially depends on the solar zenith angle, on cloud coverage, and to a lesser extent on atmospheric absorption and surface albedo.

3.1. Methodology

The method for the retrieval of DSSF currently implemented in the Land-SAF system largely follows previous developments achieved at Météo-France in the framework of the SAF on Ocean & Sea-Ice [3]. Separate algorithms are applied for clear sky and cloudy sky situations. In the presence of clouds, the down-welling radiation reaching the ground is considerably reduced. The DSSF is strongly anti-correlated with the observable top-of-atmosphere reflectances: The brighter the clouds appear on the satellite images, the more radiation is reflected by them and the less radiation reaches the surface. In this case the top-of-atmosphere albedo is first calculated from the observed directional reflectance values by applying a broad-band conversion and an angular dependence model. The top-of-atmosphere albedo then

serves as the most important input information for a simple physical model of the radiation transfer in the cloud-atmosphere-surface system. In the clear sky method the DSSF estimate is directly determined with a parameterisation for the effective transmittance of the atmosphere as a function of the concentration of atmospheric constituents. A more detailed description is given in the Product User Manual [4].

3.2. Product Characteristics

The DSSF estimates are currently calculated at intervals of thirty minutes based on every second slot of MSG/SEVIRI images. The values are derived for the instantaneous acquisition time of each image line. The SEVIRI scans are performed from South to North. At the Northern edge of the image the reference time therefore deviates from the nominal slot time by up to twelve minutes.

The DSSF product files comprise the physical estimate as well as a quality flag. An example is given in Fig. 5. In the visualisation of the quality information the green colour refers to the regions for which the clear sky method was applied, the yellow colour indicates the application of the cloudy sky method, and the blue colour marks the ocean for which no estimates are derived. The other colours appearing in the legend refer to particular cases which do not occur very frequently. The detailed signification of the bit codes is explained in the Product User Manual.

3.3. Validation

Up to now the validation studies have been based on the Baseline Surface Radiation Network [5] stations of Carpentras (France) and Toravere (Estonia) for which data concomitant with our product time series were already available. In addition we had access to in-situ data from ground measurement stations run by the Land-SAF project in Evora (Portugal) and by Météo-France in Roissy (France).

In general a good agreement between the satellite estimates and the in-situ data is observed when comparing the daily time series. A few examples are shown in Fig. 6. In the unfavourable case depicted for Roissy with a rather large dispersion, the discrepancies cannot entirely be attributed to deficiencies of the retrieval method. The example also illustrates the limitation of the validation approach when the conditions are highly variable in space and time. At least part of the dispersion is a consequence of comparing a local measurement with an estimate for a rather extended image pixel.

For validation purposes we also calculated daily averages of the Land-SAF DSSF product for the pixels corresponding to the validation sites. This is helpful for comparing the quantitative validation statistics to those

of other products which are not available as instantaneous estimates. The daily values are determined by averaging all available (day-time) Land-SAF DSSF estimates for a given day. For comparison only the in-situ measurements corresponding to the product time slots actually used for the determination of the “daily DSSF product” are then also averaged to obtain the corresponding “daily averaged in-situ measurement”. (Note that this prescription is useful only for our validation purposes, but not appropriate for generating a daily averaged DSSF product meant to be distributed and utilised. For this purpose the problems of temporal reference for the average and the treatment of missing data would have to be considered much more carefully.)

The temporal evolution of the statistical quantities - bias and standard deviation - for all four stations combined over the whole available validation period is shown in Fig. 7. Monthly sub-samples of the validation data points are considered in order to illustrate a possible temporal evolution of the product quality. From the top left to the bottom right the panels show the results for the data points processed with the clear sky method, for the cloudy sky method, for all processed day-time data points combined irrespective of the method applied, and for the daily averaged DSSF values which were calculated for validation purposes only as described above. The top left plot for clear sky also includes the bias values (but not the standard deviation) for morning and afternoon data points separately. Considering the whole validation period and all sites there is a small positive bias in the order of 5 Wm^{-2} for both clear and cloudy sky situations. The standard deviation is in the order of 40 Wm^{-2} for the clear sky and 115 Wm^{-2} for the cloudy sky (instantaneous) estimates while it reduces to 30 Wm^{-2} for the daily averaged values.

4. PERSPECTIVES

In general the validation results obtained so far show a good consistency with in-situ observations or equivalent products derived from other satellites. Nevertheless the present Initial Operational Phase still allows us to adjust the algorithms and implement some methodological improvements. In addition to continued validation studies we intend to test the application of the products in surface and NWP models in order to get a direct feedback for further development.

For the albedo algorithm minor adjustments of the narrow- to broad-band conversion relations may be required depending on the results of extended validation studies. In addition, the quality of the input information for the atmospheric correction scheme needs to be improved. In particular the presently employed climatology for the aerosol optical thickness should later be replaced by a dynamic aerosol product in order to remove from the surface albedo time series potential spurious fluctuations caused by unaccounted atmospheric variability.

The directional-hemispherical albedo is given for a reference angle corresponding to the local solar noon. We plan to provide a parameterisation which enables the user to calculate the diurnal albedo cycle. In addition to the currently available albedo product, which is suitable for near real time applications, we also envisage the implementation of a variant with different temporal characteristics based on the accumulation of the observations acquired within a “classical” temporal composition. Such an approach is appropriate for example for deriving a climatology of the variables characterising the surface properties.

After the launch of the first satellite of the MetOp series, the data acquired by the AVHRR instrument onboard will also be processed and exploited by the Land-SAF system. Owing to the complementary observation geometry resulting from the polar orbit, the additional information will be particularly beneficial for the albedo product - provided that technical problems such as geolocation and channel inter-calibration can be controlled with sufficient precision. It is planned to merge the data at the level of the TOC-reflectance factor by inverting the BRDF model with observations from both the SEVIRI and AVHRR instruments. Especially for high latitudes during winter this will significantly improve the constraints for model inversion and hence the quality of the result.

Concerning the DSSF estimates for cloudy sky conditions there is still some room for improvement by fine tuning and adapting some of the parameters used in the algorithm or by exploiting additional information such as the cloud type. For clear sky we envisage to re-formulate the currently applied parameterisation as a function of the aerosol optical thickness for which we expect that a dynamic estimate will be available in the near future in the framework of other projects.

In addition to the presently available instantaneous flux estimates it is planned to implement a daily averaged or integrated product during the forthcoming project phase. By taking into account the observations delivered by the polar-orbiting system this product could be improved and extended towards high latitudes beyond the region covered by the Meteosat disk.

REFERENCES

- [1] Land-SAF, 2005, Land Surface Albedo, Product User Manual, Version 1.3
- [2] MODIS Albedo: <http://www-modis.bu.edu/brdf>
- [3] OSI SAF, 2002, Surface Solar Irradiance Product Manual, Version 1.2. <http://www.osi-saf.org>
- [4] Land-SAF, 2006, Down-welling Surface Short-wave Radiation Flux, Product User Manual, Version 1.3
- [5] Baseline Surface Radiation Network: <http://bsrn.ethz.ch>

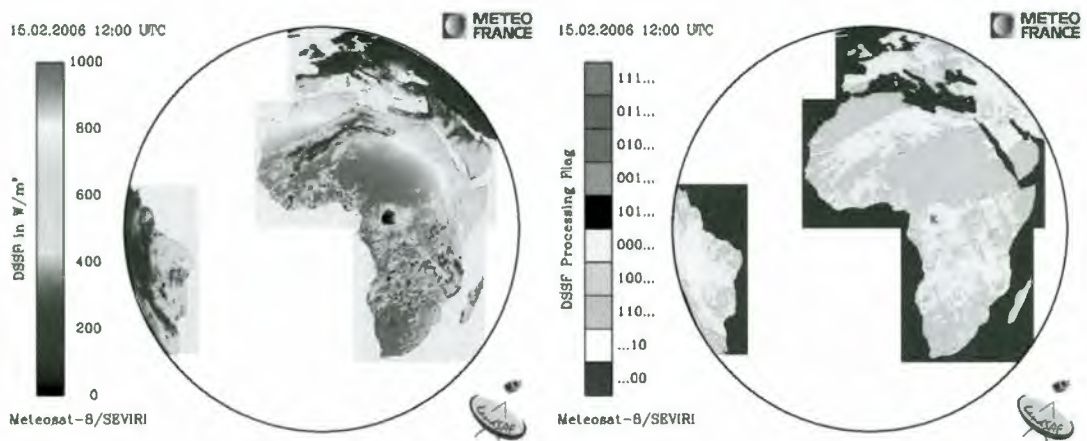


Figure 5. The DSSF estimate (left) and the corresponding quality (or processing) flag information (right) generated for the 15th of February 2006 at 12:00 UTC.

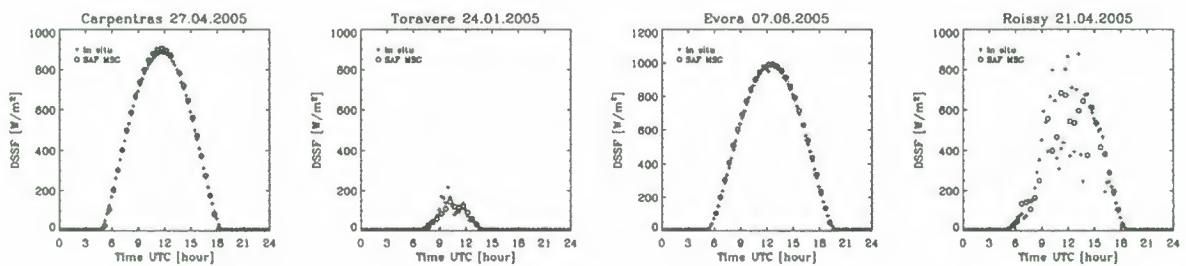


Figure 6. Examples for daily time series of DSSF estimates and in-situ measurements at the ground validation stations. The colour code of the dots is the same as for the quality flag in the previous figure.

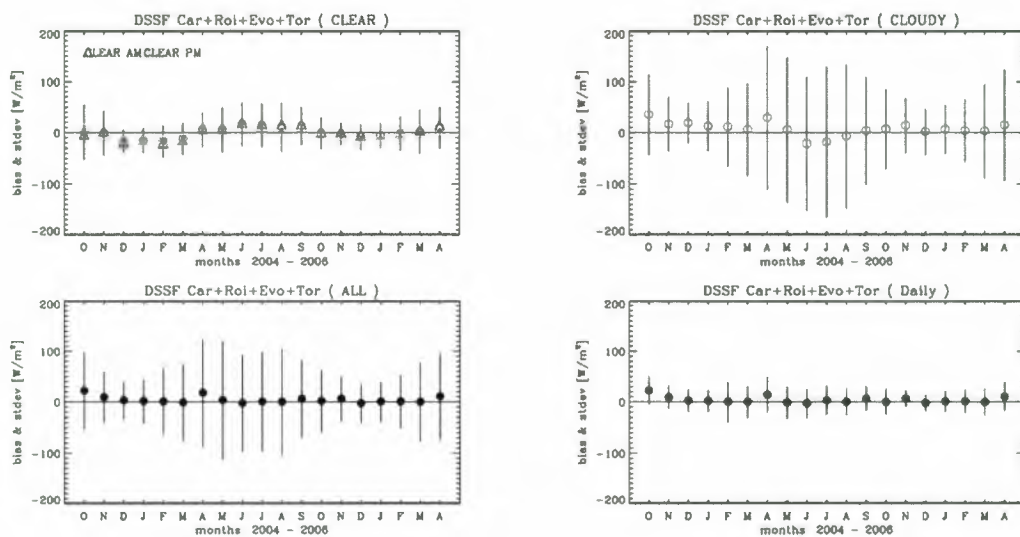


Figure 7. Temporal evolution of bias and standard deviation between the Land-SAF DSSF estimates and ground measurements for all validation stations combined (Carpentras, Roissy, Evora, and Toravere).

MSG SEVIRI DATA FOR VEGETATION MONITORING AND LAND SURFACE PROCESS MODELING IN AFRICA

Inge Sandholt⁽¹⁾, Simon Stisen⁽¹⁾, Rasmus Fensholt⁽¹⁾, Mads O. Rasmussen⁽¹⁾, Anette Noergaard⁽¹⁾, Karl M. Iversen⁽¹⁾, Torsten Bondo⁽¹⁾ and Synne H. Svendsen⁽¹⁾

⁽¹⁾ Department of Geography, University of Copenhagen, Oester Voldgade 10, 1350 Copenhagen K (Denmark),
Email: is@geogr.ku.dk

ABSTRACT

The processing of MSG-SEVIRI data at the Department of Geography, University of Copenhagen is presented. Spectral reflectances, vegetation index, surface and air temperature are being estimated for the African continent, and in this study compared to in situ measurements in West Africa. A potential application area is illustrated by applying the data as input to a regionalized SVAT model for the Okavango delta.

1. INTRODUCTION

Monitoring and modeling of dynamical systems requires a high temporal frequency of data. This can be achieved by using data from the SEVIRI sensor on board the Meteosat Second Generation satellite, with its improved capabilities for vegetation monitoring and higher accuracy in surface temperature in comparison to previous geostationary systems. SEVIRI scans the globe-disk centered over Africa with a temporal frequency of 15 minutes, which meets the requirements for input data from a range of models of land surface processes. The high temporal resolution also makes MSG-SEVIRI data a reliable data source for vegetation monitoring because of a higher chance to obtain cloud free image acquisitions. At the Department of Geography, an MSG-SEVIRI processor has been set up, with the aims of providing an improved product for vegetation monitoring as compared to data from Polar Orbiting Satellites, and to provide robust and consistent time series of input data for Land Surface Process and Distributed Hydrological Modeling. Special attention has been paid to the African continent, where access to suitable data has previously made these types of studies difficult. In this paper, the processor and the preprocessing steps will be described, including the correction of atmospheric effects of the visible, near infrared and thermal channels. Evaluation of the estimated variables are done by comparing to in situ measurements, and potential improvements of land surface modelling performance, is illustrated using an example from the Okavango Delta.

2. METHOD

A processing system has been set up using IDL routines partly based on the 'SEVIRI Native format pre-processing toolbox'[1]. The processing steps include geo-rectification, calibration and atmospheric correction of the visible and near-infrared bands (1, 2

and 3) using the SMAC algorithm. Further Normalized Difference Vegetation Index (NDVI), Land Surface Temperature (LST) and air temperature are derived.

2.1 Preprocessing

The MSG-1 SEVIRI data is received as MSG level 1.5 data through the EUMETCast HRIT transmission service using Hotbird-6 and pre-processed using MSG Data Manager Pro by David Taylor [2]. Output from the data manager is in 16 bit pgm file format. Channels 1 to 11 are then imported into IDL and calibrated using the calibration coefficients provided with the data stream over EUMETCast.

2.2 Atmospheric correction of bands 1-3.

The atmospheric correction of the red, near-infrared and SWIR bands from Top Of Atmosphere (TOA) reflectances into surface values is done using the SMAC algorithm (a Simplified Method for the Atmospheric Correction of satellite measurements in the solar spectrum) [3], an approach used by the Land SAF as well [4]. SMAC is a simple and fast technique based on the 5S code applicable to a range of satellite sensors and it accounts for atmospheric absorption and scattering due to gaseous constituents and aerosol content of the atmosphere. We have used the coefficients developed by Beatrice Berthelot [5], for the three channels. The accuracy of the SMAC code decreases for solar zenith angles greater than 60°, for viewing angles greater than 50°, and for optical depths greater than 0.8 at 550 nm [3]. Thus, the algorithm is applicable for SEVIRI data for the major part of the African continent; view angles larger than 50° are found in the fringes of the continent only.

Daily values of atmospheric composition (water vapour, aerosols, and ozone) are derived from the Level-3 MODIS Terra and Aqua Atmosphere Daily Global Products, which are sorted into 1°x1° cells on an equal-angle grid. Ideally water vapour, aerosols, and ozone should be derived directly from SEVIRI data enabling an accurate temporal correspondence between the scene to be corrected and atmospheric input data for correction. At present time the MODIS data are however the best solution even though diurnal variations in water vapour and aerosols occur; potentially introducing inaccuracies in the diurnal range of observed NDVI.

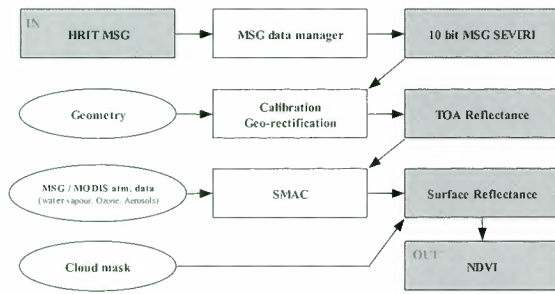


Figure 1. The MSG SEVIRI processor as implemented at the Department of Geography, University of Copenhagen. Processing steps for Channels 1-3.

The estimate of errors in retrieving the total atmospheric water vapour and total ozone are both 10% [6] and the aerosol optical thickness (τ_a) can be sensed with an estimated error of $\tau_a=0.05$ to 0.1 for small optical thickness, increasing to 20–30% for high optical thickness [7]. Daily composites of the entire African continent are performed from the MODIS Terra morning and Aqua afternoon over pass by simple averaging. A standard distribution filter is applied to fill out data gaps generated by the orbital coverage of Terra or Aqua data and finally data are resampled by bilinear interpolation to match the MSG SEVIRI pixel size.

2.3 Normalized Difference Vegetation Index

NDVI is based on the difference in reflectance in the red and near infrared part of the electromagnetic spectrum [8]. In case of the MSG SEVIRI sensor, NDVI is calculated using bands 1 and 2:

$$NDVI = \frac{\rho_{0.8} - \rho_{0.6}}{\rho_{0.8} + \rho_{0.6}} \quad (1)$$

Where $\rho_{0.6}$ and $\rho_{0.8}$ are the surface reflectances of band 1 and 2 respectively (after atmospheric correction).

2.2.2 Land surface temperature

Land surface temperature (LST) is calculated using the simplified split window approach developed by [9] using MSG SEVIRI band 9 and 10 centred at 10.8 and 12.0 μm respectively:

$$\begin{aligned} T_s = & T_{10.8} + [3.17 - 0.64 \cos \theta](T_{10.8} - T_{12.0}) \\ & + \left[0.05 - \frac{0.157}{\cos \theta} \right] (T_{10.8} - T_{12.0})^2 \\ & + \left[65 - \frac{4}{\cos^2 \theta} \right] (1 - \varepsilon) + \left[-11.8 + \frac{5.1}{\cos \theta} \right] W(1 - \varepsilon) \\ & + \left[-180 + \frac{24}{\cos \theta} \right] \Delta\varepsilon + [-4 + 34 \cos \theta] W \Delta\varepsilon - 0.6 \end{aligned} \quad (2)$$

Where T_s is the surface temperature, $T_{10.8}$ and $T_{12.0}$ are the calibrated radiances measured by the sensor in bands 9 and 10 respectively, ε is the effective mean emissivity of the ground, $\Delta\varepsilon$ is the difference between the emissivity of the ground for bands 9 and 10 respectively [9]. W is the total atmospheric water vapour (in g/cm^2), θ is the view zenith angle. The method requires information on the band specific emissivity of each MSG pixel which is found using the Vegetation Cover Method proposed by [10] which expresses the emissivity as a linear combination of the ground and vegetation emissivity weighted according to the fractional vegetation cover (FVC) (see eq. 3). The land cover map and band specific emissivities for each class were obtained from [11].

$$\varepsilon_{i, \text{pixel}} = \varepsilon_{i,v} \cdot FVC + \varepsilon_{i,g} (1 - FVC) \quad (3)$$

The fractional vegetation cover was found by using the relation between NDVI and FVC proposed by [12]:

$$FVC = \frac{NDVI - NDVI_{\min}}{NDVI_{\max} - NDVI_{\min}} \quad (4)$$

Currently NDVI from the GIMMS data set [Tucker, 2005] is applied for the estimation of FVC, as it provides a more realistic evolution of NDVI compared to the MSG-derived NDVI values which contain noise due to angular effects (described later).

2.3 Air temperature

Air temperature, T_a , is obtained through investigation of the T_s -NDVI correlation, also referred to as the temperature-vegetation index (TVX), under the assumption that vegetation canopy temperature equals near surface air temperature. See [13] and [14] for details on the method. This method is very sensitive to the seasonal bias introduced by solar zenith angle variations in both T_s and NDVI, especially since these have same effect (overestimation of T_s and underestimation of NDVI). Further, this method requires a certain amount of vegetation and is thus only applicable during the growing season and only work between approximately 9:00 and 14:00 local sun time. These are important limitations when considering that the air temperature is needed as input for hydrological modelling, as the hydrological model need input data for every timestep, not only for parts of the day and parts of the year.

2.4 Validation data

Validation of the derived products is partly done by comparison with in situ measurements from a test site located in Dahra, Senegal (coordinates 15.436°W 15.410°N). Here, surface reflectances and radiances are measured using light and thermal infrared sensors

mounted 10 meters above ground at nadir. The measured wavelengths matches the MSG SEVIRI sensor in the visible and near infrared bands. The site located in an area dominated by annual grasses and shrubs. Vegetation growth is mainly limited by water, thus making rainfall the main determinant on the amount of vegetation. Rainfall is highly variable from year to year, leading to large differences in biomass production between years. Comparing point measurements representing less than 50m² with a single MSG-pixel representing somewhere between 25 and 40 km² requires that the area is very homogenous and that the variable in question scale linearly, both assumptions that do not hold in practice. On the other hand will such a comparison give an indication of the performance of the MSG-derived values as the surface conditions only vary slowly over the region.

The air temperatures are validated against synoptic data for 18 stations throughout and around the Senegal River Basin.

3. RESULTS AND DISCUSSION

3.1 Normalized Difference Vegetation Index

The NDVI was calculated from the MSG bands 1 and 2. Due to the changing sun-sensor geometry, NDVI is not static throughout the day [15]. Therefore, the NDVI values at solar noon ± 2 hours have been averaged (after cloudmasking). Further a certain number of daily NDVI values have to be available before the average value is calculated. This is done to avoid outliers due to inaccuracies in the cloud mask which might allow for a few daily samples which are in fact influenced by unmasked clouds. This is not an optimal solution, but it does minimize some of the directional effects (though not taking influences of the view zenith angle into account). A proper description of the BRDF and a correction/normalization scheme of the reflectances are currently being investigated. Fig. 2 show the MSG-NDVI compared to in situ measurements from the Dahra test site from June 2004 until December 2005 (in situ measurements are only available during the growing season). The MSG NDVI values generally show higher variability than the in situ measurements, and in certain periods there are a large difference between the the two NDVI estimates. During the 2004 growing season the MSG NDVI values are generally lower than the in situ measured values, and seem to peak later as well. During the 2005 growing season on the other hand, the MSG NDVI are generally higher than the in situ measurements, but perform better on the timing. Further the MSG NDVI seems to catch the two NDVI maxima caused by an early rain-event followed by a dry spell. For both 2004 and 2005 the MSG NDVI values are lower than the in situ measurements at the end of the growing season, especially in 2005.

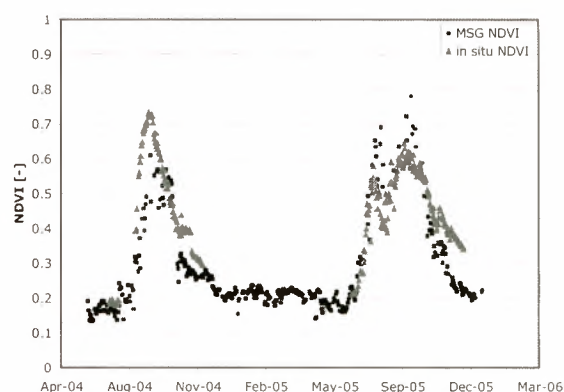


Figure 2. MSG derived NDVI and in situ measured NDVI at the test site in Dahra, Senegal.

In order to overcome some of the angular effects in the derived MSG NDVI values, the BRDF corrected Land SAF albedo DH product was tested [16]. Using the spectral albedos for band 1 and 2, the NDVI was calculated for the growing season of 2005. Fig. 3 shows the Land SAF NDVI along with the “raw” NDVI (averaged values between 10:00 and 14:00 local sun time) and the in situ measured values. The Land SAF NDVI values show much higher variability than the averaged raw NDVI values, especially at the beginning of the growing season. The double peak discernable in the averaged raw NDVI values and in the in situ measurements can not be identified in the Land SAF NDVI time series. The maximum values in the Land SAF NDVI values are also considerably lower than the averaged raw NDVI values, but closer to the in situ measured values.

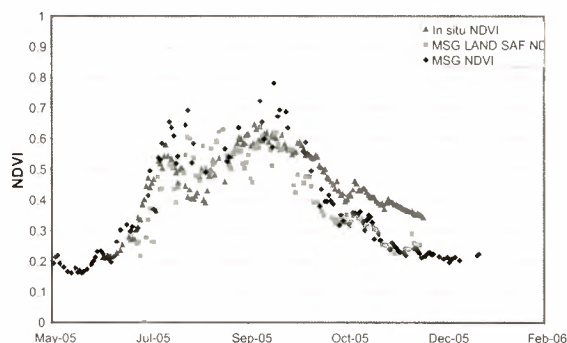


Figure 3. MSG, LAND SAF and in situ measured NDVI for the Dahra test site for the growing season 2005

3.2 Land surface temperature

The MSG derived land surface temperatures were compared with in situ measurements from the test site in Dhara, Senegal. Fig. 4 and 5 show the measured and MSG derived LST for the years 2004 and 2005. In situ measurements are only available during the growing season, and slightly longer for 2005 than for 2004. The

statistics for the two years show slightly better performance during 2005 with an r^2 value of 0.829 compared to 0.774 for 2004. The root mean square error (RMSE) is also slightly smaller for 2005 at 3.49 degrees Celsius compared to 3.96 degrees Celsius for 2004.

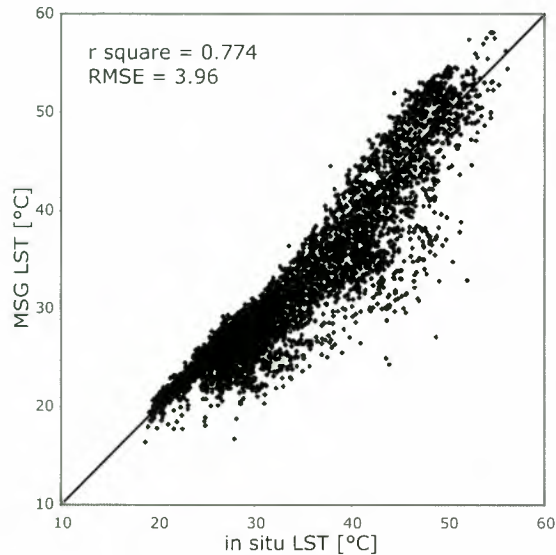


Figure 4. MSG LST and in situ measured LST for 2004 (growing season only)

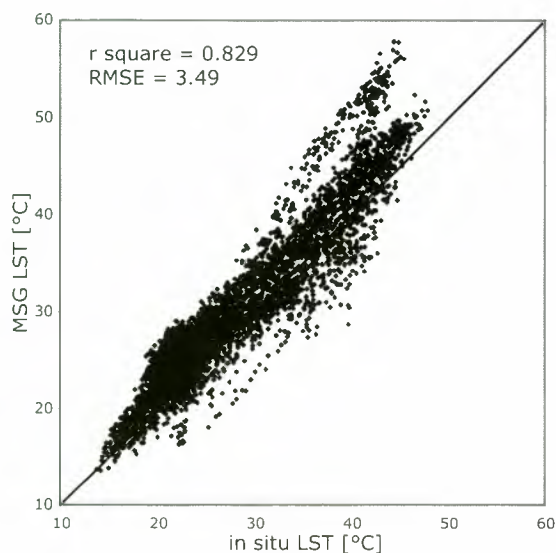


Figure 5. MSG LST and in situ measured LST for 2005 (growing season only)

In 2005 the MSG seems to overestimate for high temperatures for a certain period, which is apparent in the scatterplot as a small cloud of points above the 1:1 line in the upper part of the plot. Further investigation into the reasons for this overestimation, reveal that it is

caused by scaling effects between the MSG resolution and the ground measurements. On November 11th 2005 approximately 2/3 of the MSG pixel burned of during a large bushfire. But the area around the measuring site is left untouched by the fire. Due to the dark colour of the ground within the burned area, this part of the MSG pixel must be expected to get much warmer than the unburned area, resulting in much higher temperatures being recorded by MSG compared to the in situ measured temperatures. The apparent overestimation by MSG is thus not actually an overestimation but a scaling issue due to the fact that very different conditions exist between the area measured by MSG and by the thermal infrared sensors.

3.3 Air temperature

Air temperatures have been calculated using the TVX method [13], [14] and an example is shown in fig. 6 for the Senegal River Basin. The algorithm only works for cloudfree pixels and under certain ground conditions, and do thus not provide air temperatures for all pixels. The general pattern of the estimated air temperatures are as expected: Higher temperatures (bright colours in fig. 6) prevail in the northern regions where vegetation cover is sparse than to the south where more vegetation is present. There are though, a few areas in the north where much lower temperatures are found. Further analysis showed that some of these low temperatures are due to residual clouds not picked up by the MSG cloudmask. Other are located close to areas with open water surfaces which causes problems for the algorithm.

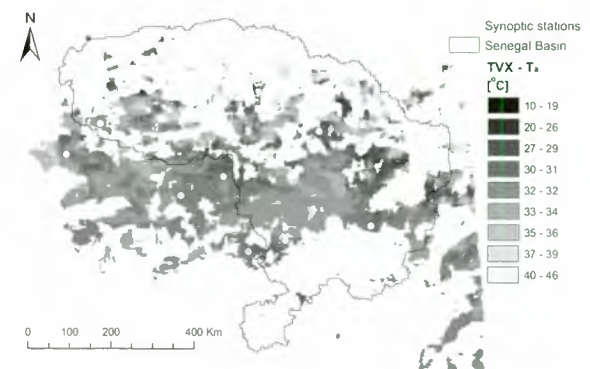


Figure 6. Air temperature derived from MSG data. The solid line shows the location of the Senegal River Basin.

As also mentioned in section 2.3, the algorithm only work under certain ground conditions and at certain times of day. In our study this limits the applicability of the algorithm to between 9:00 and 14:00 and only for the growing season (from approximately July 1st until the end of October). Geographically the method also seems to be limited in applicability to an area

stretching East-West across the Sahel region, and can thus not be applied successfully in either the dryer area to the north or to the more densely vegetated area to the south. Further the method is very sensitive to errors in LST and NDVI, which stresses the need for adequate correction for angular effects, atmospheric correction and for realistically varying time series (both in terms of diurnal and seasonal variations) of these variables.

4. IMPROVED MODEL RESULTS

One application of MSG data that benefit from the high temporal resolution of the MSG sensors, are distributed hydrological modeling. Further the presence of both a red, a near-infrared and thermal bands allow for assimilation of variables like LST and air temperature using the methods described above into these models. The data can be used either as input, as calibration parameters or for validation. In most cases, having spatially distributed estimates of LST and air temperature every third, or even every hour, will be a major step, compared to standard input which in many cases consist of synoptic data for one or a few meteorological stations located within or in the vicinity of the study area. Theoretically, data are available from MSG every 15 minutes, but less is in most cases sufficient to capture the diurnal variations sufficiently.

Fig. 7 shows a comparison between evapotranspiration simulated by two model runs of the MIKE SHE SVAT model which have been set up for the Okavango Delta in Botswana [17]. The difference between the two panels is the source of the air temperatures and global radiation. In the top panel the simulation is based on air temperature (3 hour resolution) and global radiation (hourly) derived from MSG compared to a daily mean air temperature and an estimate of global radiation based on daily sun-hours both from a synoptic station in the lower panel. At the time depicted in the figure, the north-western part of the delta is covered by clouds yielding much lower evapotranspiration rates in the model run using MSG data in this part of the delta. Contrary, the evapotranspiration rates in the south-eastern part of the delta are similar for both model runs. This example demonstrates the potential of using MSG-derived input in distributed hydrological models, though difficulties relating to clouds and missing data needs to be addressed.

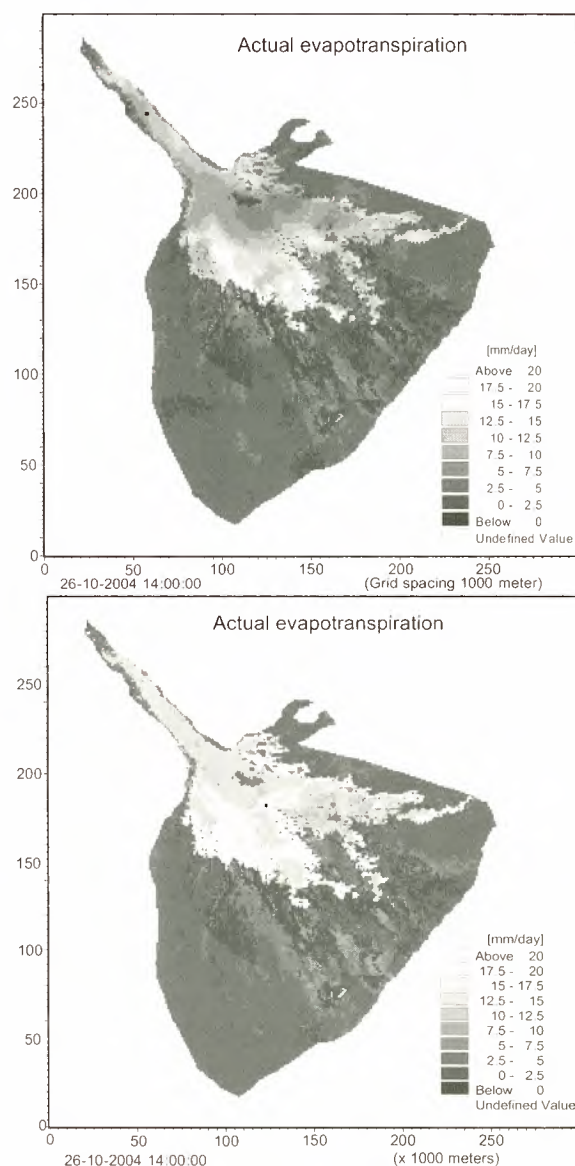


Figure 7. The images show the evapotranspiration for the Okavango Delta, Botswana, at 12.30 local sun time as estimated by the MIKE SHE SVAT model. The upper image show for the model run using MSG derived inputs, while the lower uses synoptic data.

5. CONCLUSIONS AND PERSPECTIVES

Based on SEVIRI data we are able to derive NDVI, Surface temperature and air temperature, with a temporal and spatial resolution sufficiently high so that the data can be used for input to a regionalized SVAT model. We are currently testing a method for estimation the water vapour content in the atmosphere from the split window channels based on the method developed by [18], allowing us to use MSG data only for the atmospheric correction. BRDF corrections have not been solved, and preliminar results based on a

comparison with LAND SAF data show that further work is needed, and work is in progress in that direction. We are also currently investigating the possibility of using the TIMESAT software [19] for creating a smoothed NDVI curve based on the MSG derived NDVI values.

6. ACKNOWLEDGEMENTS

The study has been funded by the The Danish Agricultural and Veterinary Research Council Grant no. 23-01-0153, and The Danish Scientific Research Council, Grant no. 21-03-0578, and OTICON. MSG data copyright EUMETSAT, MSG-RAO PI project ID 110.

7. REFERENCES

1. Govaerts, Y., Wagner, S., Clerici, M., 2005. SEVIRI native format preprocessing toolbox. User's guide. *Technical report EUM/OPS-MSG/TEN/03/0011*, EUMETSAT, Am Kavalleriesand 31. Postbox 10 05 55. D-64205 Darmstadt.
2. Taylor, D. <http://satsignal.eu>
3. Rahman, H., & Dedieu, G. (1994). SMAC: A simplified method for the atmospheric correction of satellite measurements in the solar spectrum. *International Journal of Remote Sensing*, 15 (1), 123–143.
4. Geiger, B., Franchisteguy, L., Lajas, D., & Roujean, J. -L. (2004). Operational near real-time derivation of land surface albedo and down-welling shortwave radiation from MSG observations. *Proc. second MSG RAO workshop, Salzburg, Austria. ESA SP 582*.
5. Berthelot, B. (2003). Coefficients SMAC pour MSG. Technical Report, *Noveltis Internal Report NOV-3066-NT-834*.
6. Menzel, W.P., Gumley, L.E. (1998). MODIS atmospheric profiles retrieval algorithm theoretical basis document. *Technical report ATBD-MYD-07*, NASA Goddard Space Flight Center.
7. Kaufman, Y.J., Tanre, D. (1998). Algorithm for remote sensing of tropospheric aerosol from MODIS, algorithm theoretical basis document. *Technical report ATBD-MYD-02*, NASA Goddard Space Flight Center.
8. Tucker, C.J., 1979, Red and photographic infrared linear combinations for monitoring vegetation, *Remote Sensing of Environment*, 8, 127-150.
9. Sobrino, J.A., & Romaguera, M. 2004. Land surface temperature retrieval from MSG1-SEVIRI data. *Remote Sensing of Environment*, 92, 247-254.
10. Valor, E. and Caselles, V. (1996). Mapping land surface emissivity from NDVI: Application to European, African and South American Areas. *Remote Sensing of Environment*, 57, 167-184.
11. Peres, L. F., and C. C. DaCamara, An emissivity look-up table for LST estimations from MSG data, In *Proceedings from the SAF Training Workshop - Land Surface Analysis*. Lisbon, Portugal, 8-10 July, 2002.
12. Carlson, T. N., and D. A. Ripley. 1997. On the relation between NDVI, fractional vegetation cover, and leaf area index, *Remote Sensing of Environment*, 62, 241–252.
13. Prince, S.D., & Goward, S.N. 1995. Global primary production: a remote sensing approach. *Journal of Biogeography*, 22, 815-835.
14. Pridhodko, L., and S. N. Goward, 1997, Estimation of air temperature from remotely sensed surface observations, *Remote Sensing of Environment*, 60, 335–346.
15. Fensholt, R., Sandholt, I., Stisen, S. and Tucker, Compton. 2006. Analysing NDVI for the African continent using the geostationary Meteosat Second Generation SEVIRI sensor. *Remote Sensing of Environment*, 101, 212-229.
16. MSG Land SAF, *Land Surface Albedo Product User Manual v1.3*. Land SAF, Instituto de Meteorologia, Portugal. 2005.
17. Jacobsen, T.A., Macdonald, A., Enggrob, H. *Okavango Delta Management Plan. Hydrology and water resources. Integrated hydrological model. Draft report*, DHI Water and Environment, 2005.
18. Choudhury, B. J., Dorman, T. J., and Hsu, A. Y., 1995, Modeled and observed relations between the AVHRR split window temperature difference and atmospheric Precipitable water over land surfaces. *Remote Sensing of Environment*, 51, 281-290
19. Jonsson, P. & Eklundh, L. 2004. TIMESAT-a program for analyzing time-series of satellite sensor data. *Computers & Geosciences*, 30 (8), 833-845.

FIRE DETECTION AND PARAMETERIZATION WITH MSG-SEVIRI SENSOR

A. Calle, J.L. Casanova, Moclán, C., Romo, A. and Fraile, S.

Remote Sensing Laboratory of University of Valladolid. Dept. Applied Physic.

Faculty of Sciences. 47071-Valladolid (Spain). Email: abel@latuv.uva.es

Abstract

The detection of forest fires and the determination of their parameters has been a task usually carried out by polar-orbit sensors, AVHRR (A)ATSR, BIRD and MODIS mainly. However, their time resolution prevents them from operating in real time. On the other hand, the new geostationary sensors have very appropriate capacities for the observation of the Earth and for the monitoring of forest fires, as is being proved. GOES, MSG and MTSAT are already operative with time resolutions less than 30 minutes, 15 minutes for MSG, objective of this paper, and they have led the international community to think that the global observation network in real time may become a reality. The implementation of this network is the aim of the Global Observations of Forest Cover and Land Cover Dynamics (GOF/C/GOLD) FIRE Mapping and Monitoring program, focused internationally on taking decisions concerning the research of the Global Change. In this paper, the operation in real time by the MSG-SEVIRI sensor over the Iberian Peninsula is carried out. Its capacity to detect hot forest fires smaller than 0.3 ha in Mediterranean latitudes has been analysed. Concerning fire parameterization two topics are analysed too: the possibility to use SWIR spectral channel in order to replace MIR in saturation situations and dependence of fire parameters versus the problem of resampling pixels.

1. Introduction

The information provided by the polar satellites has been of great help in the establishment of a global system of observation and in the creation of fire occurrence maps. In spite of the fact that the detection results provided by the sensors in polar platforms are not valid for providing early alarms, the fire product created by these sensors has been identified by IGBP as a very important input for the Global Change Analysis (Malingreau, 1990). In any case, the international community has continued working on a system which is able to generate early alarms from spatial platforms. In this sense, the analysis carried out in the European FUEGO programme (Living Planet Programme, ESA) by the European Space Agency has an special interest, with the aim of establishing the observation structure that fulfils the main requirements demanded by the users so that the observation system can later be used to carry

out fire extinction tasks. The main conclusions reached were that the most effective system would be formed by 12 satellites, placed in 3 orbital planes, with inclination angles close to 45° to carry out, with as much frequency as possible, the observation of the geographical latitudes situated between 36° and 45° in both hemispheres. Although the system has never been a reality, it had a very important task by establishing the requirements that a spatial mission should have from the users and administrations involved in the fire extinction. Within the project line previously mentioned, the best prototype the mission could have had is without doubt the experimental satellite Bi-spectral Infrared Detection Satellite (BIRD) developed and operated by the German Institute of Space Sensor Technology and Planetary Exploration (DLR) (Bries *et al.*, 2003). This satellite appeared faced with the necessities demanded by society of having a sensor dedicated to the observation of High Temperature Events (HTE), with a high spatial resolution in the thermal spectrum for the local/regional management of forest fires. BIRD was launched in October 2001 and placed in a low heliosynchronous orbit with two WAOSS-B sensors with the VIS and NIR bands, and the Hot Spot Recognition Sensor (HSRS) with two spectral bands MIR and TIR that provide certain improvements with respect to former sensors based on a good spatial resolution in the 4 µm spectral region, a high saturation level close to 1000K and a dynamic range of radiometric calibration of the MIR band, which makes the quantitative estimation of HTE parameters possible. This experimental mission stopped being operative in 2004 but it has established an unquestionable reference for the sensors aimed at fighting forest fires. Other polar sensors have carried out observations dedicated to the HTE observation, such as the Defence Meteorological Satellite Program (DMSP), Operational Linescan System (OLS) and the Advanced Earth Observing Satellite (ADEOS). However, although the radiometric necessities of detection have been fulfilled, the main obstacle has been the time resolution.

The detection of HTE through geostationary satellites has been taken into account with the different perspective adopted for these platforms. The improvements introduced in the sensors have allowed us to use geostationary satellites beyond their meteorological operativeness adapting them to the observation of the Earth. This has been the response to

the necessity of having series of stable observations of the fire activity for the analysis of the Global Change, the changes in the land use and the monitoring of risks (Justice and Korontzi, 2001). In this sense, the Geostationary Operational Environmental Satellite (GOES) has been the reference worldwide for the monitoring of fires through geostationary platforms. Since 2000, the Geostationary Wildfire Automated Biomass Burning Algorithm (WF_ABBA) has been generating products for the west hemisphere in real time with a resolution of 30 minutes (Prins and Menzel, 1992, 1994). This detection system has been operational within the NOAA NESDIS programme since 2002. The GOES-East and GOES-West spacecrafts are located in the Equator at 75°W and 135°W, providing diurnal coverage of North, Central and South America and data based on the detection of fire and smoke. The results provided by the GOES programme have been the starting point of a global geostationary system of fire monitoring initially formed by 4 geostationary satellites that were already operational, formed by the two GOES platforms, from the USA, the European Meteosat Second Generation (MSG), situated on the longitude 0°, and the Japanese Multifunctional Transport Satellite (MTSAT) situated at 140°E. The MTSAT-1R satellite was put into orbit in February 2005 and it is capable of detecting hot spots and smoke in the geographic latitude interval [80°E, 160°W] having Southeast Asia and several portions of India as observation regions. The main characteristic of this sensor in the detection of fires is its 2 km spatial resolution in the nadir point in the 3.7µm band, which is greatly superior to GOES and MSG. This way, it is able to detect fires of 0.03 ha and 750K placed in the Equator. However, its low saturation level, 320K, and an even worse time resolution of 24 minutes reduce its capacity for establishing the fire parameters in comparison to the former ones.

The minimum fire sizes that these geostationary satellites, GOES, MSG and MTSAT, are able to detect operating with time resolutions less than 30 minutes has led the international community to think that the global observation net in real time may become a reality. The implementation of this network is the aim of the Global Observations of Forest Cover and Land Cover Dynamics (GOFCC/GOLD) FIRE Mapping and Monitoring program, internationally focused on taking decisions concerning the research of the Global Change. The GOFCC/GOLD FIRE program and the Committee on Earth Observation Satellites (CEOS) Land Product validation held a workshop dedicated to the applications of the geostationary satellites for the monitoring of forest fires. This workshop was hosted by the European Organization for the Exploitation of Meteorological Satellites (EUMETSAT), whose most relevant conclusions can be seen in Prins et al. (2004)

The European MSG satellite, also called Meteosat-8, is the first of the second generation of geostationary satellites operated by the ESA since the launching of the first one took place in 1997. MSG was put into orbit in August 2002 and it's a spin-stabilized satellite. The main sensor, and the most important one for the purpose of this paper is the Spinning Enhanced Visible and Infrared Imager (SEVIRI), formed by 11 spectral bands and a visible broadband (HRV) with a spatial resolution of 1 km in the nadir point. The spatial resolution of the rest of the bands is 3 km in the nadir. The scan of the full disk is completed every 15 minutes. SEVIRI has three visible bands (broadband centred at 0.75µm and 0.63 and 0.81 µm), one near-infrared (1.6 µm) and 8 infrared bands (3.9, 6.2, 7.3, 8.7, 9.7, 10.8, 12.0 and 13.4 µm); the spectral resolution of all bands is 10 bits. Without doubt, the main band used in fire detection is the 3.9 µm, with a saturation level of 335K. The improvements introduced in the new Meteosat generation are the ones that have expanded their lines of work to the observation of the Earth (Schmetz et al., 2003).

This paper shows the capacity of the SEVIRI sensor to carry out the monitoring of forest fires working in real time. Some analyses are shown in the particular case of the geographical latitude of the Iberian Peninsula where, during the last three years, detection campaigns and spreading of results in real time have been carried out. The theoretical analysis about the minimum detectable size, including atmospheric effects and saturation conditions, are especially important to delimit the operation range of this sensor in the Mediterranean latitudes, where the effects of the forest fires are more and more important each year both in economic damages and human losses. Especially important are the considerations carried out around the FRE magnitude to continue the methodology of the MODIS sensor. On the other hand, the quantification of this magnitude is essential to establish the means that must be used to put out the fire and to analyse the fire's severity in the view of a future regeneration.

2. Objectives

In order to approach the fire detection and parameterization, three different topics are covered in this paper. First is to develop a methodology to detect the start of fire and to support detection; second topic is to analyze the possibility to use SWIR spectral channel to obtain fire temperature, flaming area and FRE in cases where MIR shows saturated behaviour. Finally, a methodology to resampling pixels is proposed in order to estimate fire parameters according with MODIS results.

3. Fire Detection

The establishment of the minimum fire size detectable by the sensor needs the previous specification of the detection argument; or if that is the case, of the algorithm applied to a geostationary sensor: either establishing a radiometric analysis between the bands of a concrete image or carrying out a comparison between the radiometric signal of the same band in two consecutive scenes if the time difference between them is short. Most of the detection algorithms applied to almost all the sensors use the difference between bands 3.9 μm and 10.8 μm to discriminate HTE. This criterion can be applied perfectly, especially to night scenes, in which the signal received in the region of 3.9 μm comes from the surface emission. This criterion is also valid for sensors in polar satellites whose time resolution does not make it possible to establish comparisons between the successive scenes of the same land cover. However, it is difficult to establish a fixed value for this difference without taking into account the added temperature provided by the solar contribution reflected in the 3.9 μm band, as has been seen above. Being a geostationary sensor with a time resolution of 15 minutes, the comparison between successive scenes provides reliable results once the difference temperature threshold is established for such an interval. Thus, if a time thermal gradient very superior to the one considered as normal is detected, we have a HTE. In order to carry out an estimation, let's consider a day's thermal evolution as a sinusoidal curve responding to the form:

$$\text{MIR_Temp} = A \sin(\omega t - \delta) + B; \quad \omega = \frac{2\pi}{T};$$

where T is the day's period in units of 15 minutes (T=96). A is half of the day's thermal oscillation and B an adjustment parameter of the curve irrelevant for the obtaining of differences. According to this model, the maximum difference in the MIR standard temperature between two consecutive SEVIRI scenes is $\pm 1.5\text{K}$ for a thermal oscillation of around 30K, which is typical of summer days in middle latitudes.

This estimation agrees with the experimental values found in the analysis of the series of MIR temperature evolution curves selected for different places in the Iberian Peninsula during summer days with high values of thermal oscillation, a condition that guarantees the finding of the highest differences between consecutive SEVIRI images adopting a conservative criterion that tends to eliminate false alarms. With respect to the maximum temperature difference found, in absolute values, 98.2% was lower than 2K. Only two values higher than 2.5K (3.2 and 3.7k) were found, probably due to strong anomalies in the atmospheric conditions since they were very hot days with the presence of vertical turbulent effects. The mean value of the differences found, only considering the most enhanced

gradient stretch, intervals [05:00-11:00 GMT] and [14:00-20:00 GMT], was 1.2K, with a standard deviation of 0.5 K. Taking all this into account, we have considered appropriate to establish a threshold of 4K as the temperature increase value to detect the beginning of a fire without providing false alarms.

In any case, it must be pointed out that there are two periods very well defined throughout the day: from dawn to midday, in which the temperature is increasing and where the estimation of 4K is appropriate, and the second one between midday and sunset, for which a value of 2-4K would be enough, being a negative gradient. The thermal changes corresponding to night periods are not so stressed and so they are subject to the former considerations. According to these comments, we have carried out the estimation of the minimum fire size detectable by the SEVIRI sensor when establishing the beginning of a fire. For this purpose, simulations have been done through the MODTRAN code (*Berk et al., 1994*) by introducing different surface and fire temperatures according to different time thermal gradient values. For the obtaining of results, the calculation of the radiance observed by the sensor was carried out according to $L_{\text{sensor}} = p \cdot L_{\text{fire}} + (1 - p) \cdot L_{\text{surface}}$ where p is the surface fraction affected by the fire and where two homogeneous phases have been considered: fire and surface; L_{fire} and L_{surface} are the radiances that coming from the fire and the surface respectively reach the sensor. All the calculations were carried out through the integration of the spectral radiance with a resolution of 20 cm^{-1} , applying the spectral response function of the 3.9 μm band and considering different situations of atmospheric attenuation. The results are shown in figure 1, where the results corresponding to a typical atmosphere of middle summer latitudes and aerosol content with 23 km. of visibility are represented. The axis of abscissa shows the hypothetical fire temperature and the axis of the ordinate, the minimum detectable area expressed in ha.

For the analysis of figure 1, the different magnitudes of influence must be seen separately. The most important of these magnitudes are the threshold of the time thermal gradient considered, $\frac{\partial T}{\partial t}$, and the geographic latitude of observation. The figure contains the results for three different values of the gradient: 4, 6 and 2K/15_minutes and for two enclaves type at 20° and 50° latitude that define the geographic limits of the occurrence of fire considered in this study. With respect to the latitude, it must be taken into account that although the pixels' area in the nadir point is 9 km^2 , at latitude of 20° it is 10 km^2 and at 50° it has increased up to 18 km^2 , mainly because of the variation of the vertical resolution, which is almost 6km. That's why remote sensing is much more limited in high latitudes.

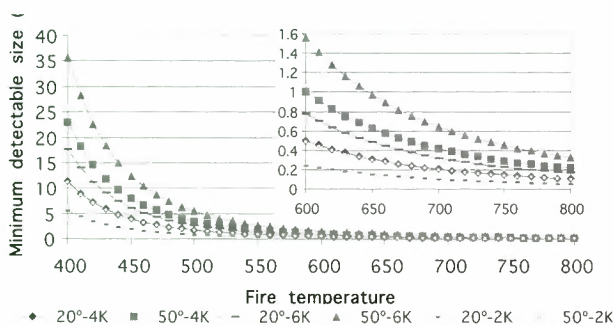


Figure 1. Minimum size of fire (in ha.) to be detected by SEVIRI, for different fire temperature and latitudes, taking into account atmospheric attenuation.

Thus, for a required gradient of 4K/15_min. and a fire of 600K, the detectable area at 20° latitude is 0.5 ha, whereas at 50° latitude it would be 1ha. The geographic longitude has not been analysed since it has a very low distortion in the pixels' area. With respect to the thermal gradient, the value 4K/15_min is the reference for the analysis carried out in previous paragraphs. The figure shows the same results for a value 2K/15_min that can be applied in the descendant period of the day's thermal evolution [14.00-20:00]. During this period

$$\frac{\partial T}{\partial t} < 0$$

is expected and the value 2K/15_min could be enough. This means that during the evening, fires are more easily detected through this methodology and the starting of the fire can be established at 600K with 0.24 ha. at 20° latitude and 0.48 ha. at 50° latitude. As can be seen, the detectable sizes during the day at 20° latitude are similar to the ones in the evening at 50° latitude. These results give a minimum detectable area considerably inferior to the ones presented by Prins & Schmetz, 1999, who did not include the atmospheric attenuation. These results are also slightly lower, although comparable, than the ones presented by Prins et al., (2001), who stated that MSG could detect a fire of approximately 0.2 ha. at 759K in the Equator and a fire of 0.5 ha. at 50° latitude.

A possible problem when dealing with very small fires or fires with not very high temperatures is that the increase of temperature in the MIR band is less noticeable. This could mean that a sharp change between two consecutive scenes wouldn't be detected, although it would in successive scenes once the fire has acquired a larger size. For this case, we have included a comparison with the third scene for a value of 6K that can be applied to skies with very mild cloud coverage. The figure mentioned shows the new detectable fire conditions in this situation, which will be checked more thoroughly when the comparison between consecutive scenes is negative.

The methodology proposed to detect the beginning of the fire is no longer valid as the fire keeps developing since the temperature differences between the different scenes experiment strong variations. Even the frequent appearance of saturated pixels cause sharp changes that cannot be analysed. On the other hand, for the subsequent monitoring of the fire, as will be seen later, it is necessary to have a methodology that provides the detection of hot spots. Fire detection using remote sensing techniques is not a particularly difficult task except for, as it is logical, the possibilities of the sensor used in relation with the minimum size detected and according to the fire's effective temperature. The detection methods used on other sensors that have been the reference are sometimes based on physical models. However, the experimental statistical models have shown better results and are easier to apply. Thus, the algorithms based on thresholds have worked on the AVHRR sensor and the contextual models have been operating on AVHRR and MODIS (Lee et al., 1999; Lee and Tag, 1990; Kaufman and Justice, 1998; Giglio et al., 2003; Justice et al., 2002). However, the difficulty of the validity of the detection results lies in the quality of the data, that is, the appropriate filtering of false alarms since the errors occurred in almost every model are errors of commission. In the case of the SEVIRI sensor, our laboratory has started to get results in real time through the application of a method based on the contextual analysis modified through the time conditions of permanence of the fire. The aim is to spread this information via the Internet with added information concerning the toponymy added value in the events. The methodology followed for the present study is based on the use of two thermal spectral bands situated in the region of 3.9 and 10.8 μm respectively. A contextual analysis is carried out on them through a spatial matrix of NxN pixels, establishing the required statistical parameters, mean value and standard deviation. According our results, obtained from the analysis of a data base of fires validated by MODIS, the best size of window is N=9. The detection test consists, finally, of assigning as affected pixel the one that fulfils the following:

$$T_{39} > \mu_{39} + f \sigma_{39}$$

where μ and σ are the mean value and the standard deviation in each channel respectively. Although the contextual algorithm has been widely used for other sensors, there still aren't any established values for the size of the matrix of analysis applicable to SEVIRI and the statistical factor f. A large interval of values for fires of different sizes have been studied throughout the summer of 2004 y 2005 with the aim of obtaining the detection without the inclusion of a large number of false alarms near the clouds.

Finally, our system is working with three different values, in the interval $f=[2.9, 3.0, 3.1]$ which show three different levels of probability in the detected fire. With respect to the filtering of points of analysis with a cloudy cover, the band of $10.8 \mu\text{m}$ has been used in order to get rid of low temperature points. It must be said that a contextual detection algorithm applied to MSG images, as it has been applied to images from other polar sensors, would be absolutely inadequate to obtain satisfactory results. The detection of the true HTE is easy to obtain but the unceasing appearances of false alarms makes this methodology unfeasible. For this reason, our aim was not to present an effective detection algorithm, but rather to present a method to support the detection of HTE once they have started. The experience has proved that this linked process has good results in the initial detection of HTE and reduces drastically the appearance of false alarms since the contextual process is applied very punctually on the points that are already candidates.

Figure 2 shows results obtained from the last summer campaign over the Iberian Peninsula. Detection results for period August-November, 2005, and time of permanency of fires

4. Fire parameterisation and use of SWIR spectrum

The real usefulness of remote-sensing in the early detection of fires will take place when the time resolution of the sensors implied is around 15 minutes or less. At present, this characteristic is only available in the geostationary satellites, but they have the problem of their low spatial resolution. After the detection, the problem of the analysis of the fire parameters such as the fire temperature, the area affected by it and the intensity radiative, is brought up. The fire detection work has been widely documented for most sensors. In the case of MODIS (Kaufman & Justice, 1998; Ichoku et al., 2003), for the BIRD case (Briess et al., 2003; Wooster et al., 2003) and for the SEVIRI case as an extension of the algorithms for GOES (Prins & Menzel, 1992). The next process to be applied after the detection of HTE is that leading to the fixing of the fire's parameters, that is, the fire's temperature, the area taken up by the burning flame and finally the energy intensity. Two levels of analysis have been distinguished to fix these parameters. First, the analysis at pixel level, where all the pixels affected will be studied and characterised and, on the other hand, the analysis at cluster level. By cluster it is understood a group of pixels affected by the fire and in contact with each other. In the clusters case, the parameters are the cluster's flame area, the cluster's pondered temperature and the total intensity provided by all the pixels affected. In order to carry out this analysis, we have applied a technique based on Dozier methodology (Dozier, 1981; Matson & Dozier, 1981), based on the solving of the

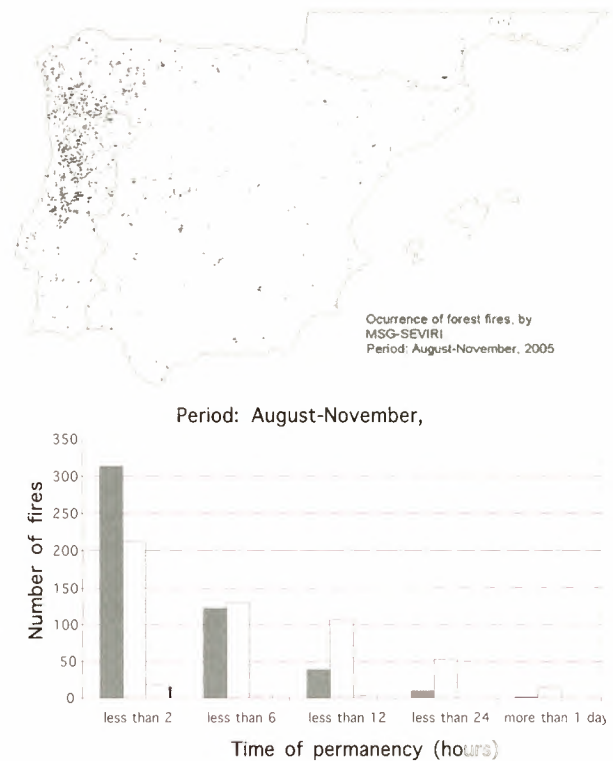


Figure 2: a) Map of fire occurrence in Spain, Portugal and Southern France corresponding to August-November, 2005. b) Number of fires vs. time of permanency detected by SEVIRI.

following system of equations proposed for bands MIR and TIR. The problem in the application of the Dozier equations lies in the introduction of the appropriate surface temperature value. This value is not known and it must be calculated through the mean of the surrounding non-affected pixels. On the other hand, small errors committed when fixing this variable imply strong variations in the establishment of the fire's temperature. Simulations on a real, programmed and controlled fire have been carried out in order to reach some conclusions. For the reasons mentioned above, we have applied the methodology suggested by Giglio & Kendall, 2001. They suggest introducing the surrounding pixels' radiance so that the atmospheric effects and emissivity influence can be taken into account as well as the small surface's solar reflective contribution in day images. This is summarized in the following system of equations:

$$L_{\tau} = \tau_i \rho B(\lambda_i, T_{fire}) + (1 - \rho)L_{background} + \rho L_{atmos} \quad i = 3.9\mu\text{m}, 10.8\mu\text{m}$$

Where τ is the atmospheric transmittance for each channel, λ is the wavelength, T_{fire} is the fire temperature, $L_{background}$ is the radiance coming from surface at level of sensor and L_{atmos} is the radiance coming from atmosphere and it can be neglected. The subsequent fixing of the fire's energy intensity has been carried out through the application of Stefan-

Boltzmann's equation using the fire's area and temperature resulting from the former system of equations.

In order to know the errors and the calculation sensitivity of this methodology, we have chosen the MODTRAN code carrying out simulations of fires of different sizes and temperatures and reproducing next the radiance that would reach the SEVIRI sensor through the filters of the response functions of each band. Then the

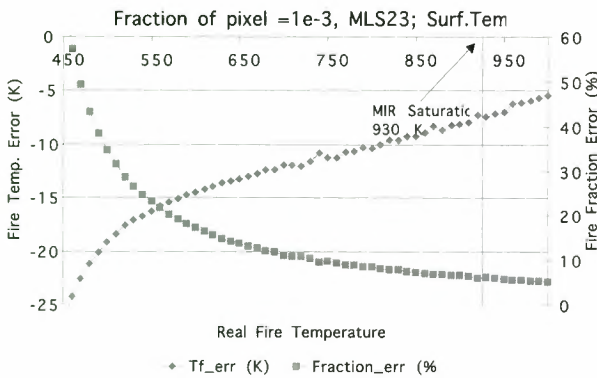


Figure 3. Analysis of errors in the fire parameters. The left scale shows error in the fire temperature and the right scale shows the error in the percentage of fire area.

bi-spectral methodology has been applied on those data in order to establish the fire parameters, that is, the reverse process to the former one. Finally, the comparison between the data coming from the bi-spectral equations system and the hypothetical simulated fires will give us the errors and sensitivity of this process and its performance in the case of this sensor. In order to carry out the simulations above mentioned, a standard atmospheric profile 1976US-Standard and a profile of middle summer latitudes have been used since they are similar to the conditions in which the fires in the Iberian Peninsula will be detected. The aerosols content has varied between visibility values of 50, 23 and 5 km. With respect to the simulated fires, fire temperatures of [350,1100K] with 10K-intervals have been used. The sizes of the fire area have comprised what is considered between small and large fires with fractions of affected pixel in the interval [1e-5, 1e-2], which corresponds to a mean land area at the level of the Iberian Peninsula of [140 m², 14 ha. aprox]. All the calculations have been carried out for the particular case of the 3.9 μ m and 10.8 μ m bands through their spectral response functions. In the calculations that have used integrated magnitudes, such Planck's equation, the central wavelengths and the equivalent width of each band have been used. Figure 3 shows the results corresponding to an active fire that occupies a fraction of pixel of 1e-3, in a range of temperature values in the interval [450,1000K], represented in the axis of abscissa

with a fire-free-surface temperature of 300K. The figure shows the errors obtained when establishing the fire's parameters through the establishment of the fire temperature and the burning area. The first axis of the ordinate represents the difference between the fire temperature obtained in the reverse process applied to the bi-spectral equations system and the theoretical fire temperature used in the simulation of the radiance at the sensor's level through the MODTRAN code.

The operative range of the SEVIRI sensor reaches up to 335K. This value is similar to the AVHRR (Robinson, 1991) and even superior to (A)ATSR with 312K, which has also been used for fire detection (Arino, 2000) although inferior to MODIS (Kaufman & Justice, 1998) and of course, inferior to other sensors with a higher spatial thermal resolution such as BIRD (Lorentz & Skrbek, 2001). This might seem high enough to observe any type of fire and establish their parameters since the SEVIRI pixels area is an order of magnitude superior to the ones mentioned. However, the 3.9 μ m band [3.48-4.36 μ m] appears saturated relatively frequently in several types of fires observed. This situation has advantages since the saturation assures the detection without the possibility of false alarms. However, the radiometric information has been lost and with it the possibility of obtaining fire parameters. The analysis of the factors that cause the sensor's saturation implies, for a geostationary sensor, considering the latitude, given the variability of the area of each pixel. In order to establish the saturation conditions, we have simulated the radiance that the SEVIRI sensor receives for different fire temperatures and different affected areas by limiting these conditions for an apparent temperature value of 335K. Figure 4 shows the fire area, expressed in ha, that would cause the sensor's saturation according to the fire temperature. The figure shows different geographical locations at 20°, 30°, 40° and 50°. The atmospheric conditions with which the results have been obtained correspond to a profile characteristic of the middle summer latitudes and with an aerosol content of 23 km of visibility

In this epigraph, we will analyse the possibility of

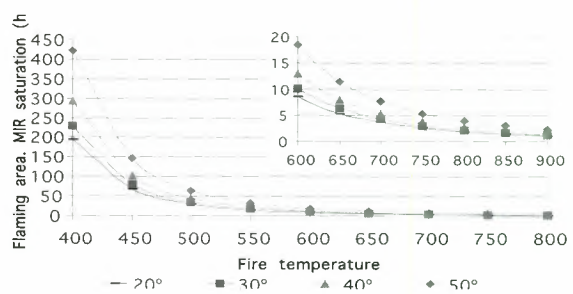


Figure 4. FIRE flaming area, in hectares, that produce saturation on the 3.9 μ m band, versus fire temperature. Graphic shows these results for

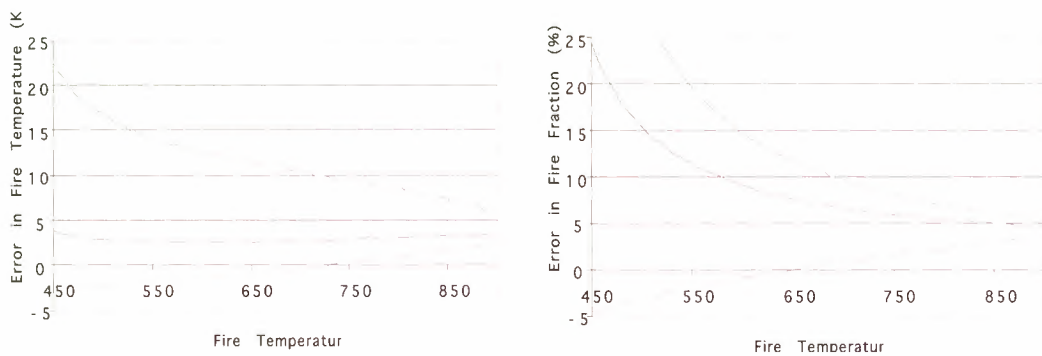


Figure 5. a) Error in fire temperature vs. Fire temperature. b) Error in fire fraction vs. Fire temperature. If color is not available, combinations MIR-TIR, SWIR-TIR and SWIR-MIR are placed from top to bottom. In both cases fire fraction is fixed to $1e-3$ and background temp. 300 K are considered

using band $1.6\mu\text{m}$ for fire parameterization in those cases in which band MIR is saturated. First, we have carried out a theoretical analysis in order to calculate the different errors caused by using different spectral combinations in the resolution of Dozier's system of In order to estimate errors by using different spectral combinations, we have used many different types of fires, with different FIRE temperatures and flaming areas. The MODTRAN code and spectral response functions have been used in these fires in order to evaluate the radiances at the top of atmosphere, that is, at level of sensor. Later, the parameters of the fires entered were calculated again by solving the bi-spectral equation system with different SWIR-MIR, SWIR-TIR and MIR-TIR combinations. Figure 5 represents the parameterization errors using the possible spectral combinations MIR-TIR, SWIR-TIR and SWIR-MIR, part a) FIRE temperature and part b) flaming area. The conclusion reached from this theoretical analysis is that the combinations that include band SWIR present the best behaviour.

The solar component has not been considered in this analysis, which is only valid, consequently, for night images. In case of sun presence, it is necessary to know the emissivity in the SWIR region to break down the components and work exclusively with the emissivity component. The impossibility of knowing the exact value of the emissivity adds errors to this methodology, but it can provide valuable information on the fire parameters when band MIR is not available. Thus, in an attempt to apply this technique to day images, images from MODIS $1.6\mu\text{m}$ band were used in order to calculate the emissivity in each land cover and apply it to SEVIRI images. The methodology consisted in using MODTRAN to establish the radiance at level of sensor by applying the solar conditions of MODIS images. The radiance was calculated separately in different tree covers according to the CORINE Land Cover Map for 2000, applying on these covers the emissivity values

equations. Several authors have proposed the use of short wavelength bands (Giglio & Justice, 2003) although there has not been an estimation of compared errors nor has it been applied on real images.

provided by the Data Base of Spectrum from Johns Hopkins Library under direction of John W. (Jack) Salisbury. U.S Geological Survey in Reston, VA. These radiance values were compared with the ones provided by MODIS images on the same dates as the SEVIRI images analysed. Summarising, the validation results provided errors of 7% in the case of conifers, 15% in the case of dry grass, 1% for the deciduous classes and 3% for sand.

Although this theory should be able to establish the parameters of real fires, its application on SEVIRI images has not succeeded due to different factors. Figure 6 shows a typical case of a fire's evolution which can be considered general and representative. The x-axis represents the hour of the day in which the fire started. The two thin continuous curves show the evolution of

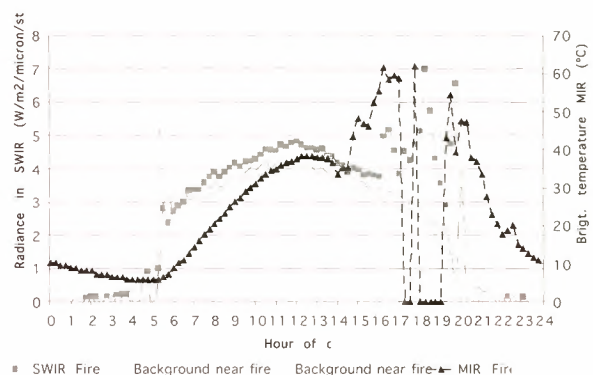


Figure 6: Time evolution (by hour) of a fire. SWIR radiance (in square line) and MIR temperature (in triangle line). SWIR is not sensitive to fire and increasing radiance of fire with $3 \text{ W/m}^2/\mu\text{m}/\text{str}$ only can explained with fire temperature around of 1200 K.

the SWIR radiance in two neighbouring pixels to the one containing the fire and escalated in the first y-axis. Their evolution is as expected with the peaks typically characteristic of the “terminator effect” at dawn and sunset. The line with triangles shows the evolution of the brightness temperature corresponding to the pixel on fire. It can be clearly observed how the beginning of the fire occurs around 14:00 hours; see the peaks corresponding to the pixel saturation. The line with squares represents the evolution of the SWIR radiance in the same pixel that contains the fire. The conclusions are clear: in the first place, the detection of the fire by the SWIR band takes place three hours after the fire started, in the hours close to sunset. Thus, it can be stated that SWIR is not sensitive to the outbreak of the fire. On the other hand, the radiance increase peak in SWIR, close to $3W/m^2/\mu m/str$ can only be explained with fire temperatures higher than 1200K, which is not realistic.

On the other hand, the visual inspection of the images confirms that the fire is only visible from sun zenith angles close to 77° , around sunset. In these cases, the calculation of the temperature does not involve the solar error. However, while parameterization through MIR-TIR provides fire temperatures in the interval [450K–650K], the parameterization by means of SWIR-TIR provides temperatures of [1000K-1800K].

Finally, the band SWIR has arbitrary values that cannot be used quantitatively. Thus, we can state that although the theoretical analyses were very promising for the application of this methodology, the real application is, however, not satisfactory. In future works, two factors should be revised: 1. The calibration of SWIR in the value interval of the fires is correct. 2. Rigorous application of the atmospheric correction, especially of the spherical albedo term, in conditions close to the terminator: dawn and sunset.

5. Correction of resampling method to estimate FIRE temperature.

The SEVIRI sensor has an important limitation when it comes to obtaining the fire temperature in radiometric analyses. In spite of the fact that the resampling step of the sensor is 3 km at nadir, in reality, there is a spatial resolution of 4.8 km with an overlapping of 1.6 km. A consequence of this effect is that the radiance coming from a pixel is at times present in several neighbouring pixels. Although this fact may not imply any problems in other applications, it is of the highest importance in the case of fire detection since fires present confusing geometric structures which make the discrimination of the real affected pixel very difficult. In figure 7, we can observe the typical cross structure and another confusing structure. These two patterns, obtained in real images, appear quite frequently.

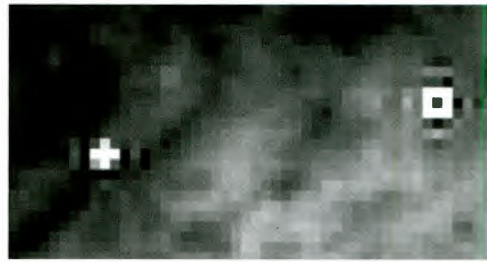


Figure 7: Pattern of sampling of pixels affected by fire

Other important consequence is the inability to compare parameters of fire obtained by other sensors of higher spatial resolution, which is the MODIS case. It must be pointed out that the comparison of results between different spatial resolution sensors is not appropriate from the quantitative point of view although it could be so from the qualitative perspective. This is mainly due to the effect of the sensor’s Point Spread Function (PSF), which carries out a smooth over the radiometric signal and, consequently, over the fire temperature and the FRE calculated for the fire. This comparison effect has already been shown by other authors who have carried out comparisons between results of sensors dedicated to the monitoring of forest fires. As an important example, it must be pointed out the comparison between the sensor of the BIRD and MODIS satellites. BIRD was designed with a spatial resolution of 370 metres in the MIR and TIR bands (staggered sensor with 185 meters of spatial resolution in the resampling process) (Briess et al, 2003). The lower spatial resolution of MODIS appears to prevent many of the less intensity radiating fire pixels being detected as such, meaning MODIS underestimates FRE by up to 46%, in several cases, in comparison to BIRD (Wooster et al., 2003). Our laboratory has found similar results when comparing fires by MODIS and SEVIRI, which is stated in the DEMOBIRD (Definition of the End-to-End Demonstration of the use of Space techniques for forest fires management. ESA project. Contract ESTEC 17192/03/NL/GS).

In order to improve the detection and discrimination of the pixel affected by the fire as well as the calculation of the fire temperature so that it can be compared with other sensors, we have proposed the use of a filter that usually provides “purer” signals of each pixel in the image. Thus, we suggest a filter with the structure of a 3x3 matrix typical of contour enhancement, but adapted to the geometric conditions of the SEVIRI sensor. The filter matrix suggested is as follows:

$$\begin{pmatrix} 0 & -0.5 \cdot A_{\text{over}}(\text{lat}, \text{long}) & 0 \\ -0.5 \cdot A_{\text{over}}(\text{lat}, \text{long}) & + A_{\text{pixel}}(\text{lat}, \text{long}) & -0.5 \cdot A_{\text{over}}(\text{lat}, \text{long}) \\ 0 & -0.5 \cdot A_{\text{over}}(\text{lat}, \text{long}) & 0 \end{pmatrix} \text{ normalized as } \sum_{i,j} a_{i,j} = 1$$

where A_{over} is the overlapping between the central pixel and the neighbouring pixel, which depends on the

geographic latitude and longitude, and Apixel is the total area from which the radiance in the central pixel comes. Let's bear in mind that the area overlapped is practically the same for all the pixels to the right and left but different for the pixels above and below. In the concrete case of a wide zone in the Iberian Peninsula corresponding to lat=42° y long=0°, an example of mean, normalised filter matrix would be:

$$\begin{pmatrix} 0 & -0.309 & 0 \\ -0.14 & +1.898 & -0.14 \\ 0 & -0.309 & 0 \end{pmatrix}$$

However, it must be taken into account that the matrix varies for each longitude-latitude position.

To check the effect caused by the application of this filter, figure 8 shows the radiometric profile of a cross structure corresponding to a detected fire. The most important effect is the correct discrimination of the pixel affected by the fire, whose radiometric value increases considerably with respect to the original profile. The detection of weaker fires can be more effective. Besides, the pixels which are not affected by a sharp change in temperature remain completely unaltered after the application of the filter. That is, this effect only takes place on fires, thus improving their detection.

The most frequent cases are those in which the most intense radiometric signal corresponds to the same pixel before and after the application of the filter. However, we have detected cases in which the radiometric signals of two neighbouring pixels were very similar, but the position of the most intense one changed after the filter was applied. This used to happen in large fires in which several SEVIRI pixels were actually affected. The problem here was not only to improve the detection but also to distinguish which of these pixels contained the most intense fire. In order to validate the technique presented in these “confusing” cases, we have analysed simultaneous MODIS images, which have a resolution of 1km², so as to establish in them the position of the most active fire pixel.

An interesting example is that of figure 9: before applying the filter, two adjacent SEVIRI pixels show the same brightness temperature in the 3.9µm band, but after applying the filter, the hottest pixel appears on the right side. The figure shows the overlapping of these two SEVIRI pixels on the simultaneous image from MODIS 3.9µm channel, in which the position of the pixels affected by the fire can be seen. As can be observed, the fire activity appears on the right side.

Finally, we have used different large fires detected in MSG and MODIS simultaneously in order to carry out the fire parameterization. As was said at the beginning of this epigraph, the fire temperature estimated by

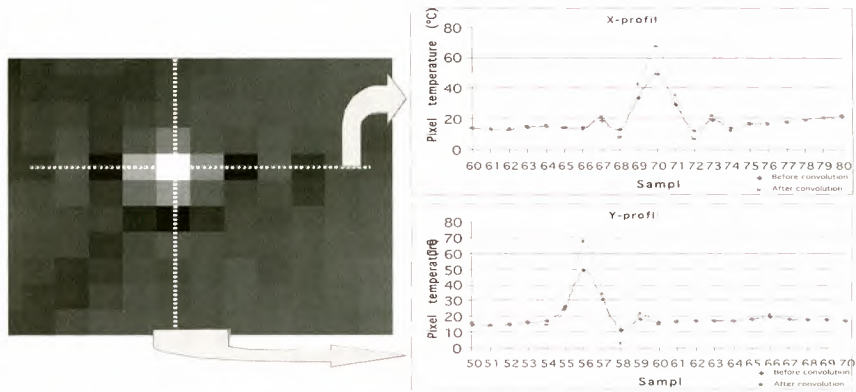


Figure 8: X-profile and Y-profile of FIRE pixel before and after filtering application, in the 3.9 microns channel. The most important effect is the enlargement of main pixel.

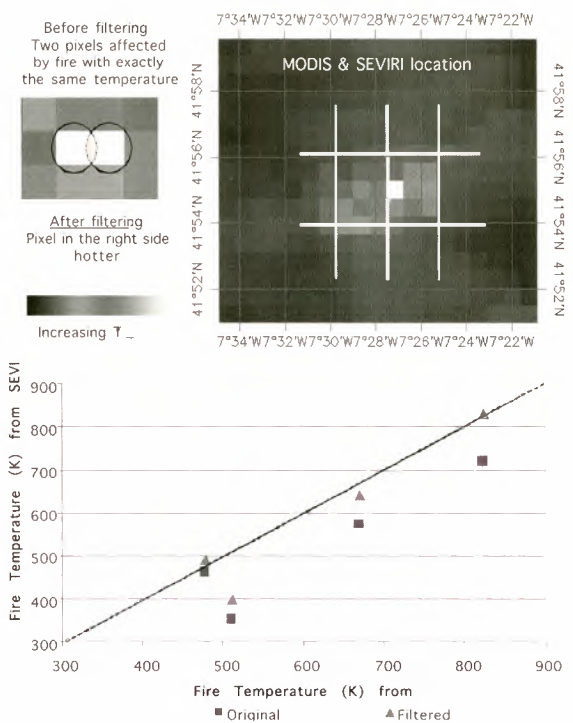


Figure 10: A comparison between FIRE temperature

solving the bi-spectral equation system is lower in the SEVIRI case than in the MODIS case due to different spatial resolutions. Figure 10 shows the comparison results between the fire temperature estimated on SEVIRI and MODIS images. The figure presents the results obtained before and after the application of the filter. In the cases where several pixels were affected, the temperature was obtained on the hottest pixel of MODIS and the hottest pixel of SEVIRI.

The most relevant conclusion is that before applying our methodology, the estimated fire temperatures were lower with differences of up to 100K with respect to the ones obtained with MODIS (square signals in the

figure). The application of the filter provides comparable results in both sensors (triangles in the figure).

6. Conclusions

Three conclusions are obtained for each objective:

Concerning fire detection, the use of temporal thermal gradient, in the 3.9 μm , provides the start of the fire with high accuracy. A contextual algorithm is used for supporting the fire detection.

Concerning use of SWIR, a very sensitive atmospheric correction is required, especially in order to evaluate atmospheric spherical albedo in sun set conditions. No concluding results are founded.

Concerning sampling pixels problem, the filtering matrix proposed improves strongly the detection process. The fire parameterization provided is comparable to MODIS results.

7. Acknowledgments

This paper has been carried out within the 2000 ESA_EUMETSAT MSG Research Announcement of Opportunity ID 2136, titled "Development of an algorithm for the detection and monitoring of forest fires in the Mediterranean area", and the project CICYT ESP2001-4532-PE "Operational Detection of forest fires through MSG images". The authors wish to thank the institutions that have made this paper possible.

8. References

- Arino (2000). Various Authors. ATSR World Fire Atlas validation. ESA-ESRIN, Italy.
- Berk, A., Bernstein, L.W. and Robertson, D.C. (1996), MODTRAN: A moderate resolution model for LOWTRAN 7, Philips Laboratory, Report AFGL-TR-83-0187, Hanscom ARB, MA. 1983.
- Briess, K., Jahn, H., Lorenz, E., Oertel, D., Skrbek, W. and Zhukov, B. (2003), Fire recognition potential of the bi-spectral detection (BIRD) satellite, *Int. J. Remote Sensing*, 24, 865-872.
- Dozier, J. (1981), A method for satellite identification of surface temperature fields of subpixel resolution, *Rem. Sens. of Env.*, 11, 221-229
- Giglio, L and Kendall, J.D., (2001), Application of the Dozier retrieval to wildfire characterization. A sensitivity analysis, *Rem. Sens. of Env.*, 77, 34-49.
- Giglio, L. and Justice, C.O., (2003), Effect of wavelength selection on characterization of fire size and temperature, *Int. J. Remote Sensing*, 24, 3515-3520
- Ichoku, C., Kaufman, Y.J., Giglio, L., Li, Z., Fraser, R.H., Jin, J-Z and Park, W.M. (2003), Comparative analysis of daytime fire detection algorithms using AVHRR data for the 1995 fire season in Canada: perspective for MODIS, *Int. J. Remote Sensing*, 24, 1669-1690.
- Justice, C.O., Giglio, L., Korontzi, S., Owens J., Morisette, J.T., Roy, D., Descloitres, J., Alleaume, S., Peticolin, F. and Kaufman, Y. (2002), The MODIS Fires Products, *Rem. Sens. of Env.*, 83, 244-262.
- Justice, C.O. and Korontzi, S. (2001), A review of satellite fire monitoring and requirements for global environmental change research, In *Global and Regional Wildfire Monitoring: Current status and future plans* (F. J. Ahern, J.G. Goldammer, C.O. Justice, Eds.), SPB Academic Publishing, The Hague, Netherlands, pp. 1-18.
- Kaufman, Y. and Justice, C. (1998), MODIS Fire Products, Algorithm Theoretical Basis Document. MODIS Science Team. EOS ID#2741.
- Lee, T.F. and Tag, P.M. (1990). Improved detection of hotspots using the AVHRR 3.7 microns channel. *Bulletin of the American Meteorological Society*, 71(12):1722-1730
- Li, Z., Kaufman, Y.K., Ichoku, C., Fraser, R., Trishchenko, A., Giglio, L., Jin, J. and Yu, X. (1999). A review of AVHRR-based active fire detection algorithms: Principles, limitations and recommendations. *Forest Fire Monitoring and Mapping: A Component of Global Observation of Forest Cover*, Editors: Ahern, Gregoire and Justice, Ispra, Italy, 3-5 November 1999
- Lorentz, E. and Skrbek, W. (2001), Calibration of a bi-spectral infrared push-broom imager. *Proceedings of SPIE, Infrared Spaceborne Remote Sensing IX*, San Diego, 29 July-3 August 2001.
- Malingreau, J.P. (1990), The contribution of Remote Sensing to the global monitoring of fires in tropical and subtropical ecosystems, *Fire in the tropical Biota, Ecosystem Processes and Global Challenges*. Ed. J.G. Goldammer (Berlin: springer-Verlag), pp. 337-399
- Matson, M. and Dozier, J. (1981), Identification of sub-resolution high temperatures sources using a thermal IR sensor. *Photo Engr. and Remote Sensing*, 47(9), 1311-1318.
- Prins, E.M. and Menzel, W.P. (1992), Geostationary satellite detection of biomass burning in South America, *Int. J. Remote Sensing*, 13, 2783-2799.
- Prins, E.M. and Menzel, W.P. (1994), Trends in South American burning detected with the GOES VAS from 1983-1991. *J. Geophys. Res.*, 99(D8), 16719-16735.
- Prins, E and Schmetz, J. (1999), Diurnal fire active detection using a suite of international geostationary satellites. *GOFC Forest Fire Monitoring and Mapping Workshop*, JRC, Ispra.
- Prins, E., Schmetz, J., Flynn, L., Hillger, D. and Fetz, J. (2001), Overview of current and future diurnal active fire monitoring using a suite of international geostationary satellites. *Global and Regional wildfire monitoring: current status and future plans*, F.J. Ahern, J.G. Goldammer and C.O. Justice Eds., SPB Academic publishing, 145-170.
- Prins, E., Govaerts, Y. and Justice, C.O. (2004), Report on the Joint GOFC/GOLD Fire and CEOS LPV Working Group Workshop on Global Geostationary Fire Monitoring Applications, GOFC/GOLD Report No. 19. 23-25 March 2004. EUMETSAT, Darmstadt, Germany.
- Robinson, J.M., (1991), Fire from space: Global fire evaluation using infrared remote sensing. *Int. J. of Remote Sensing*, 12, pp.3-24
- Schmetz, J., Konig, M., Pili, P., Rota, S., Ratier, A. and Tjemkes, S. (2003), *Meteosat Second Generation (MSG): Status after launch*. Preprints, 12th conference on Satellite Meteorology and Oceanography, Long Beach, C.A., Amer.Meteor. Soc., CD-ROM. P7.3
- Wooster, M.J., Zhukov, B and Oertel, D. (2003), Fire radiative energy for quantitative study of biomass burning: derivation from the BIRD experimental satellite and comparison to MODIS fire products. *Rem. Sens. of Env.*, 86, 83-107.

3rd MSG RAO Workshop – List of Participants

Peter Allan	CCLR	Rutherford Appleton Laboratory	p.m.allan@rl.ac.uk
Wolfgang Benesch	Deutscher Wetterdienst (DWD)		Wolfgang.Benesch@dwd.de
Abel Calle	University of Valladolid		abel@latuv.uva.es
Jose-Luis Casanova	University of Valladolid		jois@latuv.uva.es
Pierre-Yves Deschamps	Laboratoire d'Optique Atmosphérique		pyd@loa.univ-lille1.fr
Bernhard Geiger	Météo-France		Bernhard.Geiger@meteo.fr
Yves Govaerts	EUMETSAT		yves.govaerts@eumetsat.int
Rainer Hollmann	Deutscher Wetterdienst		rainer.hollmann@dwd.de
Anton Kaifel	Zentrum für Sonnenenergie- und Wasserstoff-Forschung		anton.kaifel@zsw-bw.de
Fernand Karcher	Meteo-France		fernand.karcher@meteo.fr
Kristina Katsaros	University of Miami		katsaros@whidbey.com
Ernesto Lopez-Baeza	University of Valencia. Faculty of Physics		Ernesto.Lopez@uv.es
Hermann Mannstein	DLR - Instut für Physik der Atmosphäre		Hermann.Mannstein@dlr.de
Bernard Mayer	Deutsches Zentrum fuer Luft- und Raumfahrt (DLR)		Bernhard.Mayer@dlr.de
Patrick Minnis	NASA Langley Research Center		p.minnis@nasa.gov
Jean-Marc Nicolas	LOA, University of Lille		nicolas@loa.univ-lille1.fr
Evangelina Oriol-Pibernat	ESA		eoriol@esa.int
Rachel Pinker	University of Maryland		pinker@atmos.umd.edu
Mads Olander Rasmussen	University of Copenhagen, Institute of Geography		mor@geogr.ku.dk
Jacqueline Russel	Space and Atmospheric Physics, Imperial College		j.e.russell@imperial.ac.uk
Johannes Schmetz	EUMETSAT		johannes.schmetz@eumetsat.int
Marion Schroedter-Homscheidt	Deutsches Zentrum für Luft-und Raumfahrt (DLR)		marion.schroedter-homscheidt@dlr.de
Geneviève Séze	Laboratoire de Météorologie Dynamique, Université Pierre et Marie Curie		genevieve.seze@lmd.jussieu.fr
Glyn Spencer	University of Leicester		gjs8@leicester.ac.uk
Thomas Nauß	Laboratory for Climatology and Remote Sensing, University of Marburg		nauss@lcrs.de
Jean Verdebout	European Commission - Joint Research Centre		jean.verdebout@jrc.it
Martin Wooster	King's College London		martin.wooster@kcl.ac.uk

European Space Agency
Agence spatiale européenne

ESA Publications Division

ESTEC, PO Box 299, 2200 AG Noordwijk, The Netherlands
Tel: +31 71 565 3400 Fax +31 71 565 5433